Optimization of the fluidization system of the Trailing Suction Hopper Dredger

TU Delft - Section Dredging Engineering

Emal Kamal

2017

Graduation Committee:

Chair professor:	prof. dr. ir. Cees van Rhee
Supervisor TU Delft:	dr. ir. Arno Talmon
Supervisor MTI:	dr. ir. Mario Alvarez Grima

Acknowledgements

In front of you, the thesis of the Master Offshore and Dredging Engineering, at Delft University of Technology. The research is conducted in collaboration with IHC MTI.

I would like to warmly thank professor Cees van Rhee and Arno Talmon for their supervision and guidance. The cooperation with the supervisors is in all times experienced as very pleasant and constructive. I would like to thank Mr. van Rhee for his input and guidance through the research period. And Mr. Talmon, for the support, guidance and the humor during the meetings.

I would like to thank IHC MTI, in particular Mario Alvarez Grima and Rick Lotman for the guidance, understanding and supervision, as well as for the ability of the choice of conducting the research of my interest and the use of the lab and other materials for doing the research.

My thanks and appreciations goes also to Marcel Grotenboer from Deltares. The extending of the hiring period for the use of the sensors and the measuring tools where of crucial importance for the results of the experiments.

My warm appreciations and thankfulness goes to the infinite support and love from my parents and family, who supported me through the ups and downs during the project.

Emal Kamal
Delft, June 2017

Summary

The Trailing Suction Hopper Dredgers (TSHD) are typically used for the transportation of soil. The soil in the hopper can be removed by hydraulic transport using water jets and the discharge at the bottom level of the hopper. The soil fluidization and transportation is jet assisted. The unloading process can take quite some time; the unloading process can be limited by the soil transportation instead of the pumping system. The scope of this research is the optimization of the jetting system in order to deliver high mixture densities, to increase the unloading production and therefore decrease the unloading time.

The information in the open literature describes mainly the jetting parameters, which leads to a certain final fluidized volume, after a long period of jetting ($t > 30$minutes). For the jetting process in the hopper, it is important to understand the influence of the jet parameters over a short period. During the unloading process, the pre-jetting occurs in the order of a few minutes, there is no time for the jets to reach the equilibrium-fluidized trenches. During the pre-jetting period and the unloading period it is not clear how the jets influence the hopper cargo, deep in the hopper. The penetration depth and reach of the jets is not known.

A small testing facility is used for studying of the influence of the jetting parameters on the fluidization process in the bed. Different pressures, flow rates and nozzle diameters are used to study the influence of pressure, flow rate and hydraulic power on the front velocity, fluidized area and the fluidization velocity in the bed and over time.

The design of the fluidization system is based on experience and practical results. For an optimized unloading process, the understanding of the combination of fluidization and unloading is important. Therefore, a hopper section of the '' Vessel'' with the complete geometry and fluidization system of the hopper section, is downscaled with a scaling factor of 7 and the different tests are conducted to study the influence of the jet parameters on the unloading times with the highest productions.

The findings of the literature review and the single jetting experiments are used to test potential optimizations in the small-scale hopper section. Different pressure levels, flow rates, pre-jetting times, ''company philosophies'' and an adapted nozzles configuration is varied to test and verify the findings on a small-scale hopper section.

Based on the results of the literature review, the single fluidization experiments and the small-scale hopper fluidization experiments, recommendations are made for the existing vessel and the TSHD in general.

Table of contents

1 Introduction

IHC MTI is a specialized research wkh and development institute of Royal IHC. IHC MTI has expertise in the fields of dredging, mining and offshore engineering and is mainly doing research and development for the Trailer suction hopper dredgers and dredging equipment. IHC is developing, designing and building vessels and equipment for the offshore and dredging industry.

The main functions of the trailer suction hopper dredger describes three phases, forming the TSHD cycle:

1. Loading and storing soil in the hopper.
2. Transportation of the cargo to dumping location.
3. Unloading the cargo at desired location.

Ad1: Fluidizing the soil on the seabed with the drag head under high flow rates and high jet pressure. Pumping the fluidized mixture into the hopper, giving the mixture settling time for storage in the hopper.

Ad2: De trailer suction hopper dredger sails back to the dumping location.

Ad3: The aim is to unload the hopper cargo as fast as possible, with having no residual load in the hopper. The cargo can be unloaded on two ways: (1) dumping the soil via the bottom doors. (2) Via the self-emptying system, using water jets for fluidization and the emptying channels for transport of the fluidized mixture.

(1) By opening the bottom doors, the soil flows into the dumping location by gravitational forces. Waterjets at the bottom level of the hopper are enhancing the unloading process and preventing bridge forming. In this way delivering a controlled unloading process.
(2) Wat jets in the hopper are fluidizes the soil, the created mixture is pumped via suction channels to the dumping location by rain bowing or hydraulic transport via pipes.

The most decisive physical process during the unloading process are:

- Fluidization
- Breaching

This study is focusing on the optimization of the fluidization system in the hopper. The aim is creating an effective mixture in order to reduce the unloading times. By reducing the unloading

times, the total cycle time of the TSHD shortens; this delivers more TSHD cycles on year bases. Decreasing the unloading times by even a few minutes per cycle reduces transportation costs.

FIGURE 1.1 TSHD UNLOADING VIA RAIN BOWING

1.1 Problem definition

A theoretical description for the design parameters or design specifications of the fluidization system is not available, different parameters simultaneously influence the unloading velocity during the unloading process, these parameters are:

1. Geometry of the hopper
2. Soil specifications
3. Use of suction channel or suction pipe in different configurations
4. The angle of shear strains.
5. Water level conditions prior to unloading and during the unloading process.
6. Capacity of the emptying pump.
7. The number, orientation and position of the nozzles.

The design of the fluidization system is based on experience and practical results. For an optimized unloading process, the understanding of the combination of fluidization and unloading is important.

It is important to know the required jet orientation, position, pressure and flow rate, in order to create an effective mixture for transportation via the emptying channel and pumping system.

Different companies in the Netherlands and Belgium purchase the same vessel from IHC, with the same jetting and unloading pumps. These companies use different water level conditions (dry, saturated, constant water level) in the hopper during the unloading process. Each of these companies are excited about their method**.** The question is: which unloading method is the most efficient? For IHC it is interesting to advise clients which of the methods is more effective for the unloading process.

1.2 Scope

The scope of the study is delivering recommendations for optimizing the fluidization system of the trailer suction hopper dredger, by optimizing the jetting system on the nozzle orientation, position, pressure and flow rate. In order to reduce the unloading period.

1.3 Approach

Delivering a literature study on the jet fluidization process. Delivering a theoretical analysis on the fluidization process in the hopper.

Conducting jetting experiments for in depth understanding of the influence of the jetting parameters in a sand bed.

Combining the findings of the literature review and the jetting experiments for potential optimizations. Testing and verifying the findings on a small-scale hopper section.

A TSHD manufactured by IHC and sold to different companies with the same fluidization and emptying specifications under different names (Pallieter, Reynaert, Artevelde, Marieke), is used as prototype. This vessel is in the report referred as the '' Vessel''.

1.4 Analyzing the jet- and unloading system

The hopper area consists of different hopper sections; in this case, the hopper sections are symmetrical. The hopper consists out of 10 hopper sections. Each hopper section has its own bottom door, unloading door and jetting system. The geometry and jetting configuration is similar for all jetting sections. The ''kippekooi'' is a terminology which is widely used in the Dutch dredging companies; it is a prism shaped obstacle, positioned in the middle of the hopper. The name kippekooi comes from the shape of the structure, which has the shape of a henhouse. The kippekooi functions as an unloading enhancer .The slope angles of the kippekooi are generally larger than the angle of repose, forcing the sand to flow downwards under gravitational forces. The unloading channel and jet water pipes are hided in the kippekooi.

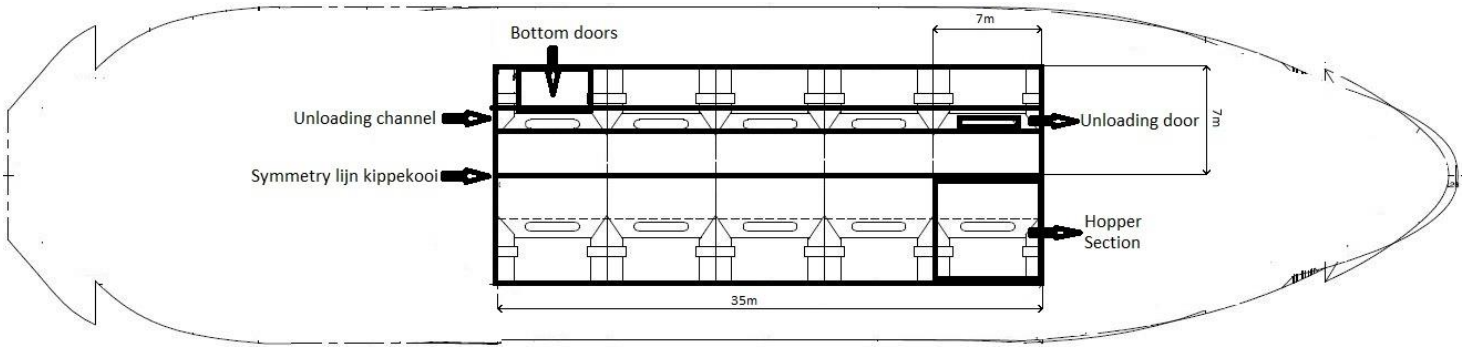

FIGURE 1.2 TOP VIEW OF THE HOPPER

vessel Specifications

- Length 97.50m
- breadth 21.60 m
- molded depth 7.60 m
- draught maximum 7.10 m

Hopper capacity

- $5.600 m^3$

Total installed power

- 6.800 kW

1.4.1 Fluidization system

The jets in the hopper sections fluidizes the hopper cargo under high jet water pressure and flowrate into a transportable mixture, this mixture is unloaded via the bottom doors into the unloading channel, which is then pumped out of the hopper. During the fluidization process, four jetting sections simultaneously fluidize the hopper cargo.

Each jetting section consists out of 7 nozzles, 3 nozzles at the top of the kippekooi and 2 nozzles at each wall side. The nozzles at the top of the kippekooi are parallel to the slope of the kippekooi. The nozzles at the walls of the hopper are positioned 2m above the hopper bottom. These jets are directed towards the bottom doors of the hopper. The jet pressure, diameter and flow rate are similar for all jets.

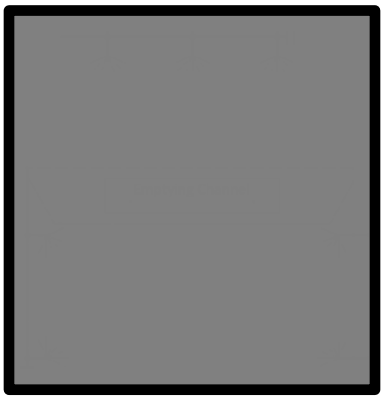

FIGURE 1.4 JET CONFIGURATION IN A HOPPER SECTION

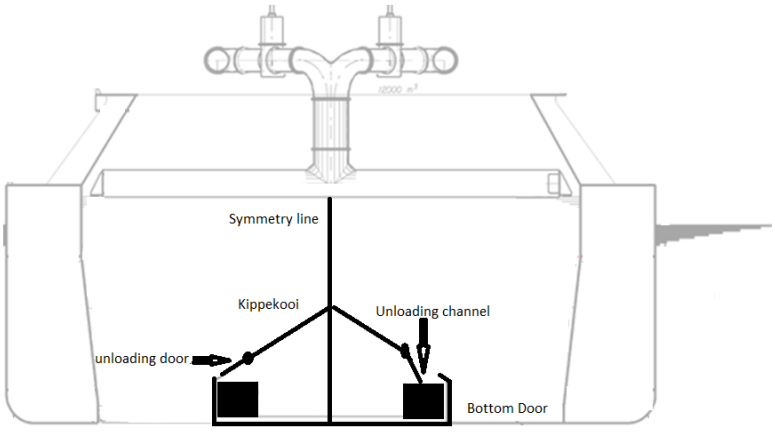

FIGURE 1.3 CROSS VIEW OF THE HOPPER.

The nozzles at the top of the kippekooi functions as unloading enhancers, moving the soil towards the unloading channel. The unloading channel is not a pipeline, but a channel shaped structure spread over the total length of the hopper. The unloading channel is positioned at the bottom of the hopper, with a wall height of approximate 1m above the bottom. The configuration of the structure delivers in almost all hoppers residual load above the bottom doors. The nozzles at the walls are fluidizing deep in the hopper and creating a turbulent mixture moving upwards and in the direction of the unloading channel.

1.4.2 Unloading procedure.

When the TSHD arrives at the dumping location, the unloading procedure starts, the unloading procedure is executed as follows:

The jet pump starts the fluidization process at the rear of the hopper by simultaneously jetting in 4 hopper sections. This phase is known as the pre-jetting phase, the unloading doors remains closed during the pre-jetting periode. The pre-jetting period is somewhere between 3 and 5 minutes. In this phase, the hopper cargo is pre fluidized in order to prevent sanding of the unloading channel. The inserted water during the pre-jetting period, functions also as transportation water. The unloading flow rate is 4 to even 5 times higher than the total jet flowrate.

During the pre-jetting period, seawater is pumped via the sea inlet through the unloading channel. The use of the sea inlet prevents sanding of the unloading channel. If the sea inlet is not used, the mixture suddenly falls into the unloading channel, in a very short period a large amount of sand is dumped in the channel by gravitational forces; this increases the chance of a sanded unloading channel.

After the pre-jetting period, the 2 unloading doors at the rear side of the hopper are gradually opened. The mixture in the hopper flows in the unloading channel, at this point also water from the sea inlet flows through the channel. When the unloading doors are fully open, the water flow in sea inlet is closed; the mixture in the hopper is rapidly unloaded from the hopper sections.

Jetting occurs in all times simultaneously in 4 hopper sections, when the first 2 hopper sections at the rear of the hopper are unloaded the unloading procedure moves to the next 2 hopper sections, which are in this case already pre-jetted. This unloading procedure moves towards the front of the hopper. During this unloading procedure, a large two-dimensional breach is observed, the breach is moving from the rear towards the front of the hopper.

Hopper unloading consists of two unloading rounds. In the first production round (further referred as the ‘’Bulkslag’’), the biggest part, approximate 80 percent of the cargo is unloaded. After the first production round (unloading densities between $1700\,\frac{kg}{m^3}$ and $1900\,\frac{kg}{m^3}$), in all hopper sections remains a small amount of cargo. For the second unloading round (further referred as the ‘opschoonslag’’), the unloading procedure is fully repeated. The bulkslag and opschoonslag both take approximate half of the total unloading time.

2 Literature review

2.1. Fluidization in an infinite domain.

In the chemical industry, there is lots of research conducted on the fluidization of the hopper silos. The hoppers are fluidized by inserting air at the bottom of the hopper, via perforated air systems. The drawback of this research field are the relative small dimensions of the hoppers, however the fundamental fluidization principles remains similar for both disciplines. Insights on the fluidization principles in this report are obtained on the fluidization techniques studied from the chemical industry. Using perforated jetting systems at the bottom of the TSHD is not suitable, since the small openings of the jetting system are sensitive to sanding of the openings.

Studying the jetting process in water, started as early as in the 60-ties (Rajaratnam, Kobus, Clarke, Johnson). Jetting in sand is mainly studied for the fluidization of the upper surface of the sand bed (Rajaratnam, Breusers). In the dredging industry, much research is done for trailing jets, this is important for the understanding of the excavation of drag heads. Very few research is conducted for jetting deep in the soil, in an ''infinite'' large volume. This would be more representative for jetting in the big volume of the hoppers of the TSHD.

2.1 Design of fluidizer systems for Coastal Environment (Weisman and Lennon, 1994)

This study treats the use of a buried pipe (fluidizer) with on both sides' rows of nozzles for the fluidization of sand in a certain coastal domain. The pipe is fluidizing a specified dimension for the applications of sand bypassing and channel maintenance. The scope of the fixed fluidizer is reducing the effort of maintenance work, like periodical deepening of the harbor. The study delivered design characteristics for the desired fluidization area of the fluidizer.

Background

15 years of experimental and analytical research is collaborated and formed into a design methodology for the fluidizer flow rate, the required head in the fluidizer, the fluidizer diameter and the nozzle orientation needed for the understanding of fluidization in 2D and 3D dimensions. Data from field results, like port maintenance and sand bypassing projects are used to analysis of the fluidizer.

Defined Model

This research delivered a model, which estimates the trench dimensions of the removed fluidized sand. The model is defined as:

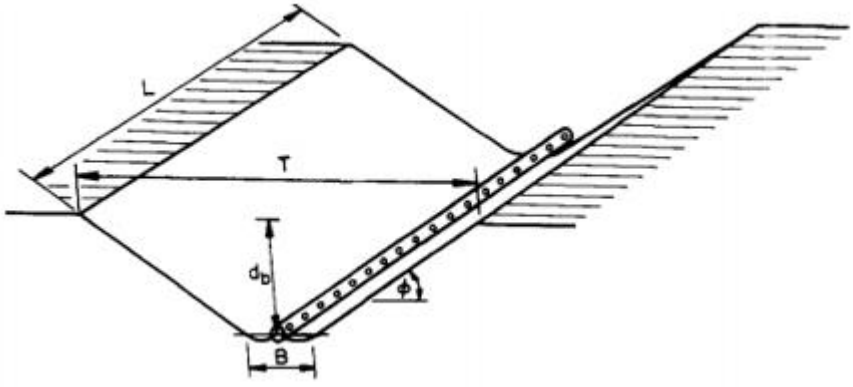

FIGURE 2.1 DEFINITION SKETCH OF THE FLUIDIZER PIPE AND FLUIDIZATION TRENCH

$$T = \frac{2d_b}{\tan\phi} + B \qquad \textbf{2.1}$$

Where:
$T = seabed\ level\ width$
$B = bottom\ width$
$d_b = burial\ depth$
$\phi = angel\ of\ internal\ friction$

Fluidization process

The fluidization process is described in 5 stages:

- **Pre-fluidization (a)**, the sand skeleton is not changing at low flow rates.
- **Prior to Incipient Fluidization (b)**, the law of Darcy can describe the laminar flow through the pores in this stage of fluidization. Increase of the jet flow leads to local fluidization at the nozzles.
- **Full Fluidization (c)**, flow rate increases over time, which delivers an increased fluidized area. Fluidization, first occurs at the upper surface of the sand and then in the horizontal direction of the nozzle. The seepage flow through the pores in the vertical direction increases, therefore the pore spaces in the fluidized area increases, this increases the total volume of the sand bed. The volume expansion leads to fluidization of the soil, the soil behaves as a liquid and a slurry flow triggered by gravitational forces start flowing to the surroundings.
- **Slurry Removal after Full Fluidization (d)**, removing the slurry from the trench leads to instability of the trench walls, this instability inserts more soil in the fluidized area and therefore increases the trench dimensions.
- **Jet Erosion Following Complete Slurry Removal (e)**, in this phase an equilibrium in the trench dimensions is reached.

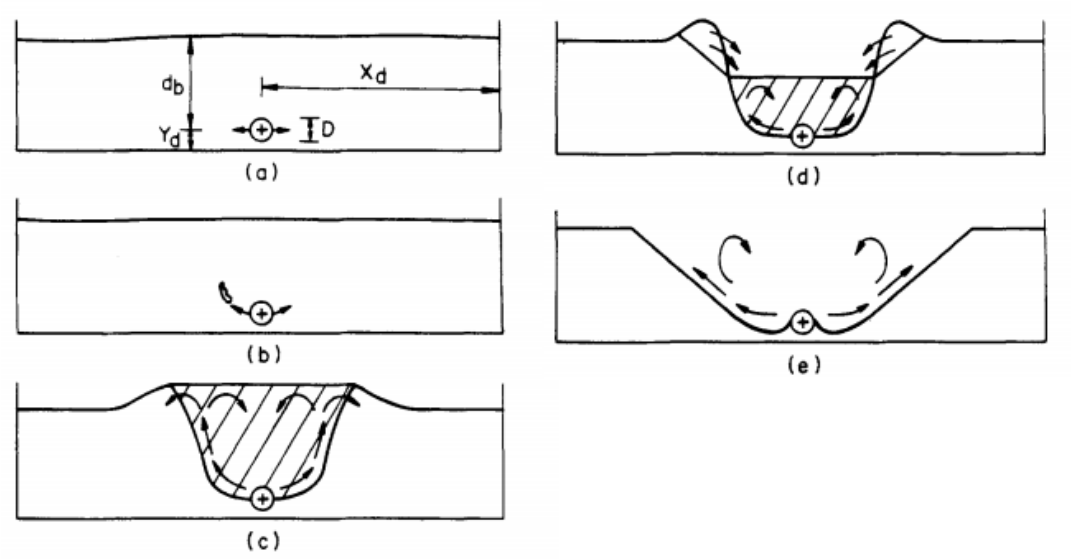

FIGURE 2.2 DESCRIPTION OF THE FLUIDIZATION PROCESS OF THE FLUIDIZER

Experimental specifications

In the smalle scale experiments the soil particle size, nozzle diameter, distance between the nozzles, burrial depth of the fluidizer, flow rate, and the fluidizer head is varied.
Two different particle diameters are used, $D_{50} = 150\ \mu m$ and $D_{50} = 450\ \mu m$. Four different nozzle diameters, D=1.6mm, D=3.17mm, D=4.8mm and D=6.35mm. The nozzle distance is varied to, 2.5mm, 5.1mm, 7.6mm and 10.2mm with a nozzle diameter of D=3.17mm.

Nozzle orientatian

The largest fluidized area is reached by horizontal jets. Nozzles under an upward angle are easily sanded, downward direction of the nozzles excavates the fluidization system deeper in the soil.

Initiation of fluidization

The particle size and the soil depth are the most decisive parameters tor the initiation of fluidization. The flow rate for fluidization is not depending on the soil height, the nozzle distance or the nozzle diameter, the permeability (particle size) of the soil is decisive for the fluidization process. Higher permeability of the soil increases the fluidization velocity.

Required flow rate for fluidization

There is no relation found for the required flow rate, for the initiation of fluidization, nor for maintaining the mixture in suspension. Weisman et al 1988, studied the flow patterns in the sandbed in the surroundings of the fluidizer.The potential flow lines for different phases of the fluidization process are studied. The following conclusions are given:

- The 2D fluidized area, is lineairarily dependent with the flow rate per meter.
- The potential lines in the fluidized zone are lineair, see figure 2.3 e and f.
- Leakage of the jet flow to surroundings is negligible.

- The density of the of the mixture decreases with increasing flow rate.
- No theoretical definition is found for the modelling of the initiation of fluidization.

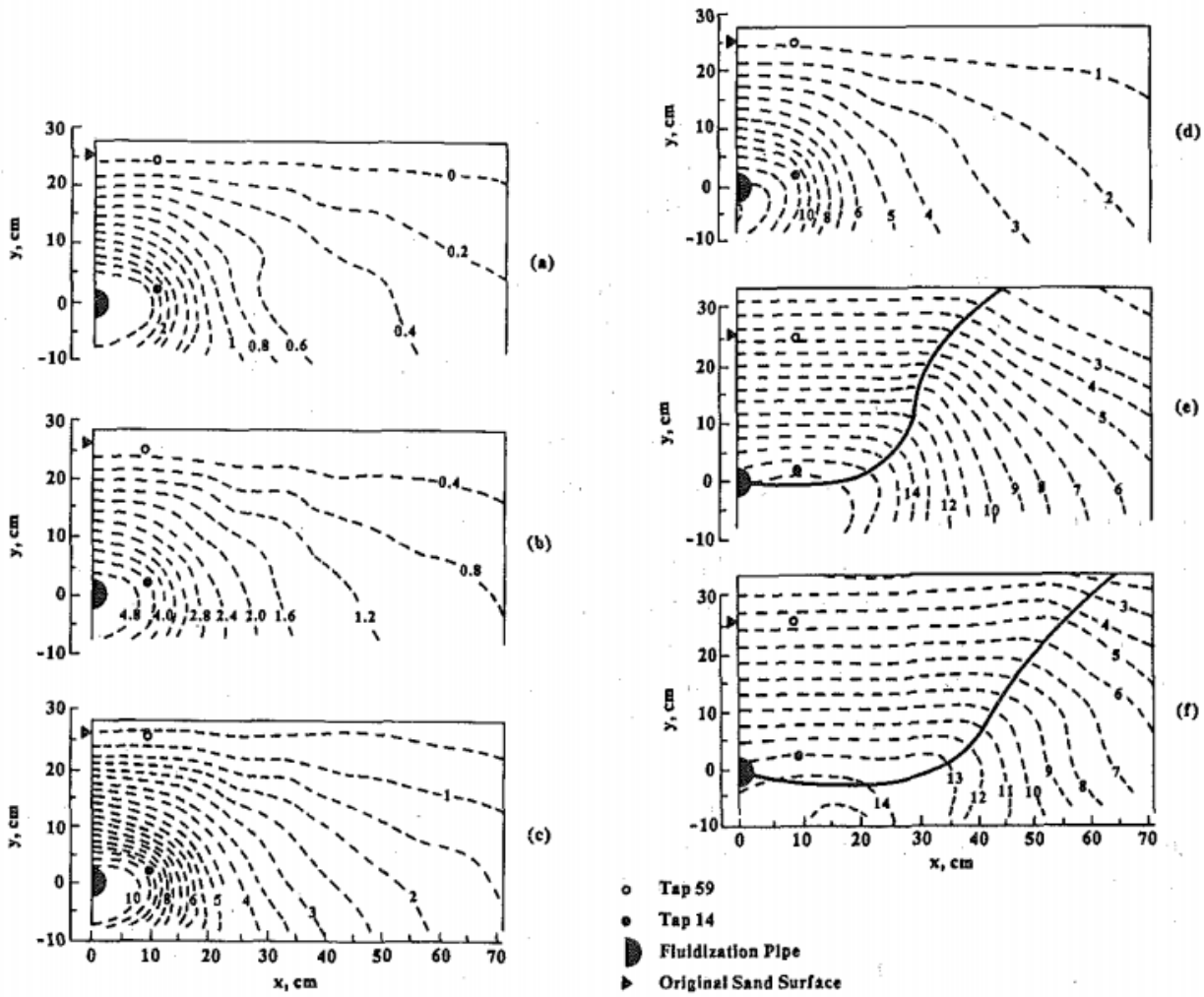

FIGURE 2.3 FLOWRATE FOR A=0.009, B=0.019, C=0.034, D=0.041, E=2.16, F=3.60 [L S^{-1}-M]

Required pressure for fluidization

For a nozzle diameter D=3.17mm and a nozzle distance of 50mm the following findings are mentioned. The head loss of the fluidizer is a balance of the energy dissipation by nozzle contraction losses and energy dissipation by the seepage flow.

Lennon (1995) studied the pressure for the initiaton of fluidization. Lennon, concluded that for small depths a jet pressure of 5 times the bed height is required and for deeper installed jets, a jetpressure of 4 times the burial depth.

2.2 Beunfluidisatie Geopotes 14, (Maas 1992)

The scope of this research is the optimization of the fluidization process of the trailer suction hopper dredger, Geopotes 14. The study consists of a literature review, small-scale experiments and a jet fluidization model. The dimensions of the experimental setup are (LxBxH) 1.9m x 0.6m x 1.2m. In this setup, jet fluidization experiments and fluidizer experiments, has been conducted. The particle diameter in all experiments is $D_{50} = 120\ \mu m$ and two different jet diameters of D=4mm and D=12mm are tested. The pressure is varied from 0.30bar to approximate 2.80bar and the flow is varied from 0.05 L s^{-1} to approximate 1 L s^{-1}. The front wall of the experimental setup is transparent, from which the fluidization process is studied. Maas used different jet specification to study the fluidization trenches and estimated the trench dimensions via observations on the transparent wall. Based on the experimental results a 2D computer model for the fluidization in sand is delivered. This model uses predefined jet characteristics in order to predict the fluidized area of the jet.

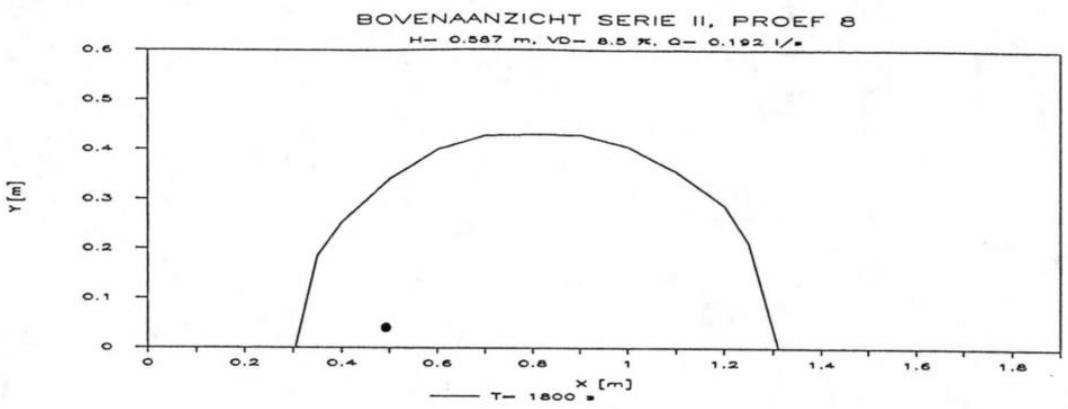

FIGURE 2.4 TOP VIEW OF AN EQUILIBRIUM TRENCH, REACHED AFTER 1800S [MAAS,1992]

Jet flow rate

The fluidized area is mainly a function of the flow, the larger the flow rate the larger the fluidized area. As shown in figure 2.5 Maas concludes that the fluidized area is linear dependent on the flow rate of the jet. The flow rate is the primary factor for the fluidization volume and the pressure is of secondary importance.

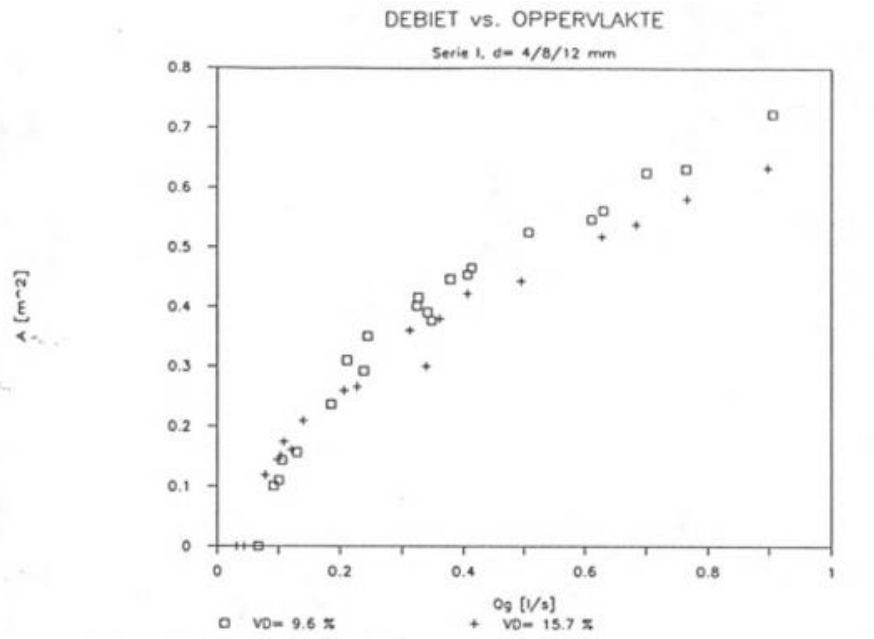

FIGURE 2.5 RELATION BETWEEN FLOWRATE AND FLUIDIZED AREA

Homogenous distribution of the jet water leads to homogenous fluidization of the cargo. The required superficial velocity for the initiation of fluidization is at least five times the permeability of the soil **(Geotechniek, 1985)**. The experiments of Maas confirm the theoretical approach of Geodelft.

Required time for steady state fluidization

Maas studied the time dependency of the jetting process reaching the steady state fluidized trenches. The fluidized trenches were estimated after approximate 30 minutes jetting. According to Maas, the fluidized trenches reaches after approximate 30 minutes in a complete steady state situation.

Jet pressure for fluidization

The pressure level for the initiation of fluidization is higher, compared to the required pressure for maintaining the fluidized soil in suspension. Increasing the jet pressure leads to a nonlinear increase of the jet power. Based on the experiments it seems that it is more convenient to use a lower pressure for delivering the required flow rate for fluidization.

2.3 On self-emptying at high discharge mixture densities, M.A.J. de Nijs (2014)

De Nijs describes an experimental study for the understating of the jet specifications on the unloading times, the experiments consists of a collaboration between the jetting system and unloading system. The experiments studies the variation of different pre-jetting times, jet flow rates, jet pressures and unloading flow rates. The scope of the research is reducing the unloading time by creating higher mixture densities. The experiments shows that local fluidization is sufficient for successful unloading of the hopper.

Experimental Setup

The experiments are executed in hopper with dimensions: (LxBxH) 2.55m, 1.28m, 4.4m. The hopper cargo consists of saturated sand with a grain diameter $D_{50} = 180\ \mu m$. The water level is approximate 4m above bottom; the saturated bed height is 2.5m above . Two conductivity probes positioned at the jetting device and at the suction inlet, estimate the mixture densities. Two pressure sensors, one at the jetting device and the second before the suction inlet are measuring the pore pressure in the system. Four jets with a diameter D=25mm and a nozzle distance of 335mm, are fluidizing the soil.

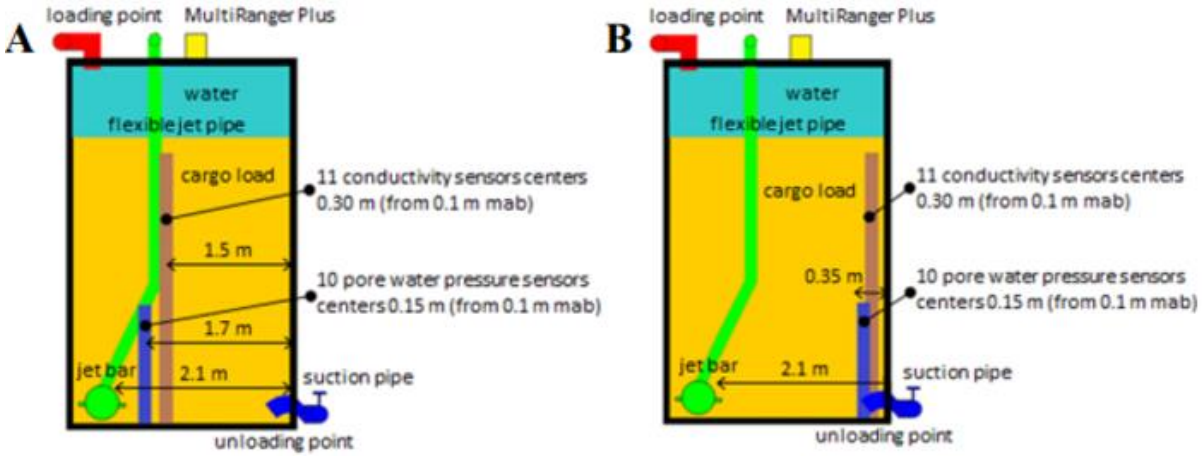

FIGURE 2.6 SCHEMATICALLY GRAPH OF THE EXPERIMENTAL SETUP [DE NIJS, 2014]

See figure 2.6 for the overall layout of the experimental setup.

Pore water pressure

The porewater pressure at the jetting location and the suction inlet increase immediatley after the jet is activated. During pre-jetting period, the density of the cargo remains low, meaning that the pressure information through the soil travels much faster than the seepage flows through the pores. During the pre-jetting periode the pore pressures at the jetbar are higher and a peak pressure is measured.

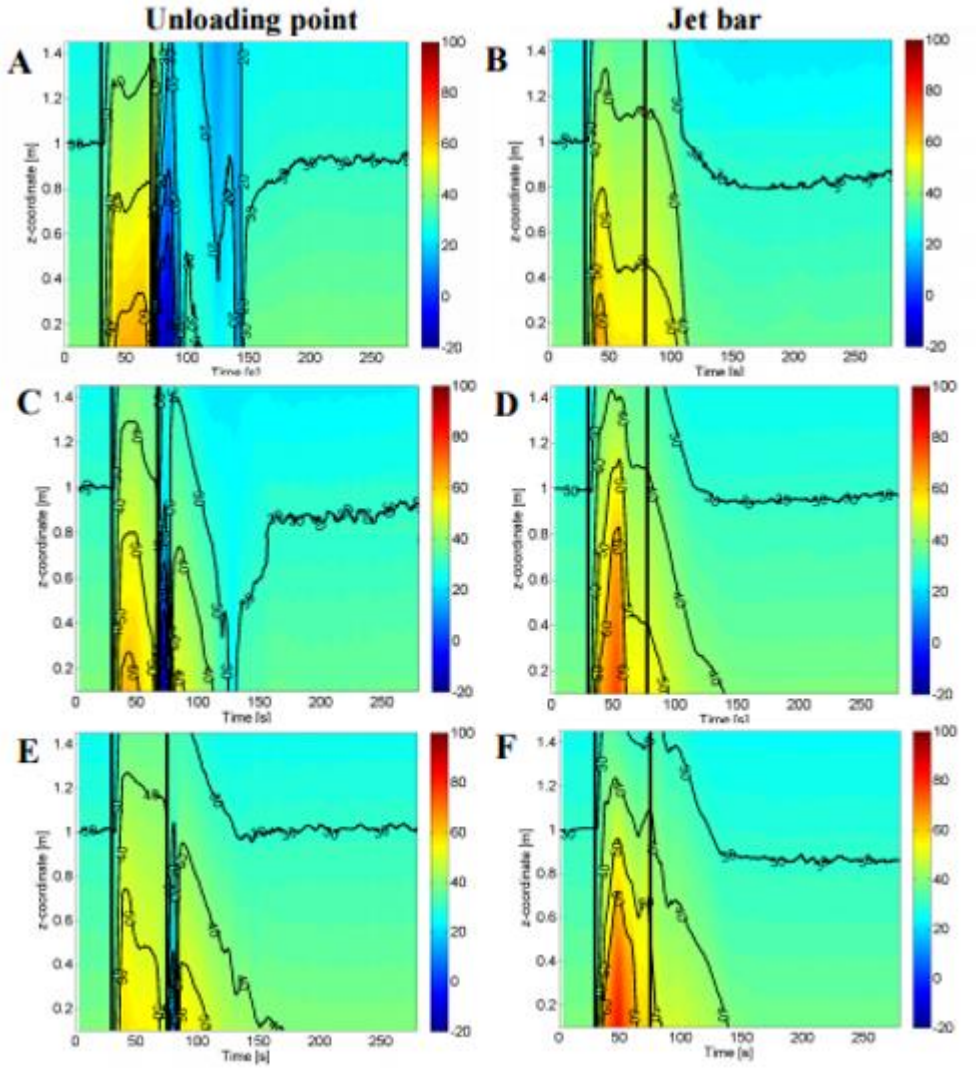

FIGURE 2.7 TIME SERIES OF THE DENSITY OVER THE VERTICAL HEIGHT OF THE BED. A, C, E PORE PRESSURE AT THE UNLOADING POINT. B, D, F PORE PRESSURE DEVELOPMENT AT THE JET BAR.

Pre-jetting effect on the pore water pressure

Increasing the prejetting period does not deliver a lower under pressure in the soil as as shown in figure 2.8, compare figure A at t=75s and figure B at t=100s. The underpressure in the bed is an undesired event which compresses the sand an increaes the possibility of bridgevorming at the suction inlet, sanding in the unloading pipe and cavitation to the pump. At longer pre-jetting periods (longer than 180 seconds) the cargo is fully fluidized (figure D) the homogeniously fluidized soil ommits the effect of under pressures in the sand (figure C).

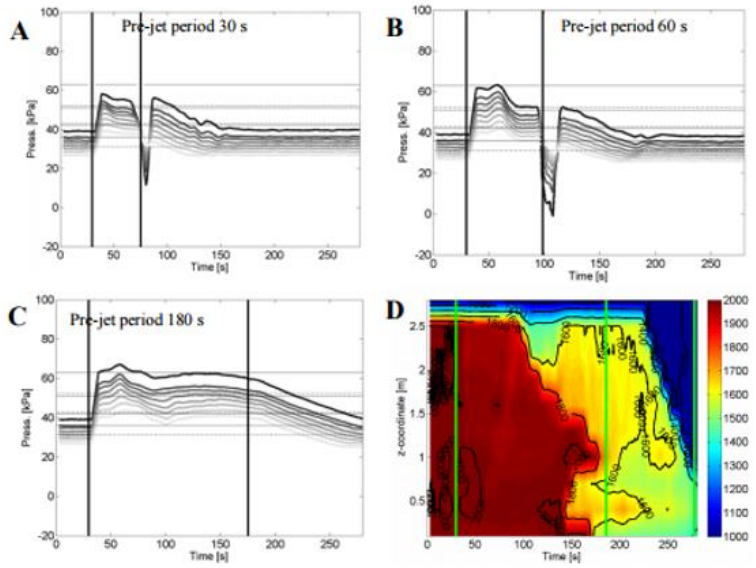

FIGURE 2.8 TIME SERIES FOR THE PORE WATER PRESSURES

Conceptual sketch of the fluidization process

When the jet is activated, a jet cavity develops in the horizontal direction in the bed. The jet predominantly increases in the vertical direction and slowly in the horizontal direction. The development of the fluidized area in the vertical direction leads to piping. After piping occures the fluidized cavity is increasing in the horizontal direction. The first fluidized area forms at the upper surface of the bed. During the unloading process the fluidized area increases towards the suction inlet. By inserting additional water at the top of the hopper, the water level in the hopper remains in all time constant at 4 m.a.b., see figure 2.6.

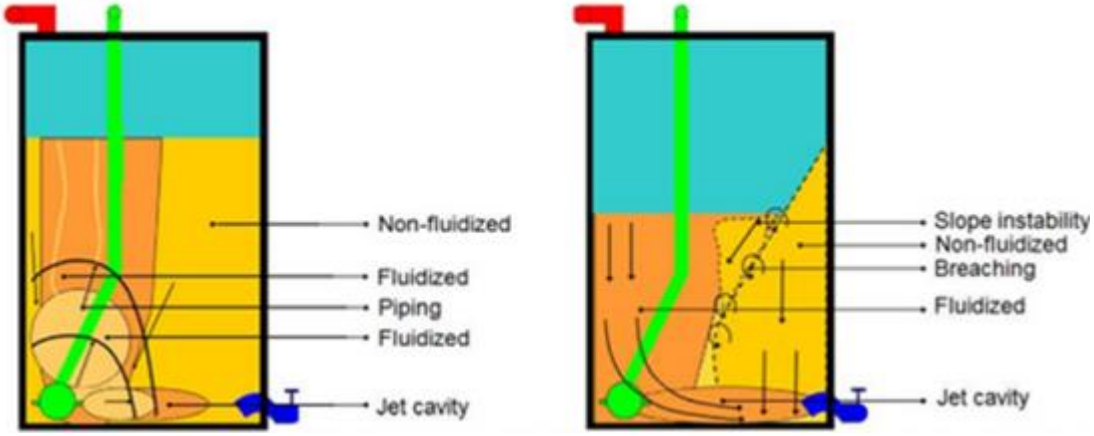

FIGURE 2.9 FLUIDIZATION DEVELOPMENT, LEFT DURING THE PRE-JETTING PERIOD, RIGHT DURING THE UNLOADING PROCESS. [DE NIJS]

TABLE 2-1 EXPERIMENTAL RESULTS DELIVERED BY DE NIJS

	Run1	*Run2*	*Run3*	Run4	Run5	Run6	*Run7*	*Run8*	*Run9*	Run10	Run11	Run12	Run13	*Run14*	*Run15*	*Run16*
T_z [s]	*128*	*115*	***90***	130	139	140	*126*	***95***	***99***	144	143	141	136	*146*	*132*	*137*
$T_{z90\%}$ [s]	*144*	*127*	***99***	145	153	150	*138*	***106***	***108***	166	158	154	148	*161*	*148*	*147*
$T_{z95\%}$ [m^3]	*161*	*141*	***120***	181	171	172	*160*	***126***	***127***	204	181	165	173	*189*	*174*	*171*
Q_p [m^{3}s^{-1}]	*0.151*	*0.152*	*0.153*	0.102	0.101	0.102	*0.151*	*0.151*	*0.151*	0.1	0.102	0.101	0.101	*0.100*	*0.100*	*0.101*
Q_j [m^{3}s^{-1}]	*0.019*	*0.026*	*0.031*	0.018	0.025	0.032	*0.018*	*0.024*	*0.031*	0.012	0.018	0.025	0.032	*0.011*	*0.018*	*0.025*
T_{jet} [s]	*46*	*44*	*45*	60	40	47	*70*	*79*	*68*	71	76	72	67	*103*	*103*	*101*
Q_j/Q_p [-]	0.12	0.17	0.20	0.18	0.25	0.31	0.12	0.16	0.21	0.12	0.18	0.25	0.31	0.11	0.18	0.25

Experimental results

Pre-jetting times of approximate 40s are sufficient. In previous studies of de Nijs (2010b) in which de Nijs refers to internal studies at Van Oord, pre-jetting times of 120s where recommended. The unloading time increases with increasing pre-jetting times, more water in the bed decreases the soil density. Decreasing the unloading flow rate is increasing the unloading time; less amount of soil is removed per second.

2.4 Conclusion literature review jet fluidization

This section gives a summary of the most important findings of the literature review. In general there is less literature for jetting under a few meters thick soil layer in an ‘’infinite space’’ of soil. There is not a general theoretical approach for the estimation of the fluidization of soil in three dimensions. The studies on this topic are mainly experimental studies giving empirical relations for specific conditions of soil type and jet specifications, like jet diameter. The literature review has many common findings, summarized in the following paragraph:

Summary important (common) findings

1. A minimum seepage velocity of five times the permeability is required for the initiation of fluidization (Maas, Weisman et all)

2. Pre-jetting times of approximate 40 seconds are sufficient for prior fluidization. (Nijs)

3. Increasing the pre-jetting times, increases the unloading time. (Nijs)

4. Unloading of higher mixture densities, reduces the unloading times. (Nijs)

5. Lower ratios of jet flow rate and emptying flow rate, delivers higher mixture densities. (Nijs)

6. For the fluidization process, the flow rate is of primary importance and the pressure of secondary importance. (Maas)

7. For an effective fluidization at constant available jet power, it is more efficiently to use low pressure and higher flow rates. (Maas)

8. Homogeneous fluidization of the hopper cargo is not necessary for emptying the hopper load, local fluidization around the unloading point is sufficient. (Nijs)

9. The required jet pressure for fluidization is dependent of the bed height. (Weisman, Maas)

10. After a certain period of jetting in sand a steady state fluidized volume trench is reached. (Weisman, Maas, Nijs)

11. The steady state fluidized area is mainly a function of the flow rate and the permeability of the soil. (Weisman, Maas, Nijs).

12. Horizontal oriented water jets delivers the largest fluidized area. (Weisman)

13. The relation between the flow rate and the fluidized area is linear. (Maas)

14. Smaller nozzle diameters, requires higher jet pressures, in order to maintain a fluidized state. A minimal flow rate is required to keep the particles in suspension (Weisman, Maas)

15. The flow rate for the initiation of fluidization is higher than the required flow rate for maintaining fluidization. (Weisman, Maas).

2.5 Blind spots in the literature study.

The study of Weismann and Lennon describes the fundamentals of the fluidization process; the fundamentals can be used for further study and application in the hopper. This study misses the influence of the jetting specifications in the sand bed. The influence of a certain pressure or flowrate in the bed is not given.

Maas describes piping as a problem for the fluidization process, while piping is a part of the fluidization process. The experiments conducted by Maas, are missing the combination of jetting and unloading of the sand. The experimental results are gained for a long jetting period, in the order of 30minutes. In the prototype, the pre-jetting period is in the order of 3 to 5 minutes. In real scale, the jetting period is much smaller. It is possible that the pressure term is decisive for the smaller jetting periods.

The influence of the jet parameters for the erosion and fluidization velocity in the horizontal and vertical direction of the bed is not treated.

The experiments of de Nijs does not treat the penetration depth of the jets, the influence of pressure is not treated in the paper. The jets in the experimental setup do not represent the unloading process of a hopper as figure 2.9 shows, the hopper geometry and hopper jet configuration are different, think of the influence of the kippekooi and the combination of different jets on the unloading process.

The time dependency of the fluidization process, from the start of the jetting process until the complete fluidization is missing in the studies. All these relevant studies describes the steady state fluidized trench area. Maas describes the equilibrium state of the fluidization; the experiments are conducted for jetting times of approximate 30 minutes. In the hopper, pre-jetting occurs in the order of a few minutes, after this small period the unloading process starts. Therefore, it is important to conduct experiments on a relative small scale in order to gain fundamental understanding of the fluidization process and study the influence of the jet parameters on the fluidization of the soil.

This study continuous on the work of F. Maas (1992) and M.J. de Nijs (2014).

3 Jets

3.1 Jetting in water

This chapter treats the development of submerged water jets, Rajaratnam (1976) conducted much research on this topic. This paragraph describes the free turbulent jet and the derivations for jetting specifications under these conditions. The jet flow conditions, expressions for the flow rate, hydraulic power and the jet discharge coefficients are treated.

3.2 Free turbulent jet

Figure 3.1 gives a description sketch of the free circular turbulent jet. This flow contains two flow regions: the flow development region and the fully developed flow region. The fully developed flow region starts at approximate six times the nozzle diameter 6 D_n .

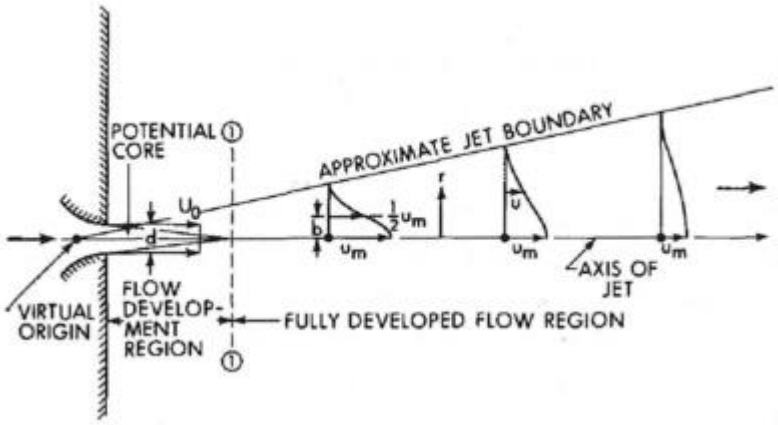

FIGURE 3.1 DEFINITION SKETCH OF A FREE CIRCULAR TURBULENT JET [RAJARATNAM]

3.2.1 Flow development region

The jet water velocity in the flow development region is equal to the velocity at the nozzle outlet.

$$u_{m,s} = u_0 \qquad \textbf{3.1}$$

Where

$u_{m,s}$ = Maximum core velocity $\left[\frac{\mathrm{m}}{\mathrm{s}}\right]$

u_0 = Nozzle velocity $\left[\frac{\mathrm{m}}{\mathrm{s}}\right]$

Once the water leaves the nozzle, the jet water has a much higher velocity than the surrounding (stagnant) water. This velocity difference will result to friction with the surrounding water. Due to the friction, the surrounding water accelerates in the jet flow direction; increasing the total amount of flow. The net flow increase, due to the velocity difference is related to the traveled distance s from the nozzle, this process is known as entrainment.

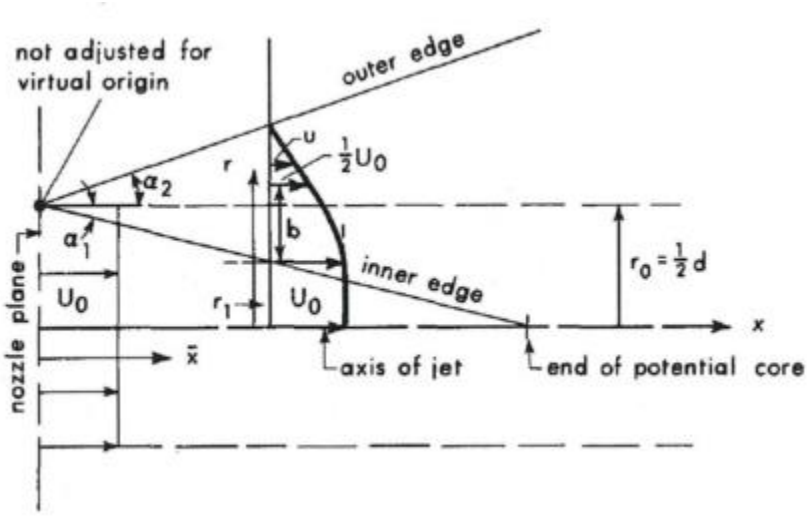

FIGURE 3.2 FLOW DEVELOPMENT REGION [RAJARATNAM]

Albertson et al (1950) described the entrainment in the flow-developed region by:

$$\frac{Q_s}{Q_0} = 1 + 0.083\frac{s}{D_0} + 0.013\left(\frac{s}{D_0}\right)^2 \qquad \textbf{3.2}$$

Where

Q_0 = jet discharge at the nozzle $\left[\frac{m^3}{s}\right]$

Q_s = jet discharge at location s $\left[\frac{m^3}{s}\right]$

s = axis along the flow trajectory [m]

D_0 = nozzle diameter [m]

3.2.2 Developed flow region

From the developed flow region, the core velocity gradually decreases. The flow pattern changes from an arrowed form to a Gaussian shaped flow pattern, this shape increases in front area and reduces the jet penetrating force. The pressure decrease for increasing distance, see expression 3.3.

$$u_{m.s} = \frac{6.3\ u_0\ D_0}{s} \qquad \textbf{3.3}$$

Equation 3.4 describes the velocity for the developed flow region, as a function of the distance s from the nozzle opening and the distance r from the centerline.

$$u(s,r) = u_{m,s}\ e^{-108\left(\frac{r}{s}\right)^2} \qquad \textbf{3.4}$$

The jet discharge in the developed flow region is increasing by entrainment, until the core velocity approaches the surrounding velocity.

$$Q_s = \frac{0.32\ s\ Q_0}{D_0} \qquad \textbf{3.5}$$

3.2.3 Nozzle discharge

By using the Bernoulli equation, the pressure drop over the nozzle, the discharge velocity and the flow rate over the nozzle can be derived. In expression 3.6 the flow conditions in the nozzle (denoted with zero) and the flow conditions far from the nozzles gives:

$$p_0 + \frac{1}{2}\ \rho_w\ u_0^2 = p_1 + \frac{1}{2}\ \rho_w\ u_1^2 \qquad \textbf{3.6}$$

The flow velocity far from the nozzle is negligible, compared to the outflow velocity in the nozzle. Rewriting the Bernoulli equation for equation 3.6 delivers the flow velocity in the nozzle opening:

$$u_0 = \sqrt{\frac{(2\,\Delta\,p)}{\rho_w}} \tag{3.7}$$

The nozzle discharge is a function of the nozzle diameter D_0 and the nozzle velocity u_0:

$$Q_0 = A_{nozzle}\,u_0 = \frac{\pi\,D_0^2}{4}\,\sqrt{\frac{(2\,\Delta\,p)}{\rho_w}} \tag{3.8}$$

3.2.4 Stagnation pressure

The stagnation pressure is the exerted pressure on the sand bed. The stagnation pressure is exponentially dependent on the stand of distance (distance between the nozzle and the bed). The larger the standoff distance the smaller the stagnation pressure. The stagnation pressure follows from the Bernoulli equation, Nobel (2013).

$$p_{stag} = \frac{1}{2}\,\rho_w\,u_s^2 \tag{3.9}$$

For the developed flow region $\frac{s}{D_s} > 6.2$, the ratio between the stagnation pressure and jet pressure gives:

$$\frac{p_{stag}}{P_{jet}} = \frac{\frac{1}{2}\,\rho_w\,u_s^2}{\frac{1}{2}\,\rho_w\,u_0^2} \approx 38.5\left(\frac{D_n}{s}\right)^2 \tag{3.10}$$

3.2.5 Hydraulic Power

The hydraulic power is the jet flowrate multiplied by the jet pressure, the expression for the hydraulic jet power is:

$$P = \Delta p\,Q_0 = \left(\frac{1}{2}\,\rho_w\,u_0^2\right)\left(\frac{\pi}{4}\,D_0^2\,u_0\right) = \rho_w\,\frac{\pi}{8}\,D_0^2\,u_0^3 \tag{3.11}$$

The flow velocity in the equation is in the third order and therefore is the most decisive parameter for the hydraulic power. Increasing the pressure over the nozzle increases the power with quadratic

order. Increasing the nozzle diameter delivers a higher flow rate and in this case increases the power linearly.

3.2.6 Jet momentum

The expression for jet momentum is:

$$I = \frac{2\,P}{u_0} = 2\,\frac{\Delta p\,Q_0}{u_0} = 2\,\frac{\left(\left(\frac{1}{2}\,\rho_w\,u_0^2\right)\left(\frac{\pi}{4}\,D_0^2\,u_0\right)\right)}{u_0} = \rho_w\,\frac{\pi}{4}\,D_0^2\,u_0^2 \qquad \textbf{3.12}$$

The jet momentum increases for the flow velocity and the flow rate.

3.2.7 Jet discharge coefficients

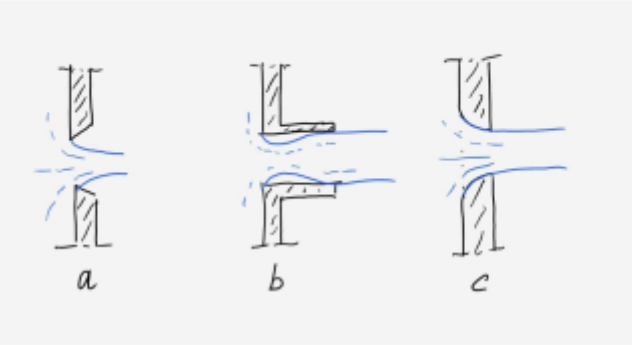

nozzle	a	b	c
c_c [-]	0.62	1.0	1.0
c_v [-]	1.0	0.82	0.98
c_d [-]	0.62	0.82	0.98

FIGURE 3.3 THREE POSSIBLE NOZZLE SHAPES AND THE NOZZLE OUTFLOW CONDITIONS [VAN RHEE, 2016]

The moving towards the nozzle, is contracting towards the opening. Different nozzle discharge openings exist; think off diameter, shape, internal angle. The ratio between the flow contraction and the opening is the contraction coefficient c_c.

For the derivation of the contraction coefficient c_c and the energy dissipation coefficient c_v, see appendix: jet contraction and dissipation derivation.

The nozzle discharge coefficient c_d is a product of c_c and c_v:

$$c_d = c_c \, c_v \qquad \textbf{3.13}$$

In order to minimize the nozzle energy dissipation, the energy dissipation coefficient c_v and the contraction coefficient c_c should be as small as possible. According to figure 3.3, nozzle shape c meets this criterion as best.

Including the discharge coefficient, the jet flow rate becomes:

$$Q_0 = c_d \frac{\pi D_0^2}{4} \sqrt{\frac{\left(2\left(p_1 - p_2\right)\right)}{\rho_w}} \qquad \textbf{3.14}$$

4 Jetting in sand

4.1 Vertical Jetting on a sand bed.

The shape of the jet trench depends on the jet pressure, standoff distance, nozzle diameter and soil specifications. Markvoort,(2002), describes the jetting process in four processes:

1. Penetration
2. Erosion
3. Instability
4. Sedimentation

See appendix sand mechanisms, for in depth background information for the erosion process, the settling velocity, hindered settling velocity and the breaching process.

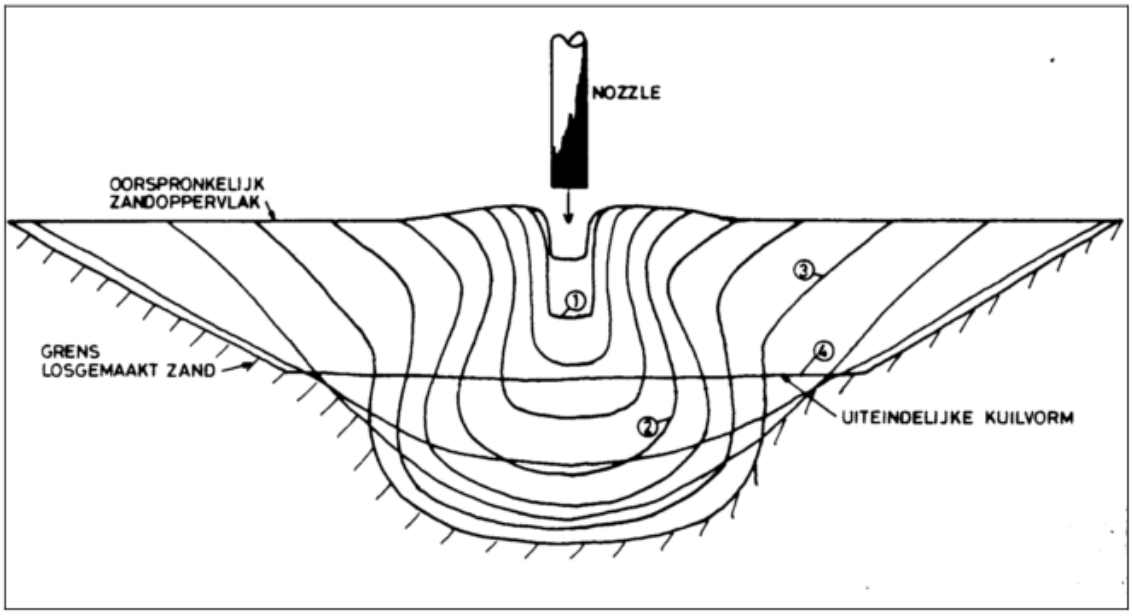

FIGURE 4.1 FLUIDIZATION PROCESS DESCRIBED IN FOUR PHASES [MARKVOORT,2002]

1) Penetration

The penetration depth is the first phase of jetting process, mentioned by 1 in figure 5.1 The penetration depends on the standoff distance (distance between nozzle and jet) and the ratio between the jet stagnation pressure and soil shear strength. For the imagination of process phase one, one can think of firing a bullet into the soil, the bullet penetrates to a certain depth in the soil depending on the bullet velocity and soil specification.

2) Erosion

Once the jet impulse reached its maximum penetration depth, the jet flow deflects and forms concentric circles in the created jetting hole; shown in figure 5.2. The flow deflection in the fluidization pit and the flow pattern of the concentric circles, initiates the erosion of the sand. The mixture flows out the fluidization pit. After a certain period, the erosion process leads to an equilibrium state, giving a fixed jetting hole, with the shape of an upside down mushroom.

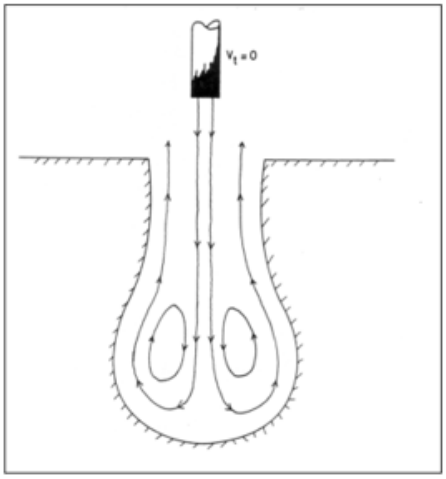

FIGURE 4.2 FLOW PATTERN IN FLUIDIZATION PIT [MASTBERGEN,1995]

3) Breaching

Instability happens on the scale of micro stability (single particle) and macro instability (layers of particles). If the slope angle is larger than the angle of repose and water flows into the pores due to dilatation. Than the breaching process starts and continues, until the slope angle reaches the angle of repose. If dilatation is not occurring and therefore the breaching process is not initiated or stopped earlier than reaching the angle of repose the slope angle will be larger than the angle of repose.

4) Sedimentation

The particles in the mixture tend to settle down under gravitational forces. For the theory behind the sedimentation process, see paragraph 4.2.

4.2 Horizontal jetting in a sand bed.

The same processes described for the vertical jetting are applicable for the horizontal jetting in a sand bed (Markvoort, 2002):

1. Penetration
2. Erosion
3. Breaching
4. Sedimentation

1) Penetration

The water flow penetrates to a certain depth, direct after the penetration the injected water expands the bed and lifts the sand. This creates space for the injected water to accumulate.

2) Erosion

After penetration, the jet flow deflects towards the surface of the soil; this flow erodes the sand and forms a mixture in the accumulated area. The erosion of sand happens at the water flow deflection and the turbulent flow patterns towards the surface. The erosion of sand leads to the concentration increase of soil in the jetting space.

3) Breaching

The accumulation of the injected water creates overpressure in the sand. The overpressure is moving up the sand layer in front of the nozzle and forming an open channel flow towards the surface (piping). Deformations in the soil after the piping process, leads to shear of soil layers, causing under pressure in the soil, the instability triggers the dilatation process leading to the breaching of the sand into the mixture. The breaching process stops when the jet flow is not able to deform the sand bed, from this moment the fluidized trench does not increase anymore.

4) Sedimentation

The particles in the mixture tend to settle down under gravitational forces. The flow rate keeps the particles into suspension. After a certain period an equilibrium between settling particles and eroded particles is reached, delivering a steady state fluidized pit. For the theory behind the sedimentation process, see paragraph 4.2.

4.3 Jet penetration depth

Breusers (1991) conducted vertical jet experiments, using different jet diameters and under different soil conditions. Breusers delivered an expression for the final scour depth of the nozzle; this expression is a function of the jet flow velocity, jet diameter and the shields parameter. The expression is given for two different flow regimes:

$$\frac{y}{d} = 0.08\frac{u_0}{u_{*cr}} \qquad \text{for } \frac{u_0}{u_{*cr}} < 100$$

$$\frac{y}{d} = 0.035\left(\frac{u_0}{u_{*cr}}\right)^{\frac{2}{3}} \qquad \text{for } \frac{u_0}{u_{*cr}} > 100$$

Where

$y = The\ erosion\ depth\ in\ [m]$
$d = jet\ diameter$[m]

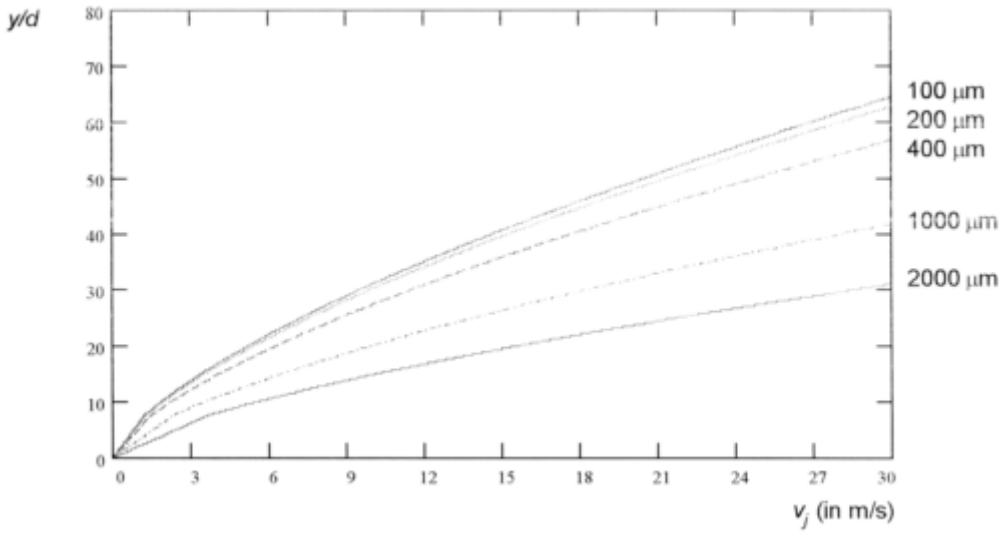

FIGURE 4.3 TRENCH DEPTH AS FUNCTION OF THE JET VELOCITY [BINDT 2002]
The approximation of Breusers for different jet velocities for different and particle diameter.

Using the real scale parameters of $u_0 = 28\frac{m}{s}$, average particle diameter of $D_{50} = 400\mu$ and a nozzle diameter of $43mm$, according to the derivation of Breusers gives an erosion depth of $y = 2.4m$

CSB – trailing jets.

The CSB derived a formula which (Bindt (1996)) describes the erosion depth as a function of the trailing velocity V_v, jet pressure p, jet diameter d, and the particle diameter D_{50}.

$$y = 0.932 \cdot 10^{-3}\, p^{0.59}\, d^{0.492}\, D_{50}^{0.861}\, e^{-0.93 V_v} \qquad \textbf{4.1}$$

For a stationary jet, the trailing velocity is zero and therefore the expression leads to:

$$y = 0.932 \cdot 10^{-3}\, p^{0.59}\, d^{0.492}\, D_{50}^{0.861} \qquad \textbf{4.2}$$

The pressure p is in kPa, the nozzle diameter d in m and particle diameter D_{50} $in\ \mu m$. Filling the scale parameters in the expression gives an erosion depth of 1.3m. There is no physical interpretation given for this formula.

4.4 Fluidization process.

4.4.1 One Dimensional Fluidization

Fluidization is a process where soil in a 'solid' state, is transformed into a 'fluid 'state. The definition of the fluid state in this case means that: solid particles are able to move freely through the fluidized space. In the chemical industry, gas is used for fluidization of the hopper cargo. In the dredging industry, waterjets are fluidizing the hopper cargo. In both industries, the fluid is inserted at the bottom of the hopper.

The fluid moves through the pores of the cargo from the bottom of the hopper towards the surface of the hopper. The pressure difference between the bottom level (higher static pressure) and the surface level (atmospheric pressure), initiates the flow.

For fluidization of the soil, it is important to overcome the gravitational forces working on the bed. At low flow velocity, the fluid has not enough drag force to overcome the gravitational forces of the particles, particles do not move. If the flow velocity becomes high enough, the fluid drag and buoyancy forces will overcome the gravity forces and the bed will expand. If the expansion is, large enough the particles will start moving, forming a fluidized state. Hydraulic transport to the surroundings takes place when the superficial velocity becomes larger than the settling velocity for the particles.

4.4.2 Momentum balance for the initiation of fluidization

This paragraph describes the fundamental fluidization conditions. Water inserted in the hopper bottom flows in the vertical direction towards the surface. The drag force needs to be large enough to overcome the weight of the submerged particles. The momentum balance is used to derive the fundamental condition for the initiation of fluidization.

$$\sum F = m\,a \qquad \textbf{4.3}$$

For the situation depicted in figure 5.4, the force balance becomes:

$$\rho_m\,V\,\frac{dU}{dt} = \rho_m\,g\,V + U_{in}\;\rho_m\;A_{in}\,U_{in} - U_{out}\;\rho_m\;A_{out}\,U_{out} \qquad \textbf{4.4}$$

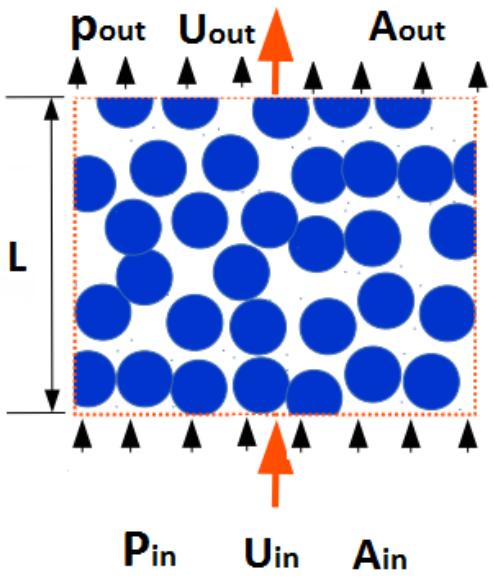

FIGURE 4.4 STATIONARY FLOW CONDITIONS THROUGH A BED

Assuming idealized, stationary hopper conditions, with homogenous density ρ_m and a superficial flow velocity of U where $U_{in} = U_{out}$. The only force working on the particles is the pressure difference between inlet and outlet pressures. Assuming constant area for the inlet and outlet $A_{in} = A_{out}$ of the control volume gives:

$$\Delta P = \rho_m\,g\,L \qquad \textbf{4.5}$$

With

$$\rho_m = \rho_s\,(1-\varepsilon) + \rho_w\,\varepsilon \qquad \textbf{4.6}$$

$\varepsilon =$ the porosity of the bed, substitution of ρ_m gives the fundamental equation for the initiation of fluidization:

$$\frac{\Delta P}{L} = (1-\varepsilon)\,(\rho_s - \rho_w)g \qquad \textbf{4.7}$$

Equation 5.11, shows that the pressure difference over the bed is equal to the submerged weight of the particles.

4.4.3 Pressure drop due to fluidization.

Different authors has approached the hydraulic resistant of the soil by experiments. Darcy's law is valid for the laminar flow regime through the pores. In the fluidization, process of a TSHD the flow through the pores will initially be laminar but very soon end up in the turbulent regime. A well-known and widely used approximation for the hopper fluidization with porous material is the so-called Ergun expression.

4.4.4 Ergun formula

Ergun (1952) and Ergun and Orning (1949) has used small pipes for the modeling of the pore spaces in a bed. The pipe diameters where constant, with paralleled distance between the pipes. The volume of the pipes approximated the pore volume of the packed sand bed.

Ergun and Orning used for their model the general expression:

$$\frac{dp}{dx} = \alpha\, a\, v + \beta\, b\, v^2\, \rho_w \qquad \textbf{4.8}$$

The pressure drop consists out of a viscosity parameter and a kinetic energy parameter.

$v =$ Hydraulic velocity in the pipes$\left[\frac{m}{s}\right]$.

$a, b =$Coefficients

$\alpha, \beta =$experimentally determined correlation coefficients

Ergun experimentally determined the coefficients α and β for different particle size and different liquids. Ergun delivered the coefficients:

$$72\,\alpha = 150 \quad and \quad \frac{3}{4}\,\beta = 1.75 \tag{4.9}$$

For detailed information and derivation of the Ergun formula, see appendix: Ergun and Orning formula

The well-known Ergun equation reads:

$$\frac{dp}{dL} = \frac{72\,\alpha\,(1-\varepsilon)^2\,\mu_w\,U}{\varepsilon^3\,(\varphi\,d)^2} + \frac{3\beta\,(1-\varepsilon)\rho_w\,U^2}{4\,\varepsilon^3\,\varphi\,d} \tag{4.10}$$

The shape factor φ is included for irregular according to J. H. Perry (1984) $\varphi = 0.83$ for rounded sand.

4.4.5 Minimum fluidization velocity

It is important to know the required pressure and flow for the fluidization system. The minimum superficial velocity is decisive for the design of the required jet flow rate. The jet pressure is the required pressure for maintaining the soil particles in fluidized state, in other words the pressure needed to overcome the weight of the submerged particles, this is the opposite flow velocity for the hindered settling velocity of a mixture.

The porosity of the soil determines the superficial velocity. In the Ergun equation, the porosity is the single most decisive parameter, the porosity in the denominator is in the third order.

The values for the porosity in literature are in the order of $\varepsilon = 0.40$, (When and Yu) $\varepsilon = 0.42$, (Barnea and Mednick) $\varepsilon = 0.415$. The porosity of the soil in the experiments is determined according the prescriptions of MTI. **.** The porosity value for un-compacted soil is $\varepsilon = 0.43$ and for compacted soil $\varepsilon = 0.395$. In this report, the porosity value for the compacted sand is used. The loaded hopper sails to the dumping location, due to the vibration of the engines and the motion of the waves it is more likely that the san bed becomes compacted.

Minimum flow velocity

The minimal fluidization velocity follows from the balance between the between the Ergun equation and the equation for the bouncy force. This balance delivers the minimum superficial velocity to overcome the gravity force exerted by the particles.

$$150\frac{(1-\varepsilon)^2\,\mu_w\,U}{\varepsilon^3\,(\varphi\,d)^2}+1.75\frac{(1-\varepsilon)\rho_w\,U^2}{\varepsilon^3\,\varphi\,d}=(1-\varepsilon)\,(\rho_s-\rho_w)\,g \qquad \textbf{4.11}$$

Using the following parameters:

$\varepsilon = 0.40$
$\mu_w = 1\cdot 10^6\ kg/ms$
$d = 1.3\ \mu m$
$\varphi = 0.83$
$\rho_w = 1000\ kg/m^3$
$\rho_s = 2650\ kg/m^3$
$g = 9.81\ m/s^2$

Gives $U = 0.008\,m/s$.

In real scale $u = \frac{Q}{A}$. One hopper section consists of seven nozzles with a flow rate of $Q_n = 0.042\frac{m^3}{s}$; this gives a total flow rate of $Q_{tot} = 7\cdot 0.042 = 0.294\frac{m^3}{s}$. The hopper section area $A_{hs} = 7m\cdot 7m = 49m^2$. The porosity is assumed $\varepsilon = 0.40$, this gives an effective flow area of $49m^2 * 0.4 = 19.6m^2$. This delivers a superficial velocity of $u = \frac{Q}{A} = 0.015\frac{m}{s}$. According to Basu en Ghosal, the porosity in the fluidized state becomes $\varepsilon = 0.55$ delivers a mixture density of $\rho_m = 1740\frac{kg}{m3}$. The theoretical velocity, according to Ergun is $8\,\frac{mm}{s}$, this would lead to a porosity of $\varepsilon = 0.48$ and give a theoretical density of approximate $\rho_m = 1860\frac{kg}{m^3}$. The Ergun approximation is a relative good approximation since: $\frac{1860-1740}{1740}\cdot 100\% = 7\%$ deviation from the expected value.

In the experiments a flow rate of $Q = 0.0024\frac{m^3}{s}$ is used. The area is 1*1=1m2, due to the pore space, this would give and effective area of 0.4m2. Resulting to a superficial velocity of u=Q/A= 0.006 m/s. According to Basu and Ghosla give a porosity of 0.45 and in case of homogenous fluidization this delivers a mixture density of approximate $\rho_m = 1900\ kg/m3$.

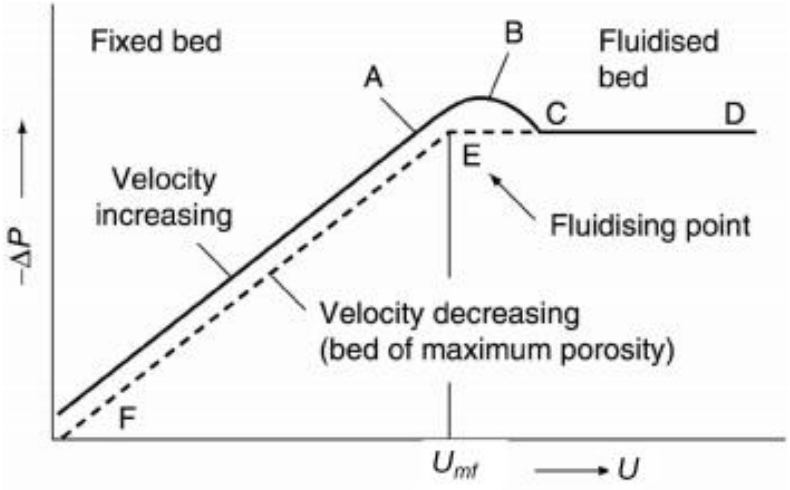

FIGURE 4.5 PRESSURE DROP AS FUNCTION OF THE SUPERFICIAL VELOCITY

http://www.che.ufl.edu/unit-ops-lab/experiments/FB/FB-manual.pdf , Updated February 8, 2017

The pressure drop increases with flow rate, point A in figure 5.6, gives the seepage velocity for which the bed starts expanding. Point B is the flow rate for the maximum pressure drop; at this point, the pressure drop is large enough to activate the fluidization process. Point B is the required minimum superficial velocity for non-spherical particles; non-spherical particles require larger force for the initiation of fluidization, non-spherical particles collaborate against the overpressure. After this ''activating point'' B the bed is fluidized. Point E is the minimum fluidization velocity for spherical particles. Once the bed is fluidized, the pressure drop remains constant, see points C and D. Reducing the flow rate moves the path of superficial velocity backwards from point D to E and from E to F.

5 Single fluidization experiments

5.1 Introduction

This chapter treats the experimental setup; the execution- and the results of the experiments. The experiments are conducted in the MTI laboratory in Kinderdijk, The Netherlands.

FIGURE 5.1 TESTING FACILITY FOR THE FIRST SERIES EXPERIMENTS IN THE MTI LAB, KINDERDIJK.

5.1.1 Motivation for the experiments.

The scope of the first experiments is to gain understanding of the influence of the jetting parameters on the fluidization in sand. The following is important for the fluidization:

A. The influence of jet pressure, jet flow rate and jet hydraulic power on the fluidization process in a constant volume of soil.
B. The time scale on which different fluidization phenomena occurs.

The following jet variations are important for the understanding of the influence of the jetting parameters on the fluidization process:

- Different flow rates at constant pressure.
- Different pressures at constant flow rate.
- Different pressure levels at constant hydraulic power.
- Different flow rates at constant hydraulic power.

Symmetry plane

Placing the jet close to the transparent wall gives the ability to track and study the jetting process. The geometry, development of the fluidization process and equilibrium trench is visible; recordings are made for further study of the jetting process. The disadvantage of the symmetry wall is the so-called wall effects; the jet water close to the wall reflects and influence the trench shapes, the wall reflections, leads to (slightly) larger fluidization trenches.

Scale of the experiments

For the first series experiments, no scaling rules are applied.

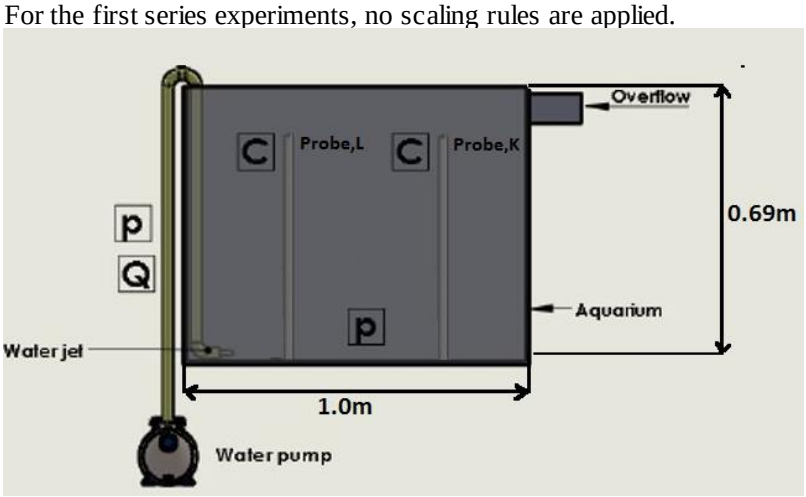

FIGURE 5.2 SCHEMATICALLY OVERVIEW OF THE AQUARIUM AND THE LOCATIONS OF THE SENSORS IN THE AQUARIUM. P IS THE LOCATION OF PRESSURE SENSORS. C CONCENTRATION MEASUREMENT AND Q IS THE LOCATION OF THE FLOW SENSOR

5.1.2 Experimental Setup

For the execution of the experiments, the following list of materials is required:

A. Aquarium
B. Sand
C. Water reservoir
D. Overflow storage
E. Jetting system
F. Big Bag
G. Pressure sensors
H. Flow rate sensor
I. Centrifugal pump
J. Conductivity probes

Ad A) Aquarium

The Aquarium is a metal container with dimensions: $(L \cdot B \cdot H) = (1.0 \cdot 0.33 \cdot 0.690)m$, see figure 5.2. The aquarium consists of a transparent wall; this gives the possibility to track the jetting and the fluidization process. The position of the overflow is at the top left corner of the aquarium. The mixture in the aquarium flows via the overflow to the settling compartment in the water storage container.

Ad B) Sand

The Sibelco AF100 sand is used for the tests, the sand consists of a narrow graded particle size, with median particle diameter $D_{50} = 130\mu m$, see the PSD and more detailed information about the AF100 sand in appendix V and VI.

The sand contains small fractions of ions; the ions in the sand has to be rinsed from the sand, washing of the sand is conducted as follows:

By removing the inner plastic of the big bags (BIGBAG Store) the big bags becomes permeable for water. It takes approximate 15 minute of continuously adding water into the bags in order to reduce the conductivity of the sand to the level of domestic water. During the washing process, water is periodically extracted from the big bag in order to measure the conductivity of the sand. This process is repeated each time when new sand is added into the aquarium.

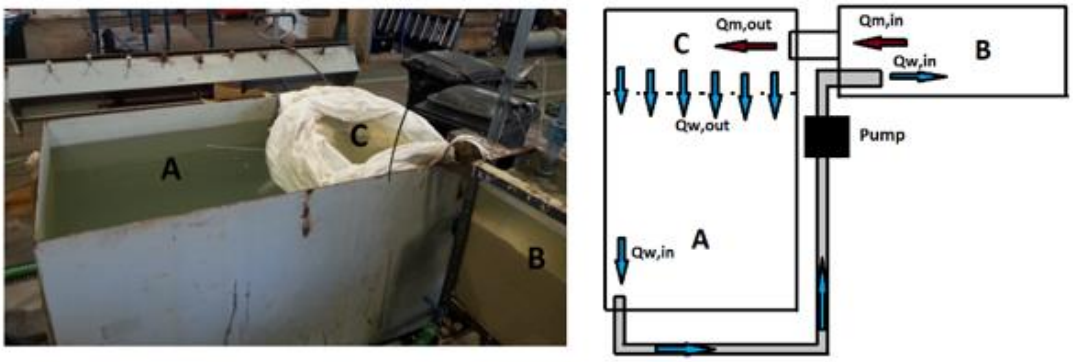

FIGURE 5.3 LEFT, THE WATER RESERVOIR AND THE STORAGE TANK. RIGHT DESCRIPTION SKETCH OF THE CLOSED WATER LOOP

Ad C) Ad D) Water reservoir and Overflow storage

The water reservoir and the aquarium form a closed system, see figure 5.3. The centrifugal pump transports water from the water reservoir (A), towards the aquarium (B). In the aquarium, the water flows through the nozzle and forms a mixture in the sand bed. When the mixture reaches the overflow level, the mixture flows from the aquarium B into the settling compartment (C). The sand is settling in the big bag in compartment C, the wall height between compartment A and C is lower, compared to the wall heights of the water reservoir. The exceeding water flows over to the water reservoir (A) and thereby forms a closed water loop.

Ad E) Jetting system

The jetting system transports the water from the storage tank into the aquarium; the jetting system consists of the following components:

- Flexible pipe
- PVC pipe
- Nozzle housing
- (Different) nozzle diameter(s)
- Centrifugal pump.

The flexible pipe ($D = 50mm$) connects the water reservoir and the centrifugal pump. The PVC pipe connects the centrifugal pump with the nozzle. The nozzle consists of a nozzle housing diameter of D=55mm and replaceable nozzle diameters. The nozzle housing is fixed on the PVC pipe. The nozzle diameters are replaceable via fabricated threads, see figure 5.4.

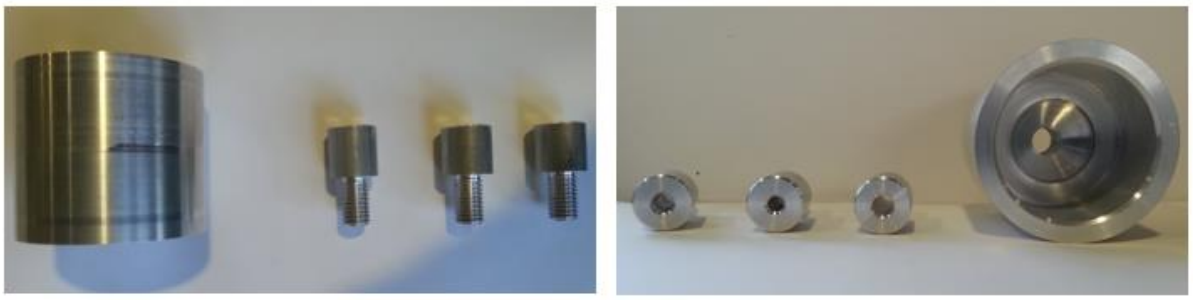

FIGURE 5.4 THE NOZZLE HOUSING AND THE REPLACEABLE NOZZLE DIAMETERS

Ad F) Big Bag

The Big Bags in compartment C functions as filter bags, and store the settled sand from the overflow. The Big Bag prevents the overflow of sand to compartment A. The big bag collects the settled sand, this makes re-use of the sand easily and prevents mixture flow into the suction inlet of the pump.

Ad G) Pressure sensors

There are two pressure sensors in the system, one pressure sensor measures the actual jet pressure in the pipeline**,** this pressure sensor is at the same level as the flow sensor. The second (diaphragm) pressure sensor gives the actual (pore) pressure in the sand bed. This sensor gives an estimate of the pressure buildup in front of the nozzle and an impression at which (over) pressure piping occurs.

Ad H) Flow rate sensor

An acoustic flow rate sensor measures the flow rate of the nozzle; the actual flow rate displays on the digital computer of the sensor.

Ad I) Centrifugal pump

The centrifugal pump, transports the water from the reservoir into the aquarium. The flow rate varies, by using a bypass flow; the bypass flow inserts the water direct into the water reservoir.

Ad J) Conductivity probes and Data acquisition material

Two conductivity probes are used in the experiments for the fluidization and density measurements in at two positions in the bed. The conductivity probes consists of 10 measuring points, the distance between two measuring points is 40 mm. Each measuring point consists of two bolts; with the distance between the bolts is 5mm.

The conductivity probes measures on the principle of electrical conductivity. An electrical flow between the two bolts measures the conductivity through the carrying fluid. The electrical current in the carrying fluid experiences resistance if the carrying fluid contains nonconductive solid particles. In the absence of nonconductive particles, the current flows directly towards the other bolt. In a mixture, the current is forced to change course and take (different) longer paths before reaching the other electrical bolt. The higher the concentration of the mixture the more particles in the liquid, the more obstacles and therefore the more resistance the electrical current experiences. Higher concentration of solid particles (sand) delivers lower measuring voltages.

The conductivity probes measures the density of the mixture, the erosion and the fluidization velocity of the water jet. The conductivity probe sends the measured voltage to the conductivity meter CCM (Conductivity Concentration Meter), which in its turn sends the voltage to the amplifier. Each CCM has 15 connection ports; the CCM tuner is set to 333 for all amplifiers in all experiments. The amplifier has 64 ports and connects the CCM to the computer. The conductivity probes, CCM, amplifier and other required material for the use of the conductivity probes are hired from Deltares, The Netherlands.

FIGURE 5.5 CALIBRATION PIPE

Calibration of the conductivity probes

The calibration of the conductivity probes is based on the hindered settling process of the particles and is executed in a (closed) PVC pipe, see figure 5.5. The calibration pipe consists of a rubber topping; this top has a hole in which the conductivity probe fits. The bottom of the calibration pipe has a valve; this valve functions for the addition and removal of water and sand. For each of the conductivity probes the calibration is conducted according to the following procedure:

Insert the probe from the topside. The conductivity probe gives non-reliable measurements when the distances of the measuring points and the pipe wall differs. In order to keep the same distance between the measuring points and the pipe wall, an additional nonconductive obstacle is positioned at the end of the probe, the radius between the pipe wall and the conductivity probe must remain similar in all times. Measure the conductivity of air. Wash the sand, in order to remove all the ions

in the sand. Dry the sand in an oven to reduce the possibility of moisture in the sand, which gives extra weight to the sand. Fill the calibration pipe with tap water, measure the conductivity of the water. Measure the weight of the sand and fill for instance 6-volume percent sand in the (measured volume) of the pipe. Turn the calibration pipe up and downwards in order to trigger the hindered settling process and create a homogenous mixture. Observe and track the actual values of the measured data, for all the 10 measuring points simultaneously. At a certain moment the measuring points converge to a certain voltage; at this point, the mixture is approximately homogenous. The converging of the measurements is more obvious for higher concentrations. Repeat these steps until the no sand fits into the pipe. The calibration tests for different concentration of the $D_{50} = 130\ \mu m$ delivers a linear approximation of the concentration as a function of electrical conductivity.

The conductivity of air (highest electrical resistance) and the conductivity of the carrier liquid (lowest electrical resistance) are the extremes for the linear calibration curve. For the calibration study for each measuring point, see appendix: calibration curves. For more in depth and detailed information about the calibration and the conductivity probes study the work of Nasr el Din(1985), van Wijk(2015).

Data acquisition

The conductivity sensors and the data acquisition systems for the data acquisition where hired from Deltares, Delft, The Netherlands. Each measuring point has an individual acquisition point. This gives 10 acquisition points for each sensor. The software needed to transform the data is a special in house built software by Deltares, delft Measure (version 7.01).

FIGURE 5.6 MEASURING COMPUTER AND THE CCM CONNECTIONS

5.2 Test Execution

In order to understand the influence of the jetting parameters on the fluidization process, the jet flow rate, jet pressure and jet diameter are varied. The initial bed conditions are for all the experiments equal.

Procedure per experiment

- Determine the jet pressure and the flowrate.
- Determine the jet diameter.
- Fill the aquarium with water up to the overflow level.
- Closing the jet valve (full with water).
- Refill the sand until 530 mm above bottom.
- Give the sand bed approximate 20 minutes settling time.
- Compacting the sand bed.

Starting and ending experiments

- Position the camera
- Indicate the experiment number on the viewing section.
- Start the centrifugal pump.
- Open the water valve.
- Track the erosion process
- Draw the shape of the fluidization pit on the viewing section.
- Close the jet valve.
- Shut the centrifugal pump

The experiments contains compacted and uncompacted tests. The sand bed is compacted by a vibrator with a needle length of 1m. In a systematically pattern the sand is vibrated for approximate 20 seconds. The vibration process starts when the needle touches the bottom of the aquarium. It is important to lift the needle slowly out of the bed; this increases the homogeneity of the bed layers. In order to gain similar bed conditions, the vibration points needs to be at the same locations and endure approximate for the same period.

In the experiments, is noticed that the sand compaction has a great influence on the piping location. Compacting the sand increase the bed resistance for deformations. Water flows in the direction in which it experiences the smallest resistance. It is therefore more likely that piping occurs at the uncompacted bed locations. It is important to maintain the same vibration pattern and duration; this delivers for each experiment approximately the same initial be conditions.

5.3 Variables

- Jet pressure
- Jet flow rate
- Jet diameter
- Hydraulic power
- Sand bed height

In the experiments 3 pressure levels, 4 nozzle diameters and 5 different flow rates are varied.

Jet pressure
Jet pressure variates the jet power, discharge velocity and therefore the flow rate of the nozzle. The pressure levels of 1bar and 4bar are studied. In this way, the influence of a relative low pressure and relative high pressure is tested for the understanding of the influence of the pressure on the erosion and fluidization process.

Jet flow rate
The jet flow rate depends on the nozzle diameter. At constant pressure, increasing the jet diameter delivers higher flowrates. At constant diameter and higher pressures, the flow rate increases. Inserting different flowrates gives understanding of the influence of the flow rate on the erosion and the fluidization process.

Jet diameters
Using different nozzle diameters gives the advantage to increase the jet flow at constant pressure. A larger nozzle diameter gives a more divergent flow pattern and therefore influences a larger fluidization area (Bindt 2002).

Hydraulic power
Hydraulic power is derived from the jet pressure and the jet flowrate, at constant hydraulic power the influence of the jet pressure and jet flow rate is studied.

Bed height
The bed height in all experiments is approximate 530 mm above the bottom.

5.4 Definitions for quantification of fluidization

FIGURE 5.7 DEFINITION SKETCH OF THE JETTING DEFINITIONS
The length dimensions are in millimeters [mm]

For the understanding of the influence of the jetting parameters on the fluidization of the bed and for the sake of accurate comparisons, the following definitions are introduced:

- The averaged front velocity from the nozzle to probe L, V_1 $[\frac{m}{s}]$
- The averaged front velocity from the nozzle to probe K, V_2 $[\frac{m}{s}]$
- The averaged vertical front velocity over probe L, Vv_1 $[\frac{m}{s}]$
- The averaged vertical front velocity over probe K, Vv_2 $[\frac{m}{s}]$
- The required fluidization time for area A (figure 5.7), t_A $[s]$

The definitions give the ability to compare the influence of the jet parameters on the fluidization process in a constant sand volume. The first experiment in the experimental matrix is elaborated in the next paragraph; the elaboration describes the defined parameters into more detail.

FIGURE 5.8 LEFT, TOP VIEW OF THE AQUARIUM, RIGHT FRONT VIEW OF THE AQUARIUM WITH NOZZLE AND CONDUCTIVITY PROBES; P REFERS TO THE LOCATION OF THE PRESSURE SENSOR.

Positions of the sensors in the aquarium

The nozzle is positioned against the transparent wall, the distance between the nozzle and the transparent wall is equal to the radius of the nozzle housing, in this case approximate 25mm. The nozzle is positioned on a metal base 110mm above the bottom and approximate 330mm distance from the left wall of the aquarium. The distance between the nozzle, probe K and probe L remains constant for all experiments. The distance between the nozzle and probe L is 0,30m, the distance between the nozzle and probe L is 0,6m. The conductivity probes are fixed at the top and bottom of the aquarium, the measuring points of the conductivity probes are directed towards the nozzle flow (Nasr el Din et all, 1986). The probes are fixed at 20mm above the bottom and 40mm distance from the transparent wall, the probes are in line with the nozzle flow.

The (diaphragm) pressure sensor is positioned at the back wall of the aquarium, (by drilling a hole of 9mm and welding the sensor at the wall), see figure 5.1. The width of the aquarium is approximate 330mm, the location of the pressure sensor is 110mm above the bottom and 600mm from the left wall of the aquarium, see letter P in figure 5.5 and 5.8.

5.5 Phenomenological description of the jetting process

The experiment is build according to the steps described in paragraph 6.2, when the jet starts inserting water in the bed, a small fluidized opening initiates in front of the nozzle. The opening starts growing in volume and after a few seconds a sphere shaped fluidized area forms in front of the nozzle. The inserted water, which cannot escape, builds an over pressure in the bed and keeps increasing the pressure in the bed, therefore the bed starts expanding and the inserted water starts lifting the upper sand layer. After a few seconds, the jet penetrates deeper in the bed and the fluidized area becomes a mushroom shape, while the jet keeps inserting water in the bed, the fluidized volume decreases in the horizontal front velocity and starts growing in the vertical direction, the mushroom shape grows in the vertical direction and changes to an oval shape. At a certain moment the overpressure in the bed becomes large enough to penetrate through the soil and

from an open channel to the surface, this is known as 'piping'. The overpressure, caused by the inserted water in the bed escapes through the piping channel. From this moment, primarily the upper surface of the bed (in the reach of the nozzle) fluidizes completely. When water flows out of the channel the direct area of the open channel fluidizes instantly. The un-fluidized soil with a higher density flows downwards in the mixture of the jet-fluidized area, dissolves rapidly and becomes a part of the mixture. After piping, the jet excavates in a faster rate deeper in the bed, until the maximum excavation depth is reached, from that moment the jet starts eroding upwards, eroding the walls of the pit, see figure 5.9 (test 18 of table 6-1) and figure 5.10 (test 13 of table 6-1).

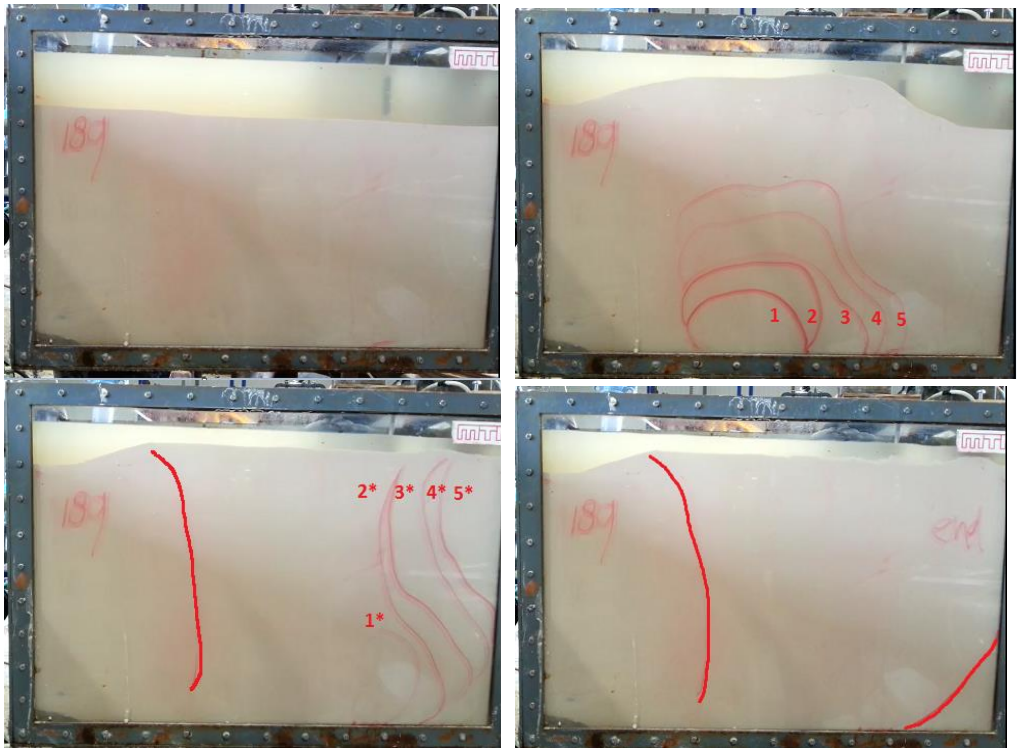

FIGURE 5.9 JETTING PHASES IN THE BED, TOP LEFT INITIAL BED CONDITION, TOP

[redacted]

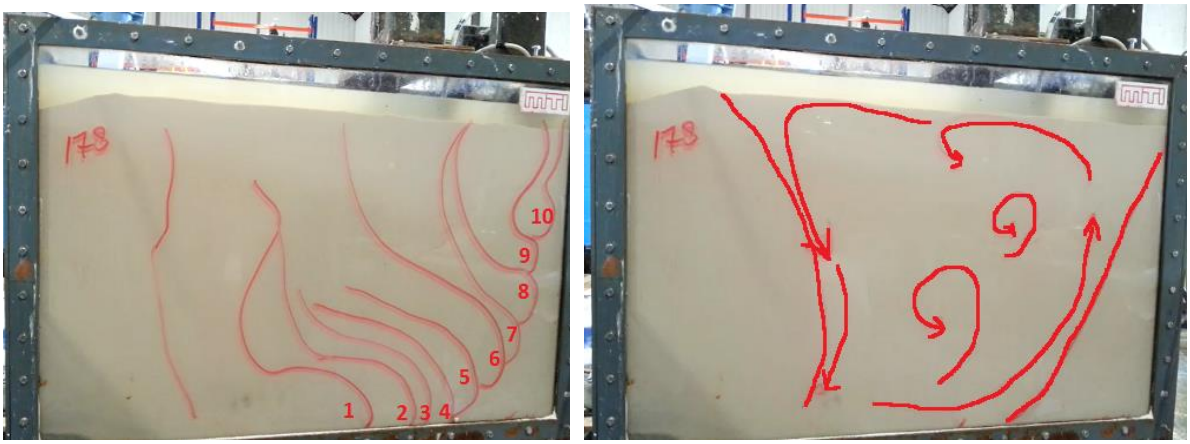

FIGURE 5.10 FIGURE LEFT DESCRIBES JETTING PROCESS AFTER PIPING (EXPERIMENT 13 OF [redacted]

5.6 Test Matrix.

TABLE 5-1 EXPERIMENTAL MATRIX
H,BED: THE BED HEIGHT, DN: NOZZLE DIAMETER, Q: JET FLOW RATE, P HYDRAULIC POWER, V1 FRONT VELOCITY PROBE L, V2 FRONT VELOCITY PROBE K, VA FLUIDIZING AREA A, VV VERTICAL FRONT VELOCITY FOR PROBE L AND PROBE K.

Nr [-]	H,bed [mm]	Dn [mm]	p [bar]	Q [L/s]	P [W]
1	530	7	4,00	0,78	312
2	530	7	4,00	0,78	312
3	530	7	4,00	0,78	312
4	530	7	1,34	0,53	71
5	530	7	1,34	0,53	71
6	530	7	1,34	0,53	71
7	530	7	0,21	0,18	4
8	530	6	4,00	0,53	212
9	530	6	4,00	0,53	212
10	530	6	4,00	0,53	212
11	530	6	1,22	0,37	45
12	530	6	1,22	0,37	45
13	530	6	0,46	0,22	10
14	530	5	4,00	0,4	160
15	530	5	4,00	0,4	160
16	530	5	1,00	0,22	22
17	530	5	1,00	0,22	22
18	530	3	4,00	0,17	68

The jetting parameters where tested in compacted and uncompacted sand conditions. The density difference between compacted and uncompacted sand is relatively small. The minimum and maximum wet density has been determined, according to the prescription of MTI**.** The determined density for the compacted sand is approximately $\rho_c = 1998\frac{kg}{m^3} \approx 2000\frac{kg}{m^3}$, the density of the uncompacted sand is approximately $\rho = 1940\frac{kg}{m^3}$. The uncompacted experiments delivered unreliable results. The compacted sand experiments reduces the pores in the bed, creates a more homogenous and structured bed skeleton. This is explained as follows: due to the non-spherical shape of the sand the particles settles each experiment under different configurations on the bed, each settling process creating a different bed skeleton with, therefore the results for the erosion velocity differ significantly for each experiment.

5.7 Elaboration of the first experiment.

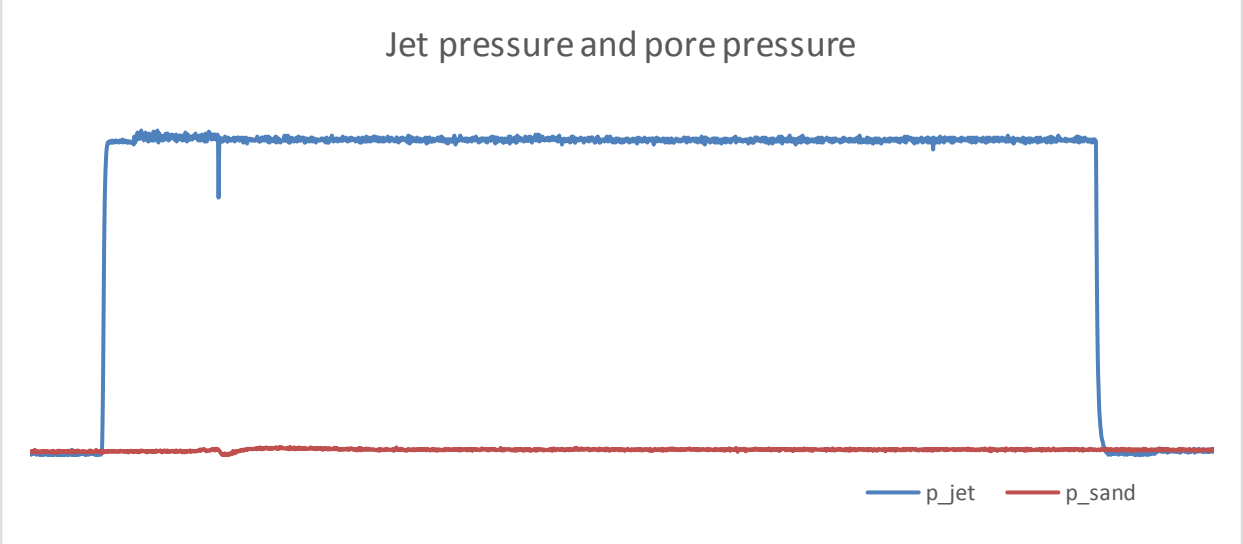

FIGURE 5.11 JET AND PORE PRESSURE DEVELOPMENT

Figure 5.11, shows the jet pressure and the pore water pressure development in the sand bed. The pore pressure fluctuations are small, compared to the jet pressure and there the pore pressure is close to the horizontal axes. See figure 5.12**,** for a clear view on the pore pressure development. The pump operates at t=13 seconds, at this timeframe the pressure immediately increases to the maximum head of the pump, $p = 4bar$. At t=35 seconds the pressure in the jetting pipe drops suddenly to 3 bar, this is the moment when the jet valve is opened and the jetting process is initiated. At t=200 seconds the jet pressure drops to zero, at this time the centrifugal pump is not operating anymore.

Figure 5.11, zooms on the pore pressure development. At approximate t=36 seconds the pore pressure drops and quickly recovers, this is explained by the fact that the densely packed sand experience deformations, causing dilatation around the point where the jetting process is started.

Therefore, the water flows towards the sheared zones and the pressure decreases slightly, causing a small fluctuation between t=35s and t=38s. The maximum pore pressure occurs between t=38 and t=60 seconds, this period describes the fluidization prior to the piping process. It is inevitable to assume that the peak at t=45 seconds describes the moment of piping, but this is not the case, video recordings of experiment 1 showed that piping occurs after 27 seconds of jetting, this means that the jet is inserting water and expanding the sand bed until approximate $t = 35 + 27 = 62s$. Piping occurs when the overpressure in the sand bed is large enough to compensate the hydrostatic pressure of the bed height at the jet level. Initially when the jet starts, the inserted water forms a ''mushroom'' shape in the sand bed. This takes approximate 15 seconds, after 15 seconds, the mushroom form is increasing in the vertical direction, causing the water to move away from the location of the sensor and creating more area for the water to divide the pressure. This explains the measured peak at t=45 seconds.

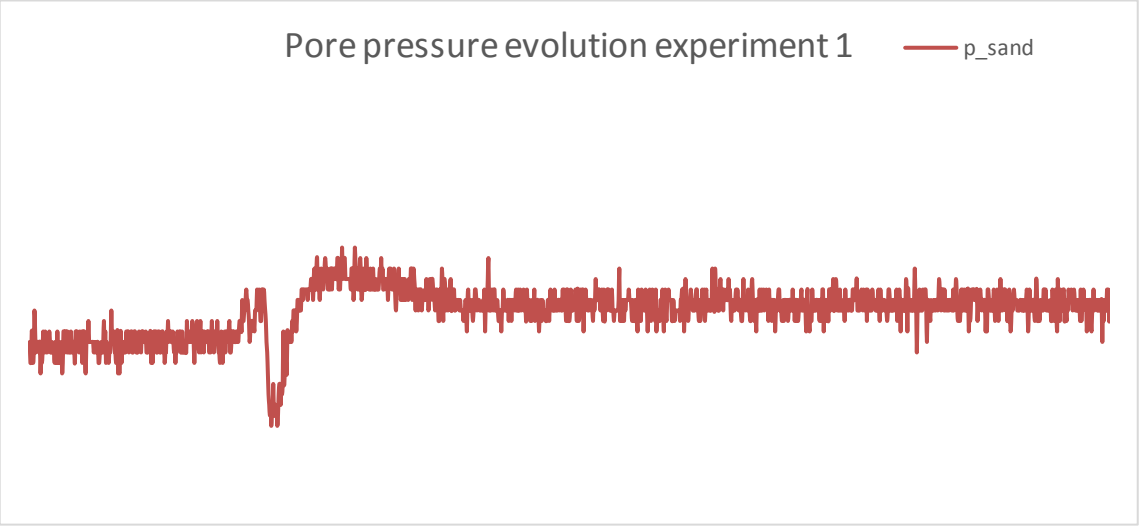

FIGURE 5.12 PORE PRESSURE DEVELOPMENT OVER JETTING TIME

Compacted density of the sand bed

The experiments for uncompacted sand starts with 530mm bed height and a density of $\rho \approx 1940 \frac{kg}{m^3}$. After compaction, the sand bed reduced approximately 15 mm resulting in a bed height of 515mm, with a compacted density of $\rho_c = 2000 \frac{kg}{m^3}$. The density difference gives $\Delta\rho = 2000 - 1940 = 60 \frac{kg}{m^3}$, expressing in fractions gives $\frac{60}{1940} * 100 \approx 3{,}1\%$. $3{,}1\% \, of \, 530mm = 16.2mm$, this simple calculation confirms that the compacted density of the bed approximates a compacted density of $\rho_c = 2000 \frac{kg}{m^3}$.

5.7.1 Theoretical and measured values of the pore pressure sensor.

The hydrostatic pressure for the compacted and uncompacted sand bed at the level of the pore pressure sensor gives:

$$p_{hydr} = \rho\, g\, \Delta h = 1940 \cdot 9.81 \cdot (530 - 110) = 0.08\, bar$$

$$p_{hydr,c} = \rho_c\, g\, \Delta h = 2000 \cdot 9.81 \cdot (530 - 110 - 15) = 0.08\, bar$$

Prior to fluidization, figure 5.12 gives a measured pore pressure of $\Delta p = 0{,}06 bar$. After the piping process ($t > 60\ seconds$) and during the fluidization process ($60 < t < 160$), the pressure $p = 0{,}08 bar$. The pressure difference is $\Delta p = 0.08 - 0.06 = 0{,}02\ bar$ this pressure difference describes the weight of the submerged particles. The fundamental equation for fluidization describes:

$$\frac{\Delta P}{L} = (1 - \varepsilon)\ (\rho_s - \rho_w) g \qquad \textbf{5.1}$$

The measured mixture density during the experiments is in between $1500 \frac{kg}{m^3}$ and $1600 \frac{kg}{m^3}$. Assuming $\rho_m = 1550 \frac{kg}{m^3}$ and a mixture level equal to the overflow level gives:

$$\Delta P = (1 - \varepsilon)\ (\rho_s - \rho_w)\ g\ L = 0{,}33 \cdot 1650 \cdot 9.81 \cdot (0.600 - 0.110) = 0.026 bar.$$

Comparing to the measured value of 0.02 bar gives a good approximation of the actual value. The theoretical and measured values are close to each other.

The maximum measured pressure reads $p_{sand} = 0.105 bar$, the calculated hydrostatic pressure gives: $p_{hydr,c} = 0.08\ bar$. Theoretically, it is expected that compensating the hydrostatic pressure leads to piping. However, compacting the sand makes the sand skeleton more resistant to deformations. Sand is not spherical, compacting the sand forces the sand particles into each other. During the fluidization, when the sand bed expands, the sand increases approximate 100mm above the initial bed before piping occurs. This property of the compacted sand therefore requires more pressure to initiate the pressure calculated from the fundamental pressure for fluidization.

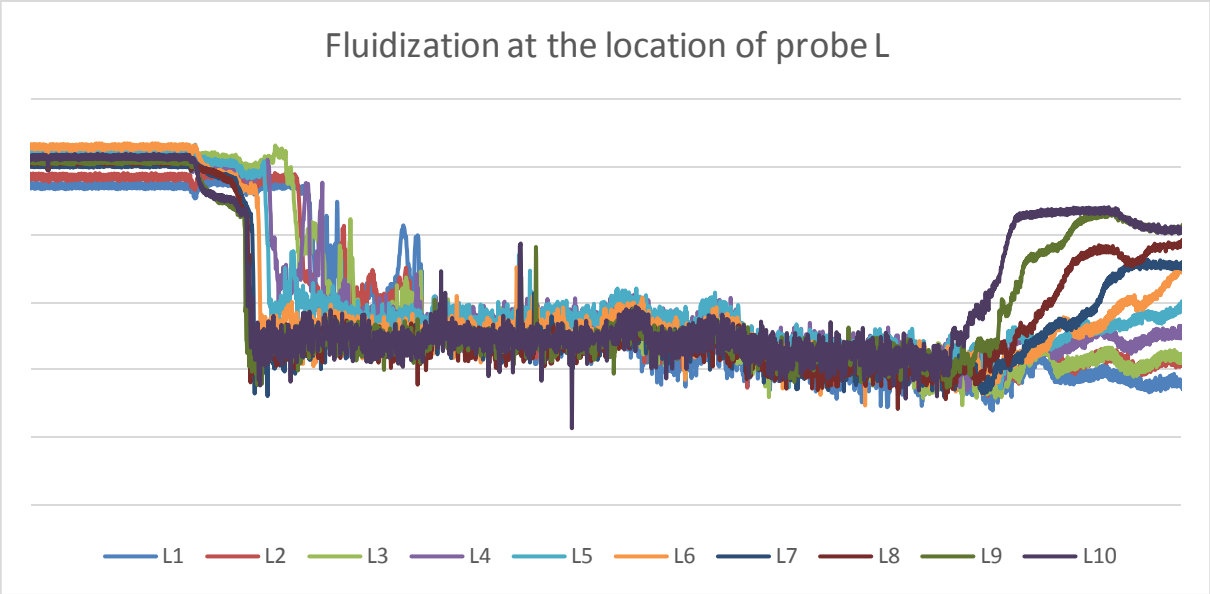

FIGURE 5.13DENSITY DEVELOPMENT FOR PROBE L

At t= 35 seconds the jetting process with a pressure of 4 bar a nozzle diameter of 7mm and a flow rate of 0,78L/s is initiated. The period t < 40 seconds, describes the density of the bed prior to the jetting process. Figure 5.13 global development of the fluidization process at location of probe L (0,3m distance from the nozzle), for all the ten measuring points of probe L. At t=47 seconds the jet water travels a distance of 0,300m in the sand and reaches the first measuring point L_{10}. This front velocity V_1 is the averaged velocity from the nozzle to the location of probe L.

$$V_1 = \frac{S_1}{\Delta t} = \frac{0.300}{t_{jet} - t_{L10}} \qquad \textbf{5.2}$$

The parallel inclining lines between 47s < t < 60s in figure 5.13, describes the jet water fluidizing the measuring points of probe L. This happens in all experiments at the same order, starting from L_{10} and ending with L_1. This fluidization process describes the vertical fluidization up to 0,4m above the bottom. The required time to fluidize the vertical height of probe L is approximate 60-47=13seconds. The vertical front velocity V_{v1}, is the averaged velocity for the fluidization over the total length of probe L, which is $0{,}4m$. De definition of the vertical fluidization is:

$$V_{v1} = \frac{S_3}{\Delta t} = \frac{0{,}400}{t_{L1} - t_{L10}} \qquad \textbf{5.3}$$

At approximate 85s, all measuring points converge to a homogenous density $\rho_m = 1500\frac{kg}{m^3}$. At t > 130 seconds, the density of the mixture linearly decreases. During the jetting process, the jet continuously inserts water into the system, due to the overflow losses, the amount of sand decreases. The overflow starts transporting sand from the moment piping occurs. The overflow loss explains the density decrease in figure 5.13.

At t=200 seconds the jet is closed and the mixture is settling down. Figure 5.13 shows that the lowest measuring point L_{10} is the first point and that other measuring points are following at backward chronological order, which is convenient for the sedimentation process.

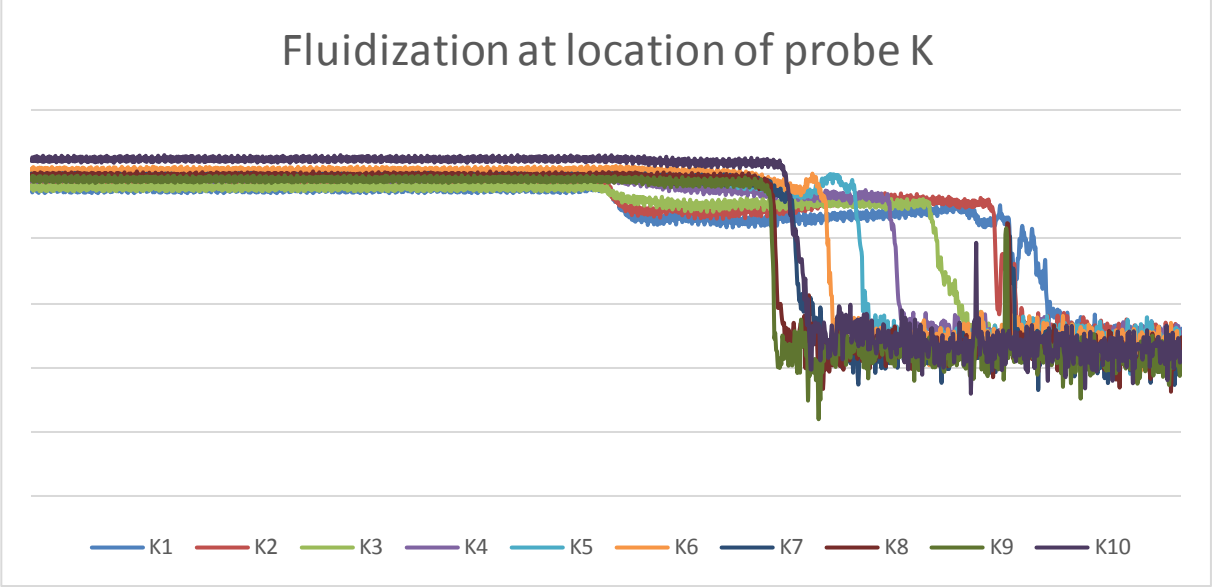

.

FIGURE 5.14 DENSITY DEVELOPMENT FOR PROBE K
Fluidization occurs from the moment the horizontal lines changes to a vertical line. K_{10}starts decreasing density from t=83s. This is the moment when the jet flow reaches the probe.

Figure 5.13, zooms on the fluidization process of probe L. At t=83 seconds, the water flow reaches the point K_{10}, at this time the jet water traveled a distance of 0,600m from the nozzle. The averaged front velocity over a distance of 0.6m from the nozzle is defined as:

$$V_2 = \frac{S_2}{\Delta t} = \frac{0.600}{t_{jet} - t_{K10}} \qquad \textbf{5.4}$$

At t=65 seconds, K_1 and K_2 obtain lower densities. The jetting process initiates the water flow at t=35 seconds, at t=65 seconds the jet already inserted for 30 seconds water in the bed. The fluidization of K_1 and K_2 prior to the fluidization of K_{10} verifies that the fluidization of the soil initially occurs at the upper layers of the soil.

The sand in the experiments has a nearly monochromatic particle distribution with a particle diameter $D_{50} = 130\mu m$.

The vertical front velocity for probe K is defined as:

$$V_{v2} = \frac{S3}{\Delta t} = \frac{0{,}400}{t_{L1} - t_{L10}}$$

Fluidization time for the area A.

Area A, see figure 5.9, is defines as the distance between the nozzle and probe K, multiplied by the vertical height of the measuring length of the conductivity probes, giving area $A = 0{,}6 \cdot 0{,}4 = 0.24m^2$. This area indicates the required time needed to fluidize a certain area. This area is assumed fluidized when probe L and K are both are fully fluidized over the vertical height. Since the area above the nozzle is the first fluidized area this area is also taken into account in area A given in figure 5.9

5.8 Analysis of the experimental results

The measurements for the probes, delivers for all experiments similar developments, as shown in figures 5.13 and 5.14. Different jet pressures and jet flow rates delivers different fluidization velocities. These differences are expressed in the experimental matrix; the results differ mainly on the fluidization velocity for each experiment. All experiments describes three main phases, see figure 5.13**:** the fluidization phase, between 47 < t < 60 seconds, the equilibrium phase (60s < t < 200s) and the settling phase (t > 200s).

The jet flow and jet pressure influences the front velocities V_1, V_2, the vertical fluidization velocities Vv_1 and Vv_2 and the fluidization time over area A. The main difference between the experiments is the time in which the parameters occure and whether the jet parameters are sufficient to reach and fluidize the distances up to probe K and L.

The matrix shows experiments where the fluidization parameters of probe K is missing. For these cases, the jet specifications where unable to fluidize the entire vertical length of probe K. In some tests a few points where fluidized, especially in experiments with stump pit angles, where in most of the tests the highest 3 measuring points where fluidized. For the sake of clarity and simplicity, these values are omitted.

When the fluidization pit becomes in a more or less equilibrium state it describes a homogenous density, between $\rho_m = 1500\frac{kg}{m^3}$ and $\rho_m = 1600\frac{kg}{m^3}$. Extending the jetting period leads to lower equilibrium densities, due to the net inflow of water and outflow of solids. For all experiments, the sedimentation process, after fluidization occurs in the same order and approximate in the same period. The scope of the study focuses on the erosion between probes K and L and the fluidization velocity between the probes.

5.8.1 Comparison of jet cavity equilibrium with results of Maas(1992)

The particle diameter used in this study is approximate $D_{50} = 130\ \mu m$, Maas conducted experiments with a particle diameter of $D_{50} = 120\ \mu m$, the particle size difference is relative small. The experiments conducted by Maas, showed the equilibrium state of the jet trench after approximate 30 minutes jetting. Maas used a larger testing facility, which made it possible to investigate the jet trench in three dimensions. The first 5 experiments executed bij Maas delivered jet trenches obtained in the first 5 minutes of jetting. The results shows much similarity for the fluidized trench shapes. The cross sections area of the fluidized trenches for the experiments with a pressure of p=1bar and a flow rate of Q=0.22 L/s where compared with the estimated trench shape areas delivered by Maas. Test numbers 16 and 17 of this study are compared with test numbers 14, 15, 26 and 27, of the experimental results delivered by Maas. These experiments contain similar jetting specifications, the fluidized trench areas in equilibrium, delivers similar trends for the total fluidization area.

Comparing the cross sectional area

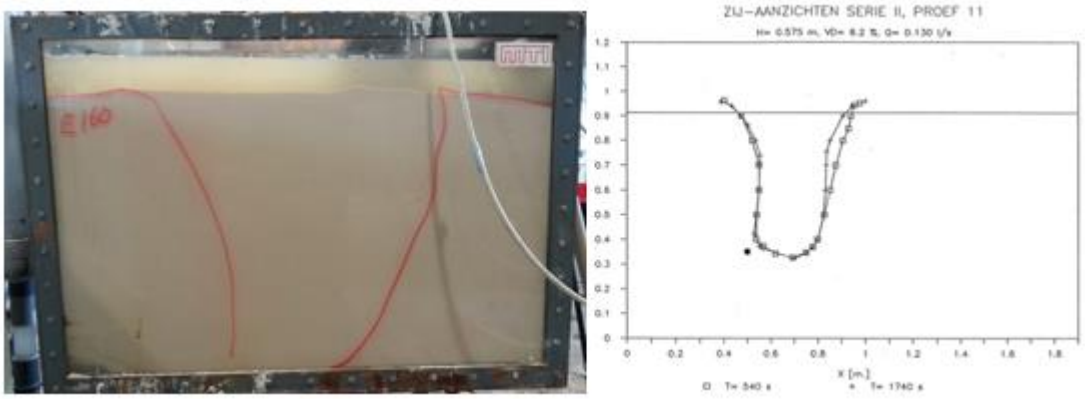

FIGURE 5.15 COMPARISON OF THE CROSS SECTION AREAS WITH THE ESTIMATIONS OF MAAS

The total bed height of the aquarium is approximate 530mm, the bed height in the experiments of Maas is approximate 900 – 350=550m, the difference in bed height is approximate 20mm. This makes it possible to compare the cross section of the fluidized trenches of the experiments of Maas and the results in the aquarium. Estimating the cross section area of Maas delivers approximate $0.21m^2$. The Width of the aquarium is 1m, the bolts in the bottom of the aquarium have a distance of approximate 75mm, the bed height in case of partially fluidized bed (figure 5.15 left) remains approximate 530mm, this delivers an estimated cross sectional area of $0.18m^2$. This delivers a good approximation of the results of Maas. The Aquarium has a small width (0,33m), this restricts to measure the width of the fluidized trenches, the fluidized trench dimensions approximated by Maas are assumed to be similar as the jetting results of the first series experiments, the scope of this study, is gaining understanding in the influence of the jetting parameters on the fluidization velocity.

The maximum horizontal penetration depth obtained by the Maas is approximately 1.0m, for d=12mm, Q=1.0 L/s, p=0.68bar and P=59 W, (experiment 33). This depth is obtained for the highest flow rate and the second highest value for the hydraulic power.

5.9 Results

The findings and analysis in this paragraph is based on the results in the experimental matrix. The figures for probe K contain less data points; some jet specifications do not reach the required threshold value to overcome the distance of probe K. This paragraph describes the results for each parameter separately.

5.9.1 Jet pressure

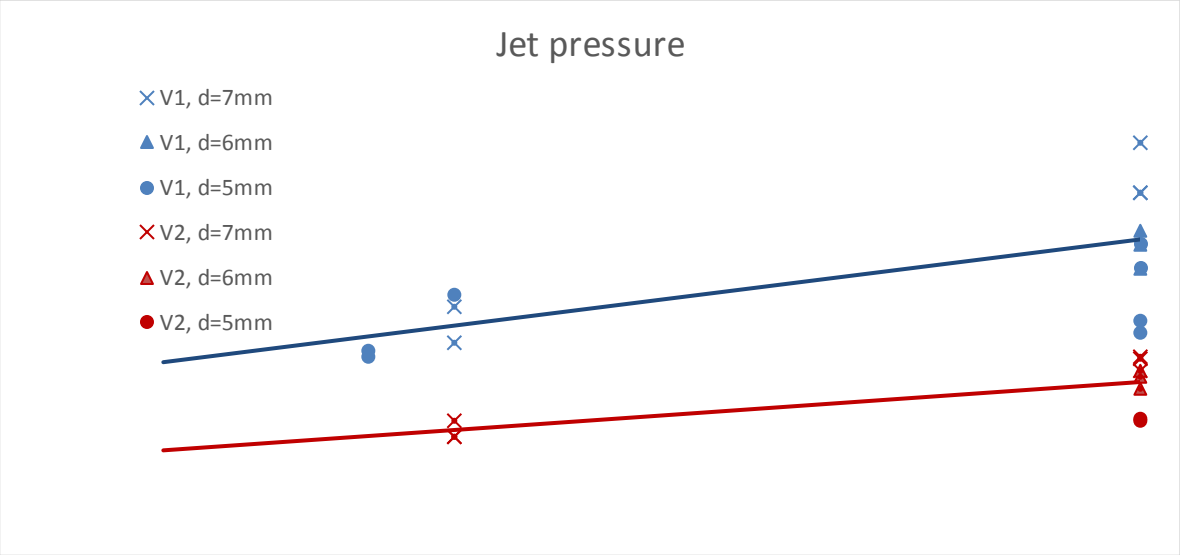

FIGURE 5.16 INFLUENCE OF THE JET PRESSURE ON THE FRONT VELOCITY V1 (BLEU) AND V2 (RED). V1 IS THE FRONT VELOCITY 0.3M FORM THE NOZZLE AND V2 0.6M FROM THE NOZZLE. THE HIGHEST FRONT VELOCITIES AT CONSTANT PRESSURE IS ACHIEVED BY THE LARGEST NOZZLE DIAMETERS.

The influence of jet pressure

Figure 5.16, shows that increasing the pressures increases the front velocity. However, the front velocity significantly reduces between probe K (red) and probe L (blue). Pressure values less than 1.3 bar do not reach probe K. Increasing the pressure increases the front velocity. At constant pressure of 4bar, larger diameters deliver higher flow rates and therefore higher hydraulic power values, leading to higher front velocities. The front velocity V_2 significantly reduces over distance. The ratio between V_1 and V_2 is approximate $\frac{Ve_1}{Ve_2} = 3$.

5.9.2 Constant flow rate and different pressures

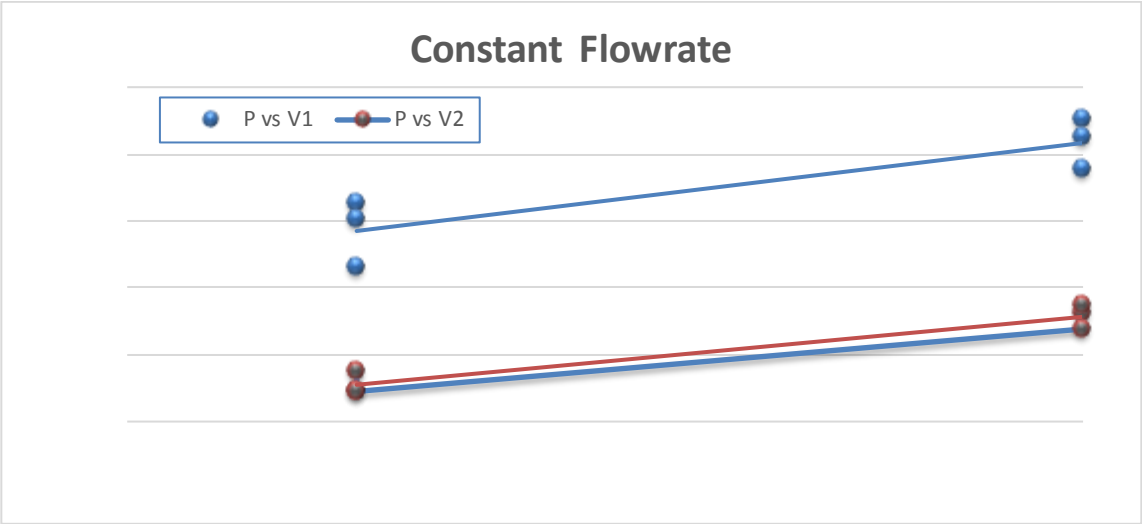

FIGURE 5.17 INFLUENCE OF CONSTANT FLOW RATE OF $\mathbf{Q = 0.53\frac{L}{s}}$, ON THE FRONT VELOCITIES V_1 AND V_2.

The front velocity ratio remains approximately $Ve_1/Ve_2 = 3$ and increases (linear) parallel between probe K and probe L

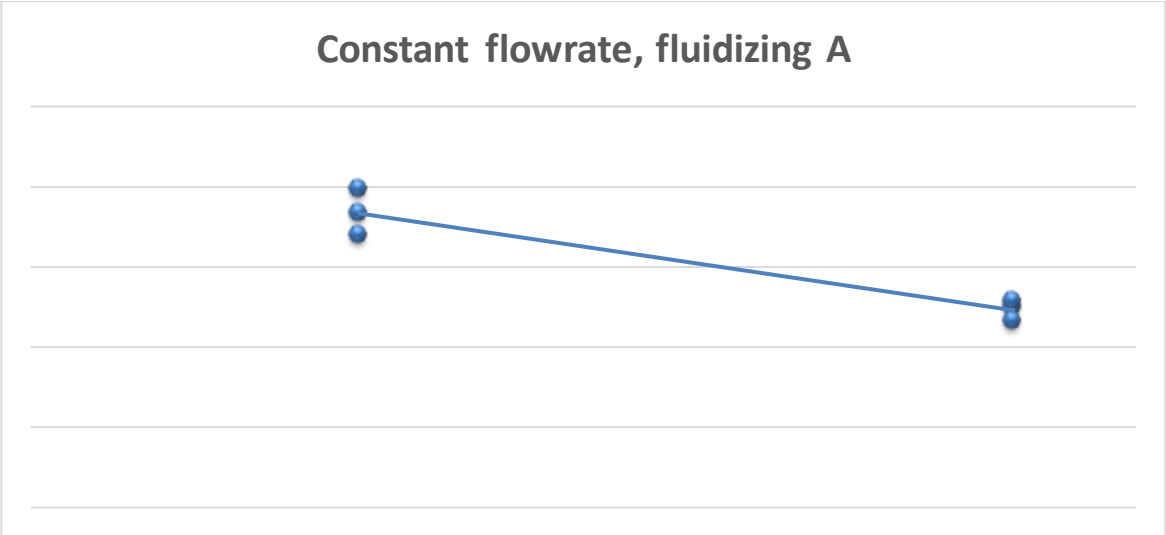

FIGURE 5.18 INFLUENCE OF CONSTANT FLOW RATE OF $\mathbf{Q = 0.53\frac{L}{s}}$, ON THE FLUIDIZATION TIME FOR TOTAL AREA A (DEFINED IN FIGURE 5.7).

A constant flow rate $Q = 0.53\frac{L}{s}$ and increasing the pressure delivers a significant faster fluidization time of area A. At p=1,3 bar the averaged fluidization time t=185s, at p=4 bar the fluidization time t=123s, this gives a time difference of Δt=62s. Which can be decisive for the prototype.

Influence of jet pressure at constant flow rate.
Keeping the flowrate constant and varying the jet-pressure, gives a better understanding of the influence of the pressure on the fluidization process. Figure 5.17 shows the influence of the jet-pressure on the front velocity. Increasing the jet pressure increases the fluidization velocity significantly. Expressing the fluidization time for area A2 in seconds, between p=1.3bar and p=4bar gives a difference of approximate 60seconds. This time interval is significantly higher and can make big differences for the offloading times on large scale.

The front velocity increases linear for higher jet pressures, see figure 5.17.

Experiments with the same flowrate and higher jet pressure delivers a higher front velocity and in the horizontal and vertical direction.

5.9.3 Flow rate

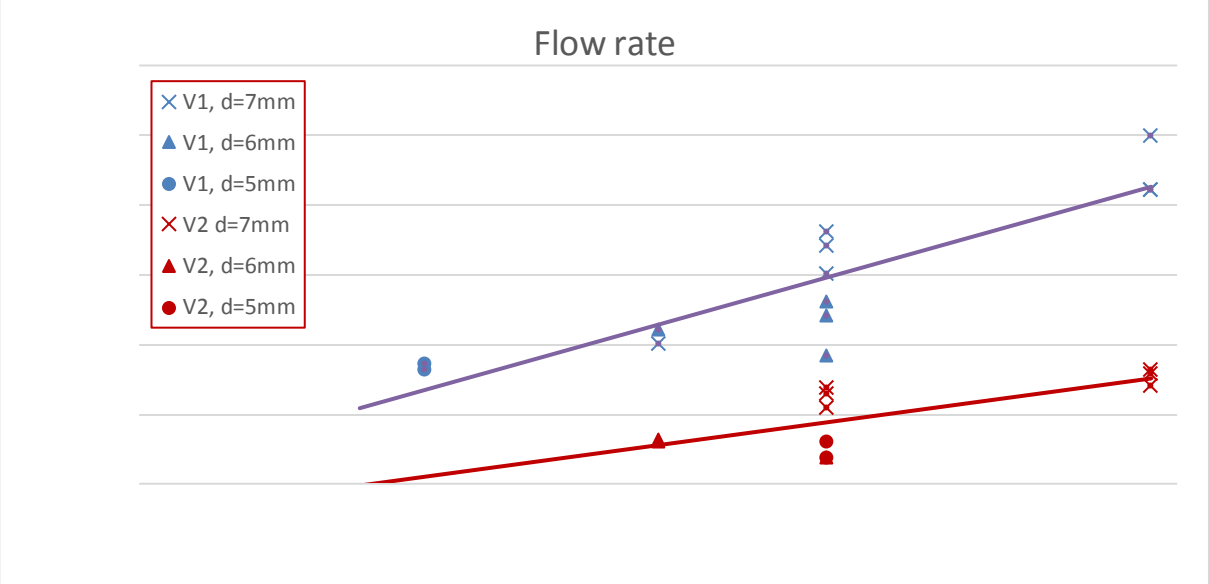

FIGURE 5.19 INFLUENCE OF THE FLOW RATE ON THE FRONT VELOCITY V1 (BLEU) AND V2 (RED). V1 IS THE FRONT VELOCITY 0.3M FORM THE NOZZLE AND V2 0.6M FROM THE NOZZLE. THE HIGHEST FRONT VELOCITIES IS ACHIEVED BY THE LARGEST (NOZZLE DIAMETERS) FLOW RATES.

Figure 5.19 shows at $Q = 0.53\frac{L}{s}$ that higher power at the same flow rate delivers higher front velocities. However, the difference in front velocity for higher flow rates and higher power at $Q = 0{,}78\frac{L}{s}$ shows that the front velocity does not increase significantly. This is further analysed at constant flow rate figures.

Influence of the flowrate on the front velocity

Figure 5.19 shows a linear relation between the flow rate and the front velocity, however the values on the line Q=0.53 are given for pressures p=1bar and p=4bar. In order to fluidize the area A, a minimum flow rate of 0.4 is required.

5.9.4 Constant pressure and different flowrates

FIGURE 5.20 INFLUENCE OF THE FLOW RATE AT CONSTANT PRESSURE P=4BAR ON THE FRONT VELOCITY V1 AND V2

Figure 5.21, shows that at constant pressure p=4bar and increasing flow rate the fluidization velocity V2 increases linearly.

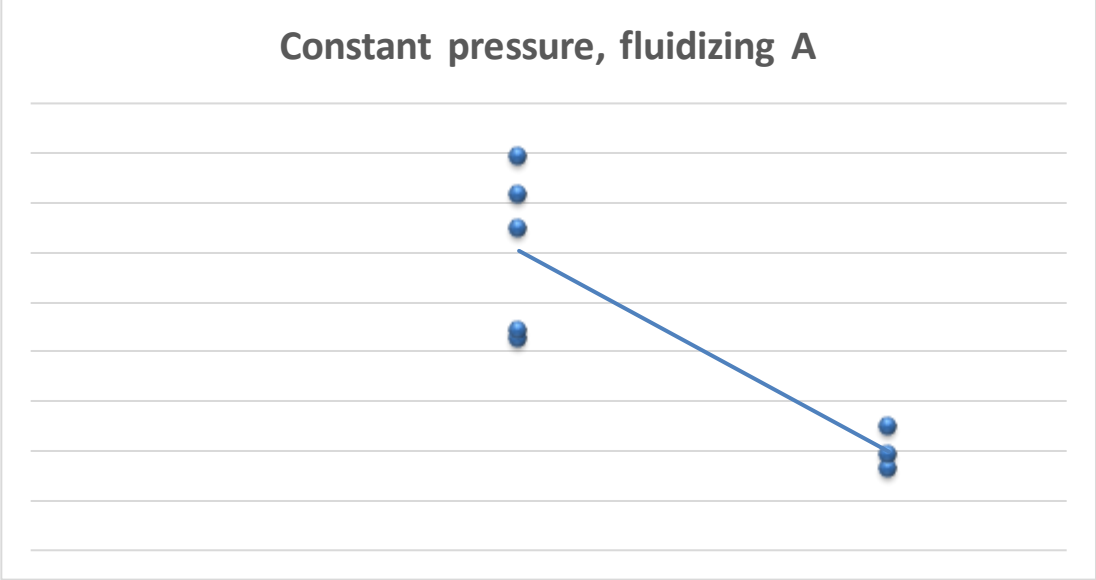

FIGURE 5.21 FLOWRATE AT CONSTANT PRESSURE P=4 BAR AGAINST THE REQUIRED FLUIDIZATION TIME OF AREA A.

At constant pressure p=4bar and increasing flow rate the fluidization time decreases linearly.

Influence of the flowrate at constant pressure

Increasing the flowrate at constant pressure delivers a linear increasing erosion velocity in the horizontal and vertical direction. These graphs confirms that the flow rate is more decisive for the fluidization velocity.

5.9.5 Hydraulic power

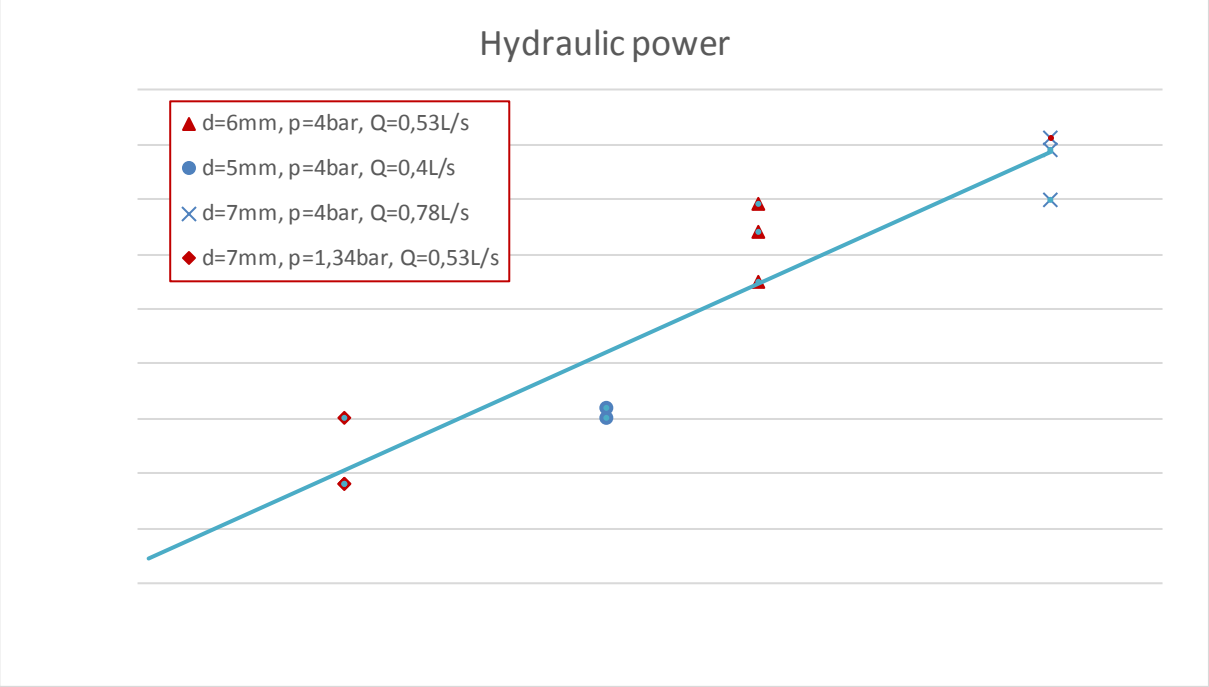

FIGURE 5.22 HYDRAULIC POWER AGAINST THE FRONT VELOCITY VE2, WITH PRESSURE INCREASE IN RED AND FLOW RATE INCREASE IN BLUE.

Figure 5.23 shows that increasing the hydraulic power increases the front velocity. A pressure level p=1.43 bar and Q=0.53 L/s delivers approximate similar front velocities as p=4 bar and Q=0.4 L/s, while consuming approximate two times more power. Increasing the pressure to 4 bar at constant flow rate of Q=0.53 L/s increases the front velocity in the order of two. Increasing the flow rate to Q=0.78L/s at constant pressure of 4 bar increases the front velocity. Increasing the pressure or the flow rate increases the hydraulic power and increases the front velocity. Based on the energy consumption it seems that increasing the flow rate is more convenient to increase the front velocity.

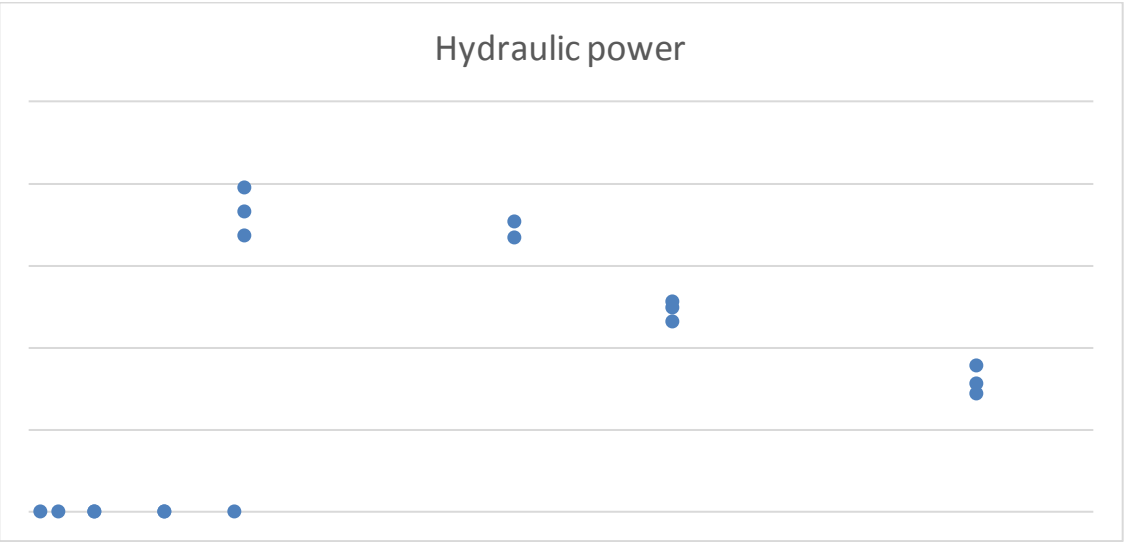

FIGURE 5.23 HYDRAULIC POWER AGAINST THE FLUIDIZATION TIME OF AREA A.

Jet hydraulic power

Figures 5.23 and figure 5.24 shows that hydraulic power has a linear dependence with the fluidization velocity in the horizontal and vertical direction in the bed. However, hydraulic power is a function of the flow times the pressure. Based on the individual analysis on the pressure term and flow term, the flow term is more decisive for the fluidization velocity. The analyses on pressure shows that the pressure influences the fluidization velocity, using higher pressures at constant flow rate increases the fluidization velocity.

5.9.6 Constant hydraulic power

The definition of the hydraulic power is jet-pressure times the jet flowrate. Experiments with approximate constant hydraulic power and different pressure and flow terms are studied. The following data of experiments 11-13 and 37 gives:

TABLE 5-2
COMPARING DIFFERENT PRESSURES AND FLOWRATES AT CONSTANT HYDRAULIC POWER

nr	H,bed	d [mm]	p [bar]	Q [L/s]	P [W]	V1 [m/s]	V2 [m/s]	A [s]	Vv1 [m/s]	Vv2 [m/s]
11	530	7	1,34	0,53	71	0,013	0,002	198	53	75
12	530	7	1,34	0,53	71	0,012	0,002	183	71	82
13	530	7	1,34	0,53	71	0,0092	0,003	169	61	67
37	530	3	4,00	0,17	68	0,0046	x	x	93	x

In these experiments, the pressures of approximate p=1bar and p=4bar are compared with the flowrates of $Q = 0.17\frac{L}{s}$ with $Q = 0.53\frac{L}{s}$. In this case the pressure of $p = 4bar$ and flow rate $Q = 0.17\frac{L}{s}$ did not succeed to erode the sand until probe K. These experiments confirms the conclusion of Maas, Maas concluded that the flow rate is of first order importance for the fluidization velocity and the pressure of second order. The video recordings and the data in table 7.2, gives that increasing the flow rate at constant hydraulic power increases the fluidization velocity. This finding again confirms the importance of the flow rate on the fluidization velocity.

5.9.7 Jet momentum

In the literature, some authors refer the jet hydraulic power as the most decisive parameter for the jet production (kg/s) and some authors the jet momentum e.g. Vlasblom, (van Rhee, 2016). The jet momentum is defined as $= \rho_w \; Q \; u = \frac{2\,P}{u}$. The jet momentum can be derived from the hydraulic power and therefore, shows similar trends as the hydraulic power, see figures 5.25 and 5.26 and compare with figures 5.23 and 5.24.

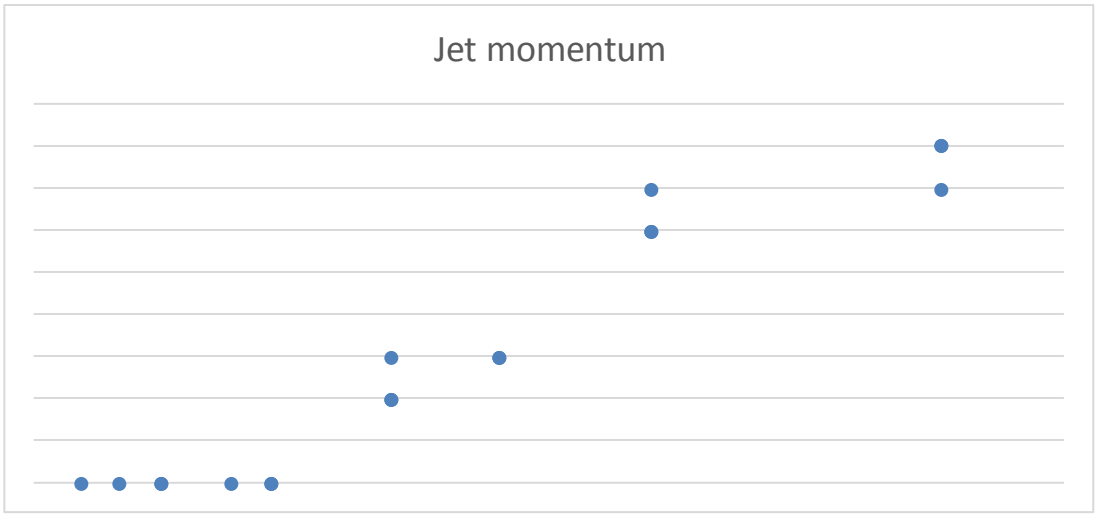

FIGURE 5.24 JET MOMENTUM AGAINST THE FRONT VELOCITY V2

FIGURE 5.25 JET MOMENTUM AGAINST THE FLUIDIZATION TIME OF AREA A.

5.10 Conclusions

1. Jet pressure is decisive for the fluidization velocity, higher jet pressures delivers faster fluidization over a certain volume.

2. The ratio between the jet erosion velocities reduces in the third order between 0.3m and 0.6m distance from the nozzle.

3. Increasing the pressure increases the fluidization velocity in the horizontal and vertical direction. Pressure is decisive for the speed of the fluidization process.

4. The fluidization area is linear dependent on the jet flow rate, higher flow rates increases the erosion velocity (linear) in the horizontal and the vertical direction of the sand bed.

5. The hydraulic power has a linear relationship with the fluidization velocity.

6. At constant hydraulic power, higher flow rates are more effective for the fluidization process.

6 Small scale hopper fluidization experiments

6.1.1 Introduction and Motivation for the experiments

The scope of the small-scale experiments is to test a combination of parameters, which are influencing the fluidization and the unloading process. By virtue of downscaling, these scaled experiments deliver the most representative results since all the parameters of influence are combined in the experiments. The combination of the findings of the literature review and the first series experiments resulted into the test parameters given in the experimental matrix of this paragraph. The significant parameters influencing the fluidization of the soil (jet pressure, jet flowrate, jet hydraulic power, pre-jetting times) and the unloading methods (dry sand conditions, constant water level, 1m water above the cargo, unloading flow rate) are tested in the small-scale hopper section. All the jetting parameters and the geometries are scaled according to the scaling rules and scaling parameters derived in chapter 6. The combination of the fluidization of the hopper cargo and the unloading of the fluidized mixture makes these experiments representative for the prototype. The testing parameters and trends leading to optimized unloading times, are very likely usable for the prototype scale.

6.2 Scale of the experiments

Scaling factor

The hopper section of the prototype has the dimensions, $(L \cdot B \cdot H) = (7 \cdot 7 \cdot 7)m$. A scale factor $\alpha = 7$ is applied, in order to meet the geometry of the available testing facility, with the dimensions of $(L_s \cdot B_s \cdot H_s) = (1 \cdot 1 \cdot 1)m$.

Appendix I describes an in depth study of the scaling of small-scale experiments, all the downscaled parameters are derived according to the scaling rules. Appendix I, delivers funded decision on the choice of the scaling indicator, the scaling effects are treated and the differences between the model and prototype are in more depth described. A summary according to the Froude scaling is given for the relevant parameters used in the experiments. The scaling factors are expressed for in the length scale.

Sand in the experiments

The particle size distribution of the sand in the Nord Sea is between the particle diameters $250\mu m - 400\mu m$. For the simplification the average diameter of $325\mu m$ is scaled with the scaling factor for the particle diameter leading to $D_{50} = \frac{325}{\sqrt{N_L}} \approx 130\ \mu m$. The particle size distribution of the sand is determined according to the prescription of MTI and is given in the appendix.

Symmetry plane

The symmetry plane in the small-scale experiments reduces two identical hopper sections to one hopper section. The hopper sections has the same geometry and amount of sand.

6.2.1 Experimental Layout

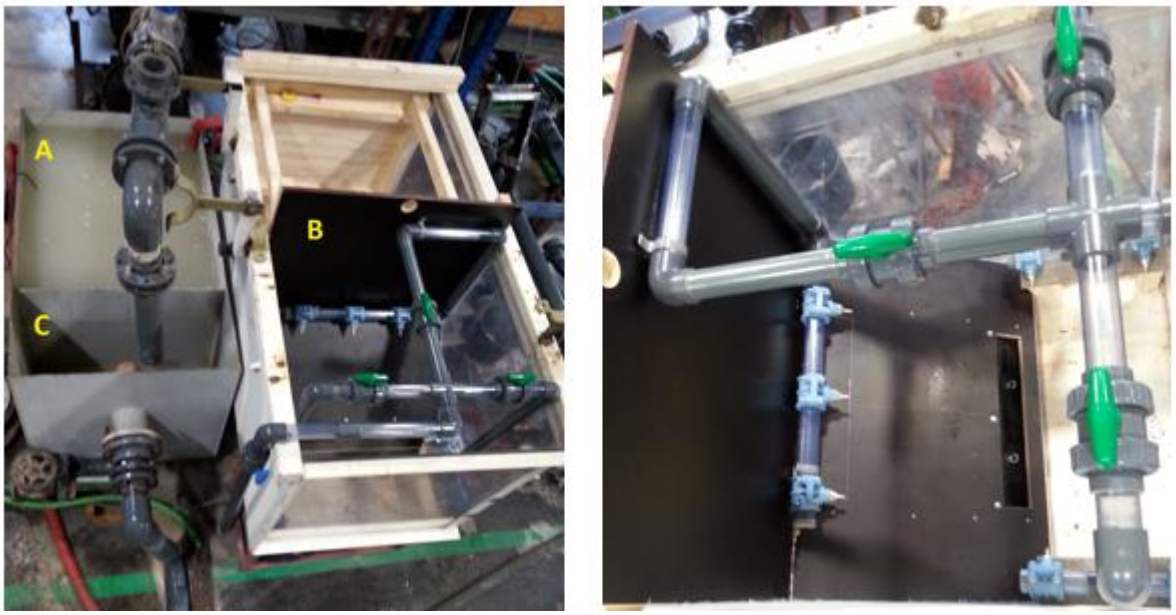

FIGURE 6.1 OVERVIEW OF THE TESTING FACILITY, A=WATER RESERVOIR, B=SCALED HOPPED SECTION, C=SAND STORAGE CONTAINER.

Figure 6.1**,** gives an overview of the testing facility. The picture left shows the water reservoir A, the soil storage container C and the scaled hopper section B. The picture right gives a closer view into the scaled hopper section B.

The part where the hopper is positioned gives two viewing perspectives (front view and side view of the hupper) into the hopper; these two planes of the testing container are transparent. The unloading process is recorded at both viewing sections.

6.2.2 Experimental Setup

Components of the testing facility

The schematic overview in figure 6.3 describes the process flows and experimental components of the experimental setup. For the execution of the experiments, the following list of materials is required:

A. Water reservoir
B. Storage reservoir
C. Big Bag
D. Jet pump (50mm Rotary pump)
E. Centrifugal pump (100mm Linatex pump)

F. Hopper section (Testing container)
G. Jetting system
H. Sand

The material list is in more detail described below:

A. The water reservoir, unloading storage tank, the use of the big bag are similar as described in the first series experiments, chapter 7. The only difference in the small-scale tests is the water outflow from storage tank (C).

B. See A.

C. See A.

D. A 50mm SEAR pump, transports the jet water from the water reservoir (A) into the hopper (B), the flowrate is varied with a variable-frequency drive.

E. A 100mm Centrifugal pump, transport the mixture from the hopper (B) to the sand storage container compartment (C) into the big bag.

F. The hopper is the scaled jetting section of the prototype. The hopper section consist of the jetting system and the kippekooi. The kippekooi consists of the unloading door, the emptying channel and the sea inlet, similar to the prototype. The unloading door opens manually by a rope connected to a pulley above the testing facility. Water flows from the sea inlet towards the unloading point and the mixture flows from the unloading point from the hopper to the big bag in storage tank C.

G. The jetting system consists of a 50mm diameter transparent PVC pipes, nozzles and closing valves. The nozzle diameter and orientation are scaled according to the configuration of the prototype.

H. The sand in the small-scale experiments is Sibelco AF100 sand with an particle diameter of $D_{50} = 130\ \mu m$, the same sand as used in the first series experiments

Measuring devices

The measurement devices in the testing facility consist of:

- pressure sensor
- two flow rate sensors
- 3 conductivity probes

Measurements

- Density in the sandbed
- Density in the unloading channel
- Flowrate in the unloading channel
- Jet flowrate

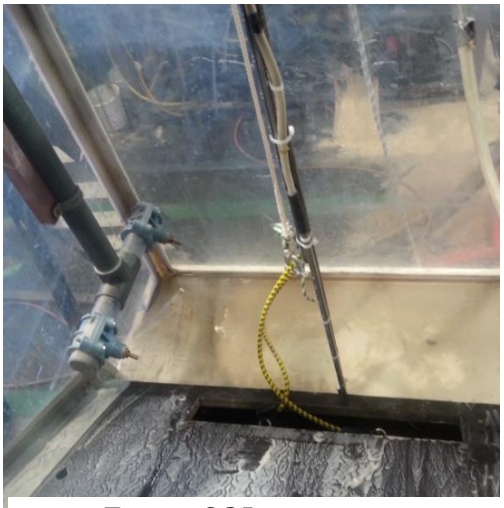

FIGURE 6.2 IN THE MIDDLE THE LOCATION OF THE CONDUCTIVITY PROBES, IN YELLOW THE UNLOADING DOOR ROPE

- Jet pressure

The locations of the sensors are shown in figure 6.3. The pressure sensor measures the jet pressure. The jet flow sensor measures the total flow rate for all the nozzles. Two conductivity probes are installed over the vertical height of the hopper, delivering density measurements up to 0.8m above the bottom of the hopper. The conductivity probe K and L are installed in the midsection of the unloading channel, with the measuring points directed towards the kippekooi, see appendix VII for the numbering of the measuring pints of the probes. Conductivity probe N is installed in the unloading pipe, the measuring points are directed in the opposite direction of the unloading flow and this delivers accurate mixture concentration (Nasr el Din et al, 1993).

FIGURE 6.3 SCHEMATICALLY OVERVIEW OF THE PROCESS FLOWS AND THE COMPONENTS OF THE TEST SETUP GIVEN IN FIGURE 6.1.

6.3 Test Execution

Procedure per experiment

- Determine the settings of the experiments according to the experimental matrix.
- Cleaning the unloading pipe and centrifugal pump by inserting water via the sea inlet, for the prevention of sanding of the pipes.
- Closing the hopper valve (in front of the pump).
- Opening the unloading door and filling the aquarium with water inserted via the sea inlet. Filling the aquarium up to the jets of the kippekooi.
- Closing the sea inlet and the unloading door in the hopper.

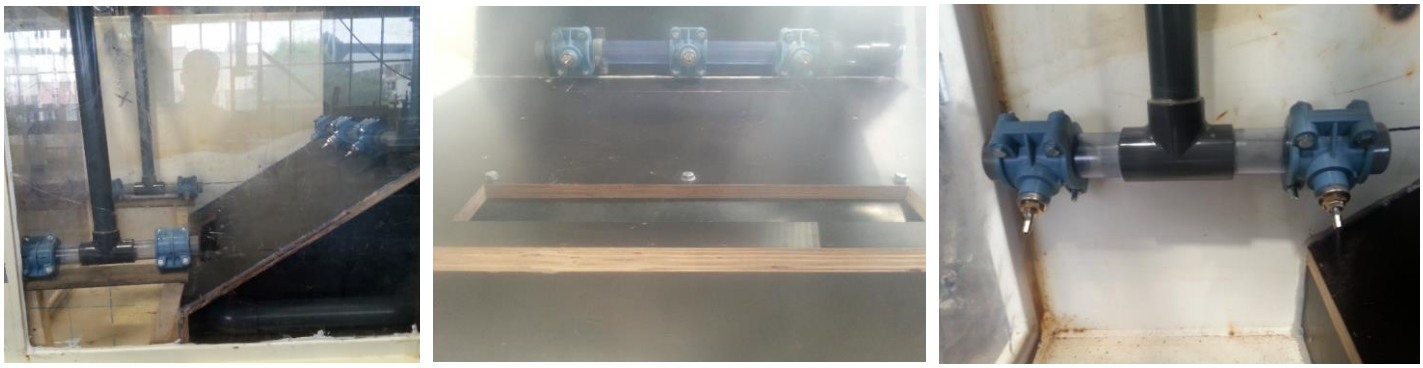

FIGURE 6.4 LEFT, SIDE VIEW OF THE HOPPER SECTION. MIDDLE, KIPPEKOOI NOZZLES AND IN DIRECTION OF UNLOADING DOOR, RIGHT NOZZLES AT THE SIDE WALLS

- Hoisting the sand loaded big bag from tank C above the hopper, emptying the big bag in the hopper (by ‘’controlled’’ cutting the bottom of the big bag).
- (Additional) Filling the sand up to **710mm** above the bottom.
- Adding water on the surface up to 850mm above the bottom.
- Giving the sand bed approximate 20 minutes settling time.

Starting and ending experiments

- Positioning a new big bag in tank C.
- Positioning and preparing the camera’s for recording.
- Indicating the experiment number on the viewing section.
- Starting the jetting pump, opening the jet valves.
- Tracking the pre-jetting times with a stopwatch.
- Opening the hopper valve (in front of the centrifugal pump)
- Opening the sea inlet for a water flow in the emptying channel.
- Starting the centrifugal pump.
- Opening the unloading door in the hopper.
- Closing the sea inlet.
- Viewing the unloading process.
- Drawing the shape of the fluidization trench on the viewing section.
- Shutting the centrifugal pump.
- Shutting the jetting pump.
- Stopping the video recordings
- Making notes of the experiments.

6.3.1 Variables

The standard jetting and unloading variables of the prototype are tested and used as reference material for the comparison between the existing jetting parameters and the tested parameters. The jetting parameters, pre-jetting times and initial water conditions in the hopper are tested and compared for the fluidization velocity, the unloading velocity and the amount of residual load. The following parameters are tested in the experiments:

- jet flow
- jet pressure,
- jet hydraulic power
- Pre-jetting times
- Unloading flowrate
- Initial conditions prior to fluidization.
- Adapted nozzle configurations

Jet pressure

The pressure levels of 3bar, 4bar and 8bar are tested. In this way, the influence of higher and lower pressure is studied on the fluidization process, the created mixture densities and the influence of it on the unloading process.

Jet flow rate

Different flowrates give understanding of the influence of the flow rate on the fluidization velocity, the created mixture density and the unloading velocity. The flow rate at constant pressure is varied by inserting different nozzle diameters.

Jet hydraulic power

Tests with higher and lower hydraulic power values are conducted in order to see the collaboration of the jets on the fluidization process.

Pre-jetting times

The pre-jetting times are varied and the influence of the pre-jetting times on the density in the bed, the fluidization velocity and the unloading velocity is studied.

Unloading flowrate

Two different unloading flow rates are studied for the understanding of the unloading velocity on the unloading time and the amount of residual load.

Initial conditions prior to fluidization.

Different companies use different methods for the water level conditions, for the unloading process in the hopper. The methods are tested and the influence of the water conditions on the unloading velocity is studied.

Adapted nozzle configurations

The adapted nozzle configuration consists of an extra nozzle located at the kippekooi having the same specifications and orientation as the other 3 existing nozzles. The distance between the nozzles is reduced in order to reduce the amount of residual load at both wall sides of the kippekooi.. The first experiments showed that fluidization of the soil by jets, mainly occurs above the nozzle, therefore the nozzles at the wall are lowered to the bottom.

Difference between model and prototype

The model consists of one hopper section; the prototype consists of 10 hopper sections. In the prototype the fluidization system fluidizes two emptying sections simultaneously, this means jetting in 4 hopper sections. In the prototype more water is inserted in the hopper, the upper surface of the sand bed is better fluidized and the hopper contains more water, which reduces the chance on sanding of the pipeline due to shortage of water. The other difference is the amount of sand which is unloaded, in the prototype the sand from one section flows and breaches to the other unloading section. However, these differences are small quantity differences, the fluidization and unloading trends, remains more or less the same for model and prototype.

6.3.2 Experimental Matrix

Experiments 1 to experiment 24 contain similar jetting positions and orientations as in the prototype. The jet pressure, jet flowrate and jet diameter are varied. Experiments 25 to 33 contain an adjusted jetting system.

In the column of the water level (Hw) the symbols 850, dry and constant refer to different water level conditions. 850 represents 1m water level on the surface of the bed, dry represents, dry sand conditions prior to unloading and cons represents a constant water level during the unloading process. In the dry conditions, the cargo unloading occurs only with the inserted jet water. The constant water level contains extra water inflow of approximate $Q = 6\frac{L}{s}$, inserted at the top of the hopper. These different water level conditions are tested during the different jetting specifications in the experiments. Based on the fluidization and unloading trends observed during the experiments the choice for the pre-jetting times and the unloading method for the water level conditions is adjusted.

TABLE 6-1 EXPERIMENTAL MATRIX

The marked values are the variations per experiment

Nr	Hw [mm]	Hs [mm]	prej [s]	D [mm]	p [bar]	Qj [L/s]	P [W]	Qj/Qp	Qunl	freq. JP [Hz]

The denotations in the upper row, from left to the right represents: the experiment number, the average sand production, the average unloading density**,** the residual load, water level, sand level, the pre-jetting time, the nozzle diameter, nozzle pressure, nozzle flow rate, nozzle hydraulic power, ratio between the jet pump flowrate and unloading flow rate, frequency of the jet pump.

Testing groups

Group (1-8)

The colors in the matrix indicate different testing groups, the green color in the matrix (1 – 8), represents the experiments which contain similar jetting specifications as the prototype. In this testing group, the influence of the pre-jetting times and the water condition in the hopper is varied. The first experiment has a similar pre-jetting time as the prototype and therefore is the most

representative to the conditions of the prototype.

Group (9-10)
The pink group, tests the influence of the jet pressure and therefore the hydraulic power increase of the jets on the fluidization. The jet pressure represents a pressure of approximate 8 bar in the prototype. The significant pressure increase delivers also a slight flow increase.

Group (11-13)
The red group, tests the influence of a lower unloading flow rate on the unloading velocity.

Group (14-15)
The white group, tests the influence of a lower jet flow at constant pressure.

Group (16-18)
The grey group, tests the influence of increasing flow rate and therefore at increasing hydraulic power at approximate constant pressure. This is the opposite of experiments 9 and 10 at approximate the same hydraulic power.

Group (19 and 20'
The golden group, tests the influence of decreasing hydraulic power, by decreasing the jet pressure.

Group (21-23)
The yellow group, tests the influence of different ratios of jet pump flowrate and unloading flowrate.

Group (24-31)
The bleu group, tests the influence the new jetting configuration, with an extra jet on the kippekooi and positioning the jets as deep as possible in the hopper, under a small downward angle of approximate 7 degrees directed towards the hopper bottom.

Group (24-27)
Experiments (24-27) tests, the combinations of parameters, which delivered the most optimized conditions for the unloading velocity during the first 23 experiments.

6.4 Interpretation of the results.

The influence of the jetting parameters on the unloading times is studied, the scope is of the experiment is to achieve fast unloading times, by delivering high unloading productions in the unloading channel. The results of the experiments will deliver recommendations for the fluidization system.

6.4.1 General proceedings for the experiments

After the preparation steps for the experiment and prior to unloading, the soil is pre-jetted. In the prototype, the pre-jetting times for each hopper section is between 3 and 5 minutes. The pre-jetting times in the hopper are based on experience in the vessels and have no further theoretical background. The pre-jetting time of the reference experiment is 90 seconds, translating to the prototype this approximates 4 minutes of pre-jetting. During the pre-jetting period, the hopper cargo becomes partly fluidized and the soil volume starts expanding, piping occurs first close to the jets of the kippekooi and then at the sides of the hopper. The erosion trenches of the jet walls close to the transparent wall are traceable; this advantage shows the fluidization process during the pre-jetting times and during the unloading process. The hopper unloading process is clearly visible; this makes it possible to anticipate on a potential sanding of the unloading channel.

6.4.2 Phenomenological description of the jetting and unloading process

The jets are slowly trenching in the direction of the jets; the jets are oriented under an angle of 33 degrees. The jets are trenching in the sand towards the hopper bottom; the erosion trench slowly deflects in the upward direction as the distance from the nozzle increases.

In the first few seconds of jetting, fluidization occurs around the location of the jets. The inserted jet water forms a mushroom shaped balloon in the bed, causing the upper surface of the bed slightly increasing, piping occurs and the water moves in the vertical direction and starts fluidizing the area above the nozzle. After the piping process, the jets keeps trenching at a faster rate deeper in the hopper, while the fluidized area above the nozzle increases rapidly. The fluidization area of the water jets becomes in the shape of an arrow, small in the eroding top and increasing in width at the tail, see figure 6.5. The fluidized area at the upper layers of the soil increases faster than the trenching velocity of the jets. At a certain moment, the fluidized area above the nozzles is wide enough to fluidize the top half of the total bed height. The lower midsection of the hopper cargo, the volume at the bottom doors fluidizes as last, this happens during the unloading process.

After the unloading doors are opened the sand bed decreases rapidly in height until a certain height at which the unloading decreases significantly. A certain amount of residual load remains on the top of the kippekooi, the sidewalls of the kippekooi and at the bottoms doors, see figure 6.6. The spaces under the nozzles remain un-fluidized during the complete fluidization cycle; an un-affected triangle of sand remains under the nozzles even after the soil is unloaded.

A few seconds before the unloading door is opened, the sea inlet is opened to trigger the unloading and prevent sanding of the unloading pipe. When the unloading door opens, the sand bed starts moving downwards. When the sand surface reaches the kippekooi level, in most experiments residual loads remains at the top of the nozzles, at the sidewalls of the hopper and especially above the bottom door. The amount of residual load is dependent of the pre-jetting time, jet pressure, jet flowrate and the dry-, constant and 1m water level conditions.

[redacted]

The unloading time and concentration development in the unloading channel are the most important parameters for the validation of the analysis.

In all experiments, the concentration in the unloading channel increases at the start of the unloading process, this remains for a certain period (in the order of seconds) and then the concentration slightly decreases and converges to lower densities, see figures 6.12 – 6.14. When the jets were not significantly fluidizing sand or the jets were not influencing the residual load the jetting pump and unloading pump were switched off.

[redacted]

6.5 Mixture density development in the sand bed.

This paragraph describes the density development in the bed for 3 phases: prior to fluidization, during the fluidization and during the unloading process. Probe K measures the density of the bed from the bottom of the bed up to 0.4m above the bed; probe L measures the density between 0.4m and 0.8m above the bed.

Density prior to fluidization

The density prior to the fluidization process for all the experiments is approximately between $\rho = 1900\frac{kg}{m^3}$ and $\rho = 2000\frac{kg}{m^3}$. In the first series experiments, the difference between compacted and uncompacted experiments is described. The sand in these experiments is not additionally compacted. The sand in the big bag is unloaded in the hopper; this unloading has influence on the behavior of the bed. In most experiments, the sand is unloaded in the left corner of the hopper. During the unloading process, it was clearly visible that parts of the sand in the left corner of the hopper were more compacted than the sand in the other parts of the hopper. This might be off importance for the prototype TSHD, but is out of the scope of this research.

Due to the uncontrolled unloading of the sand in the hopper, it is assumed that the sand bed condition prior to the fluidization process is un-homogenous and differs for each experiment. This process is not controllable in the experiments; however, by compacting the sand bed this problem is reduced, the compaction forces the sand bed to a more homogenous bed.

6.5.1 Density development for probe L

The difference between the experiments for the density development over probe L, is mainly dependent on the variation of the pre-jetting times and the total flow rate of the jets. Probe L is positioned in the upper layer of the soil and describes almost similar developments for all the experiments.

Pre-jetting period

Prior to the jetting process, the density in the bed $\rho \approx 1950\frac{kg}{m^3}$. After approximate 10 to 20 seconds of pre-jetting, the density of the soil slightly decreases to approximately $\rho = 1900\frac{kg}{m^3}$. After a certain period, depending on the pre-jetting time and the flowrate, the density of the mixture decreases from $\rho \approx 1900\frac{kg}{m^3}$ to $\rho \approx 1800\frac{kg}{m^3}$.

Unloading period

During the unloading process, the density over the height of probe L for pre-jetting times higher than approximate 60 seconds reaches a period where the density decreases between $1600\frac{kg}{m^3} < \rho < 1800$ see figure 6.7. Delivering the lowest density at the surface of the bed (L_7) and the highest density in the lowest measuring point of probe L (L_{10}). For pre-jetting times smaller than approximate 60 seconds, the density of the upper layers decrease directly from $\rho = 1900\frac{kg}{m^3}$ to

$\rho \approx 1000 \frac{kg}{m^3}$, see figure 7.8, for experiment 15 in table 7-2.

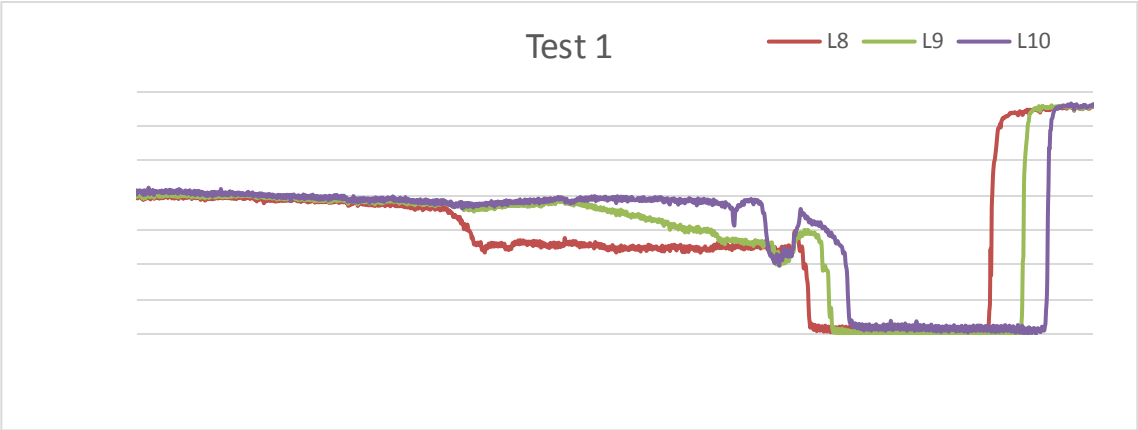

FIGURE 6.7 DENSITY DEVELOPMENT FOR THE UPPER LAYER (120MM FROM THE SURFACE OF THE BED), TEST 1 OF TABLE 7-2. THE PRE-JETTING TIME STARTS AT APPROXIMATE 170S. THE UNLOADING STARTS AT APPROXIMATE 270S.

Figure 6.7, shows the longer pre-jetting time gives more time to fluidize the upper layer of the soil, the parallel lines indicates a constant unloading velocity. The line starts slightly decreasing from t=190s. The density at the surface of the bed L_8, decreases first and during the pre-jetting time converges to $\rho = 1600 \frac{kg}{m^3}$. At the end of the pre-jetting time the density of L_9 (40mm from the surface) decreases also towards $\rho = 1600 \frac{kg}{m3}$. During the unloading process the density decreases to $\rho = 1500 \frac{kg}{m^3}$. The parallel lines between t=280s and 290is the vertical downward velocity of the bed, which decreases to the density of water. At t=310s the measuring point is in air, meaning the mixture and water level decreased to a lower level in the bed. Figure 6.8, shows the density development in the bed for a significant smaller flow rate.

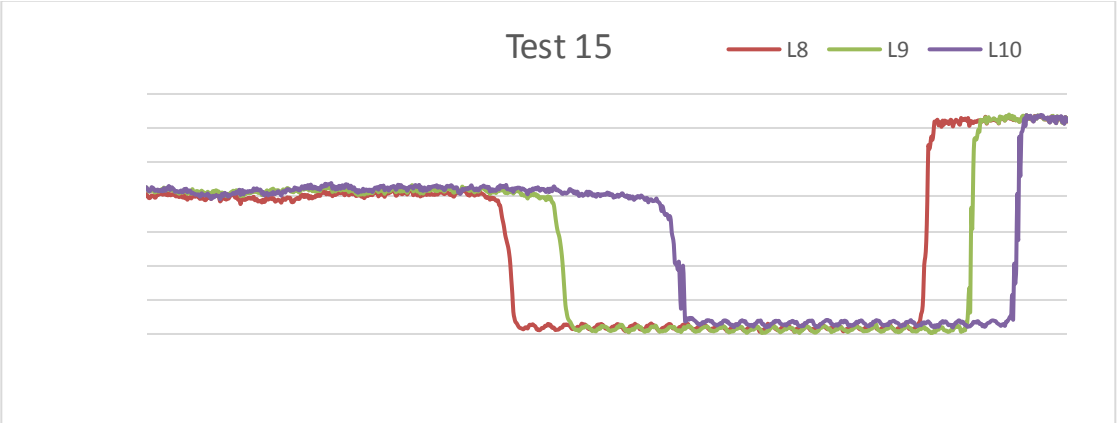

FIGURE 6.8 THE DENSITY DEVELOPMENT FOR THE UPPER LAYER (120MM FROM THE SURFACE OF THE BED), TEST 15 OF TABLE 7-2. THE PRE-JETTING TIME STARTS AT APPROXIMATE 95S. THE UNLOADING STARTS AT APPROXIMATE 120S, BETWEEN 165 AND 175 THE PROBE MEASURES AIR, MEANING THE MIXTURE AND WATER LEVEL DECREASED UNDER THE LEVEL OF THE PROBES, THE PARALLEL LINES INDICATES A CONSTANT UNLOADING VELOCITY.

6.5.2 Density development for probe K

The difference between the experiments for the density development over probe K, is mainly dependent on the variation of the pre-jetting times and the total flow rate of the jets. Probe K is positioned in the deepest layer of the soil.

Pre-jetting period

Prior to the jetting process, the density in the bed is approximately $\rho = 1950\ \frac{kg}{m^3}$. During the pre-jetting period, the jets are not able to erode and reach the area close to probe K, therefore there is no direct density difference measured during the pre-jetting period. For higher flow rates and longer pre-jetting times larger than 60 seconds, the density at locations K_1, K_2 and K_3 decreases between $1800\frac{kg}{m^3} < \rho < 1900\ \frac{kg}{m^3}$. See figures 6.9 – 6.11

Unloading period

During the unloading process, the experiments show similar development of density trajectories. The soil levels up to K_3 decreases quickly, meaning that the sand is vastly unloaded. For the locations, $K_4 - K_7$ the density in the bed decreases more linearly from $\rho \approx 1800\ \frac{kg}{m^3}$ to $\rho \approx 1200\ \frac{kg}{m^3}$, in all cases and under all conditions the overall density of the mixture increases over depth. In general, when the density of the mixture reaches point K_1 (0.4m above the bed) the mixture density reaches $\rho \approx 1100\frac{kg}{m^3}$, at the time the mixture reaches the location of K_7 the density becomes $\rho \approx 1400\frac{kg}{m^3}$. When the mixture decrease closer to the unloading point, a lower and constant density is reached. The experiments with higher power translated into more flow rate (experiments 16-18), the density for the locations $K_1 - K_7$ do not give a linear density pattern over the height, but gives a constant value of $\rho \approx 1200\frac{kg}{m^3}$ for $K_1 - K_7$. This confirms that too high flow rates leads to low unloading densities in the hopper.

Pre-jetting times larger than 60 seconds influences the density at locations K_1 and K_2 (middle of the hopper) approximate to $1800\frac{kg}{m^3} < \rho < 1900\ \frac{kg}{m^3}$.

It seems that larger pre-jetting times and higher flow rates lead to the same density trends in the bed.

Density development of the first experiment

The density development for probe K over the vertical height in the bed is elaborated. For a clear overview of the density developments, the 10 measuring points of probe K are divided in 3 figures.

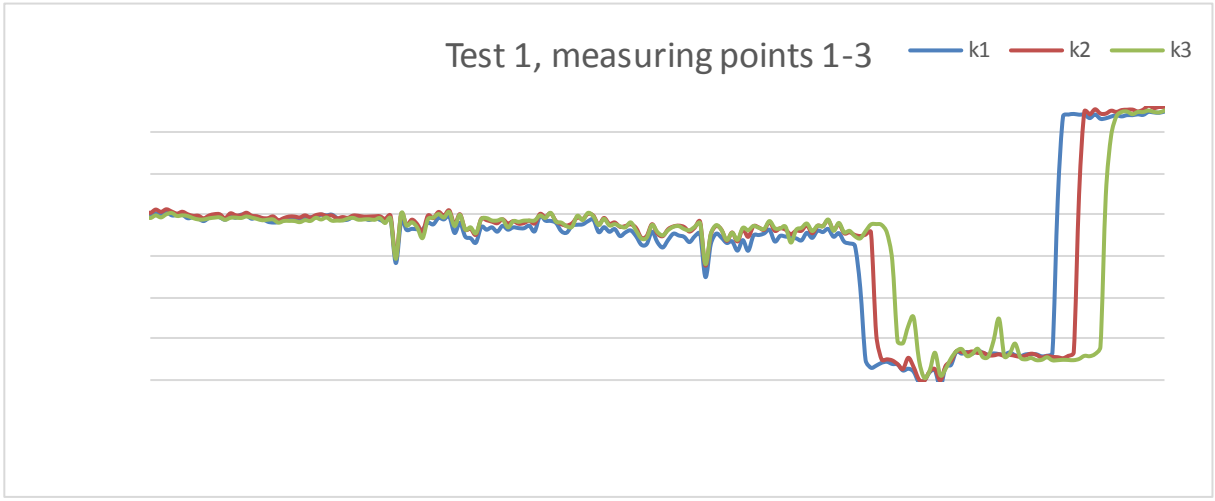

FIGURE 6.9 THE DENSITY DEVELOPMENT FOR THE 280 – 400MM ABOVE THE BOTTOM, TEST 1 OF TABLE 7-2. THE PRE-JETTING TIME STARTS AT APPROXIMATE 170S. THE UNLOADING STARTS AT APPROXIMATE 270S.

The pre-jetting period slightly decreases the density of the 120mm top layer in the bed, after approximate 30s pre-jetting the bed at this level starts moving (increasing in pore space), the parallel lines indicates a constant unloading velocity.

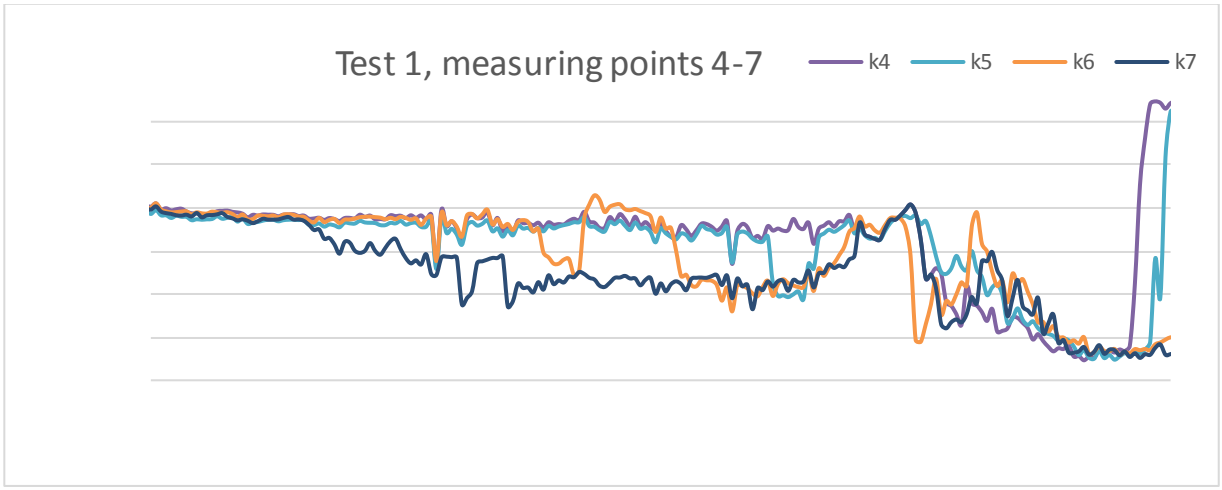

FIGURE 6.10 THE DENSITY DEVELOPMENT FOR 240 – 120MM ABOVE THE BOTTOM, TEST 1 OF TABLE 7-2. THE PRE-JETTING TIME STARTS AT APPROXIMATE 170S. THE UNLOADING STARTS AT APPROXIMATE 270S.

Figure 6.10 shows that longer pre-jetting time gives more time to fluidize the mid layer in the bed, the jets are fluidizing under a downward angle this layer is therefore for a longer period under the influence of the upward flow direction and therefore better fluidized, the lines indicate a linear decreasing unloading velocity at this layer in the bed.

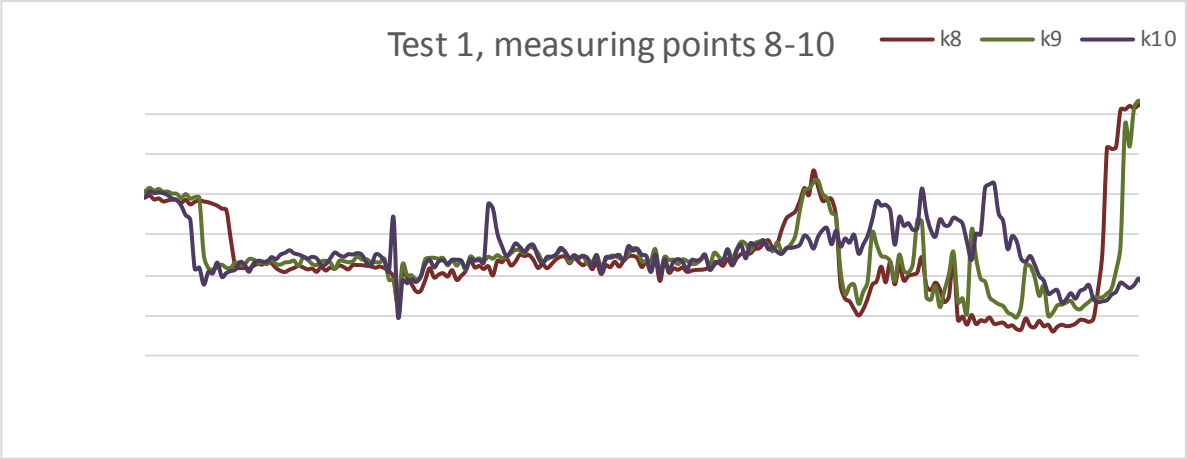

FIGURE 6.11 THE DENSITY DEVELOPMENT FOR 0 - 120MM ABOVE THE BOTTOM, TEST 1 OF TABLE 7-2. THE UNLOADING STARTS AT APPROXIMATE 270S.

Figure 6.11, shows that the soil is fluidized even prior to the pre-jetting period, however, this decrease at the lowest layer in the bed is due to leakage flowing under the kippekooi. Water from the empty reservoir, flows at a small flow rate under the kippekooi towards the hopper side. The bottom of the kippekooi and testing container does not seal for 100 percent.

6.6 Elaboration of the experiments

This paragraph analyses the influence of the jetting parameters on the combination of the jetting and the unloading process. The results for each group are described individually whereas at the end of the paragraph an overall conclusion of the results of the experiments is given.

TABLE 6-2 EXPERIMENTAL MATRIX INCLUDING RESULTS.
THE MATRIX OF TABLE 6-1 IS SUPPLIED WITH THE EXPERIMENTAL RESULTS, GIVEN IN THE GREY FIELD.

Nr	t [s]	prod. [kg/s]	ρ [kg/m3]	Res. Load [kg]	Hw [mm]	Hs [mm]	prej [s]	D [mm]	p [bar]	Qj [L/s]	P [W]	Qj/Qp	Qunl	freq. JP [Hz]
					360	710	90	±,0	0,72	1,47	106,84	0,12	12	18
					ooms	710	110	±,0	0,72	1,47	106,84	0,12	12	18

Green group (1-8), similar jet Pressure and Flowrate variation of Pre-jetting time and unloading condition.

The jet specifications of the first experiment are the most representative for the prototype, the results of this experiments is compared and validated with other tests. The unloading time of the first experiment delivers $t = 102s$, converting this to the prototype gives an unloading time of $t = 4{,}5\ minutes$, the total unloading time for the hoppers is based on the size of the hoppers and is between 45 minutes and 75 minutes. The vessel is a relative small hopper having unloading times in the order of 45 minutes. Based on the model unloading time of 4.5 minutes for one hopper section, of the total 10 hopper sections delivers an unloading time close to the prototype.

The average density of the first experiment is in the order of $\rho = 1700\frac{kg}{m^3}$ with a production of $9.3\frac{kg}{s}$.

The second test consists of a pre-jetting time of 40 seconds (de Nijs), but notice that these tests are at different scale, this pre-jetting time delivered almost a sanded unloading pipe, extra water was inserted to avoid sanding of the unloading pipe. The extra water from the sea inlet reduces the average density of the mixture significantly, resulting to a significant higher unloading time. The unloading pipe has transparent walls, from which the unloading mixture is visible. Test number 3 is conducted for the dry sand conditions, this condition has no additional water in the hopper; therefore, the test contains the highest pre-jetting time. The pre-jetting time translated to the prototype gives 5 minutes, this not sufficient (see figure 6.12 at t=170 seconds) the unloading pipe is sanded. The hopper load in this experiment is also unloaded by using the sea inlet. A pre-jetting time of 110 seconds is also not sufficient for the unloading of the initial dry sand condition, here the unloading occurred also with additional use of the sea inlet. A pre-jetting time of 150 seconds was sufficient for the unloading of dry sand condition, in this experiment the sea inlet was not additional used for the enhancing of the unloading. The dry sand tests all ended with significant amount of residual load.

Tests 6 to 8, at constant water level condition in the hopper, give lower unloading times and higher unloading productions for lower pre-jetting times. In these tests, the amount of the residual loads was also reduced, compared to the experiments 1 to 5.

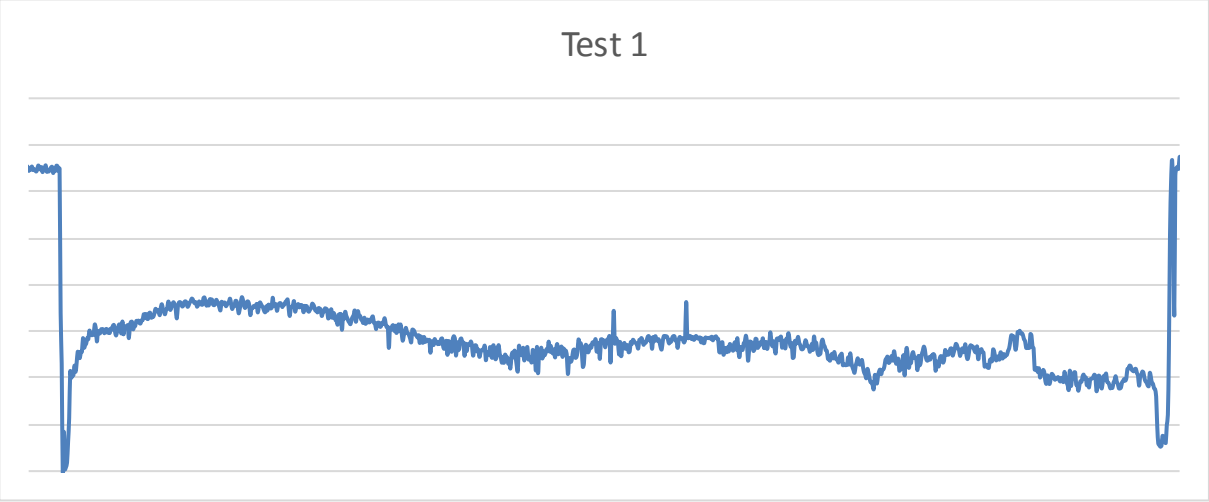

FIGURE 6.12 DENSITY DEVELOPMENT IN THE UNLOADING CHANNEL (EXPERIMENT 1 TABLE 6-2), FROM THE MOMENT THE SEA INLET IS USED (T=273S). THE DENSITY IN THE UNLOADING CHANNEL IS APPROXIMATELY CONSTANT DURING THE UNLOADING.

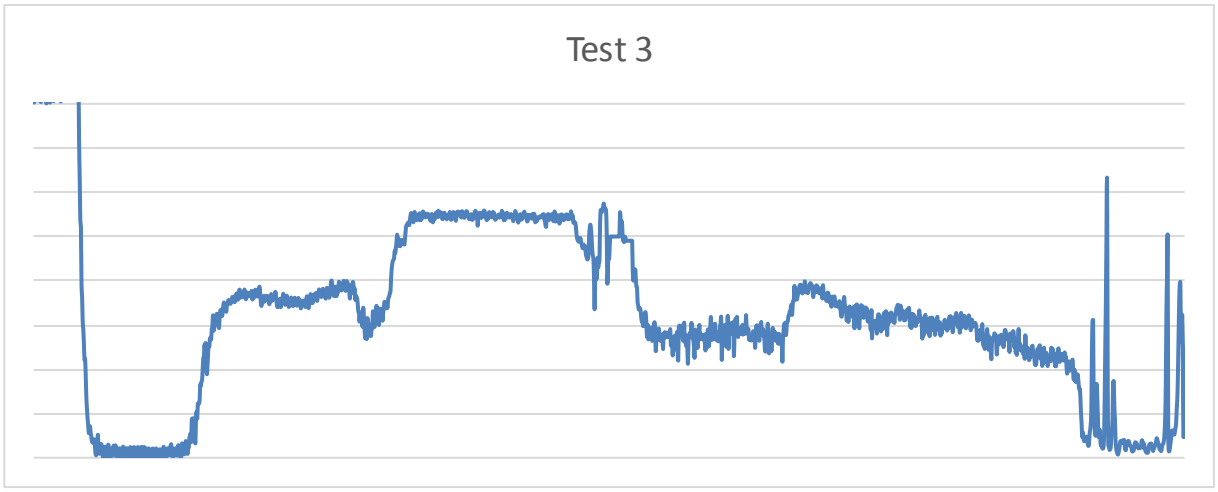

FIGURE 6.13 DENSITY DEVELOPMENT IN THE UNLOADING CHANNEL (EXPERIMENT 3 TABLE 6-2), FROM THE MOMENT THE SEA INLET IS USED (T=118S). FROM T=170 – 200S THE UNLOADING CHANNEL IS SANDED.

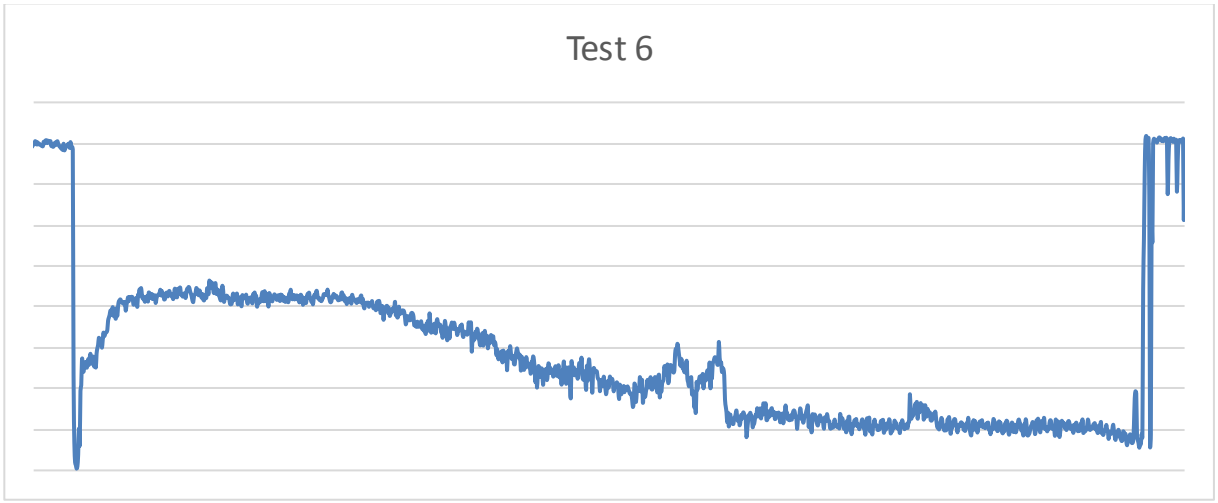

FIGURE 6.14 DENSITY DEVELOPMENT IN THE UNLOADING CHANNEL (EXPERIMENT 6 TABLE 6-2), FROM THE MOMENT THE SEA INLET IS USED (T=175S). THE FLUCTUATIONS AT T=250S REPRESENTS, LOOSED SAND LAYER SLIDING FROM THE KIPPEKOOI TO THE UNLOADING CHANNEL.

Group (9-10), higher Pressure rate

This group tests the influence of the jet pressure (p=8bar) (for the record, experiments 1-24, contain similar jet configuration) and therefore the influence of a higher hydraulic power. In experiment 9, at the beginning of unloading, the sea inlet is not used, therefore, the unloading time is low and the production is high, however the residual load was significant more than the previous experiments. This makes the unloading time less reliable compared to the other tests. Experiment 10 shows that increasing to higher pressures and lower pre-jetting times is sufficient to prevent sanding of the unloading channel (tests 3-5).

Group (11-13), Lower Unloading flowrate

For experiment 11, even for lower unloading velocity, a pre-jetting time of 60 seconds is not sufficient and therefore the sea inlet is additionally used for the prevention of a sanding of the unloading channel. The unloading time of experiment 13 is not reliable since the jet at the left wall of the hopper was sanded. Test 12 delivered a similar unloading time as test 1 here all the jet parameters are similar except the unloading flow rate, even for a lower unloading flow rate the unloading time is similar.

Group (14-15) Lowering Flowrate at constant Pressure

Test 14 and 15 are conducted for a significant lower jet flow rate, the jet pressure is remained constant, by decreasing the jet diameter. This delivered much higher unloading densities, however the higher micture densities did not lead to a faster unloading time. Contradictory, the unloading time here is higher. Test 15 is executed with a low flow rate, higher pre-jetting time and is unloaded with a constant water level at the top of the cargo, this combination delivered a similar unloading time as test 1 (even for a significant lower flow rate).

Group (16-18), Higher Flowrate (Increasing Hydraulic power)

Tests 16 to 18 are executed for higher hydraulic power, by increasing the jet flow rate. These tests are contrary to tests 9 and 10, where instead the pressure is increased, at similar hydraulic power level. In tests 16 to 18, the flow rate is high enough that even under dry sand conditions a pre-jetting time of 40seconds is sufficient. The dry sand experiments however delivered even in these conditions a significant higher amount of residual load. Experiment 18 does have a lower unloading time but the residual load is high.

Group (19 -20) Lowering pressure and increasing Flowrate (at approx. constant Power)

Using similar hydraulic power as the first group of experiments, but increasing the flow rate delivers interesting unloading times. Higher flow rates at relative lower hydraulic power delivers faster unloading times, but the residual load remains is higher. In the experiments, it is noticed that fully fluidization of the hopper cargo is not necessary for the unloading of the hopper cargo. If the flowrate and pressure level are sufficient to fluidize and keep up the unloading flow rate, no sanding will occure.

Group (21-23) Variation of jet flowrate and unloading flowrate ratio $\frac{Q_j}{Q_p}$

In tests $21-23$ the Qj/Qp ratio is varied under constant jet pressure, the flow rate is increased by increasing the jet diameter. The fastest unloading time is gained for the lowest flow rate (test 22) and the lowest amount of hydraulic power. The downside of this test is the greater amount of residual load, compared to tests 21 and 23. Test 23 delivered the least amount of residual load. This

experiment confirms that the hydraulic power is not significant for the fluidization process and the unloading process. Tests 22 also confirms, that the lower the flow rate, the higher the unloading densities and the faster the unloading time.

Group (24-27) Adapted Nozzle Configuration (pre-jetting variation)

In Tests $(24 - 27)$ the nozzle configuration is adapted and the new configuration is tested. In the previous experiments, the residual load accumulated at the wall sides on the kippekooi for almost all the experiments. An additional nozzle is attached on the kippekooi, reducing the distance between the nozzles and creating more jet overlapping area over the complete kippekooi. This nozzle has the same pressure and flow rate as the other nozzles on the kippekooi. This additional water jet on the kippekooi displaces all the sand on the kippekooi towards the unloading channel and the bottom of the hopper. The jets on the sidewall are lowered to the hopper bottom and the jet angle is reduced to 7 degrees, slightly bending towards the bottom doors.

The unloading times, for these experiments did not reduce **co**mpared to the reference experiment, but the amount of residual load significantly improved. The unloading times are comparable with the first experiments, but the residual load decreased to a negligible amount. In all the previous experiments, the wall sides of the kippekooi and the space on top of the bottom doors ended with residual load. This nozzle configuration reduces the pre-jetting time significantly. The first experiments required at least 90s of pre-jetting, in the new jet system configuration unloading times of even 20 seconds of pre-jetting.


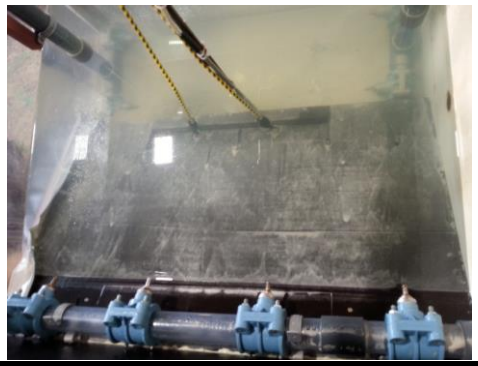


[redacted]

Group (28-31) Adapted Nozzle Configuration (most optimized unloading conditions)

In tests, $(28 - 31)$ the aim was to reduce the unloading times as much as possible; this is attempted by combining all the optimized findings of the previous experiments. Therefore, the experiments are executed for maintaining a constant water level in the hopper, reducing the jet flow rate to the smallest available jet diameter and reducing the pre-jetting times. Therefore delivering significant less water in the bed and increasing the mixture density. The differences in unloading times between tests (24-27) and tests (28-31) are very clear. Both groups contain similar

pre-jetting times, but experiments $(28-31)$ delivered improved unloading times. The pre-jetting time of 45 seconds delivered the best unloading time. Experiments show that a jetting period of 20s is sufficient for unloading, but more time is required for the unloading. On the other side, longer pre-jetting times are also not the most optimized solutions. Comparing test 30, 31with 28 gives that similar results can be achieved by using longer pre-jetting, but lower flow rates or by using high flow rates and reducing the pre-jetting times. The tests for 45 seconds for both jetting configurations delivers the most satisfying unloading times.

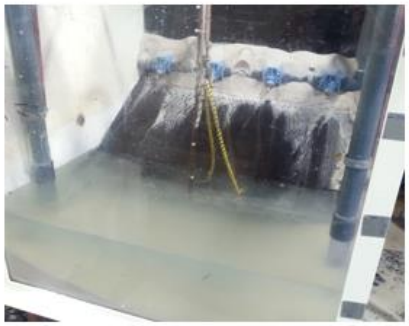

[redacted]

6.7 Analysis of experimental results

In this paragraph, first the influence of the overall trends for the flow rate, pre-jetting times, pressure and hydraulic power on the fluidization and unloading process is analyzed, then the results for the 850mm condition and the dry sand condition.

6.7.1 General trends

Experiments (1-24) which have been executed without extra measures are studied to understand and compare the general trends of the influence of the flow rate, pre-jetting times and the hydraulic power on the jet production and unloading times. The results for the lower unloading flow rate (11-13) and the tests where additional sea inlet are used, e.g. (2-4) are omitted in order to create comparable tests. Notice, the results are gained for different jetting conditions.

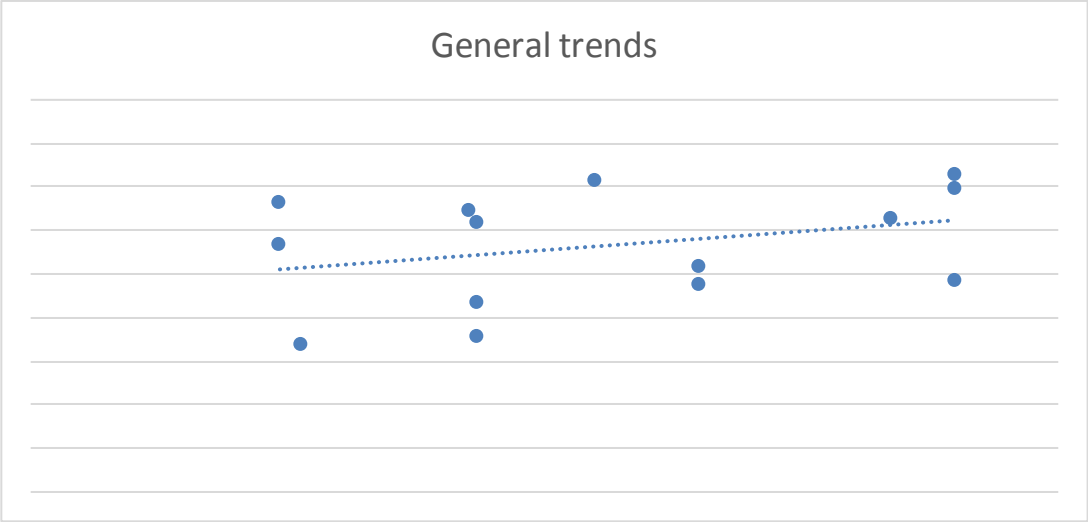

FIGURE 6.17 THE RELATION BETWEEN THE FLOWRATE AND THE UNLOADING TIME

The general results for the relation between jet flowrate and the unloading times, delivers an increasing trend, see figure 6.17. This means that increasing the jet flowrate increases the unloading time. By increasing the jet flowrate per unit of time more water is inserted into the bed, delivering lower mixture densities and therefore increasing the unloading times. The large fluctuations in figure 6.17 are due to the different unloading methods and pre-jetting times for each experiment.

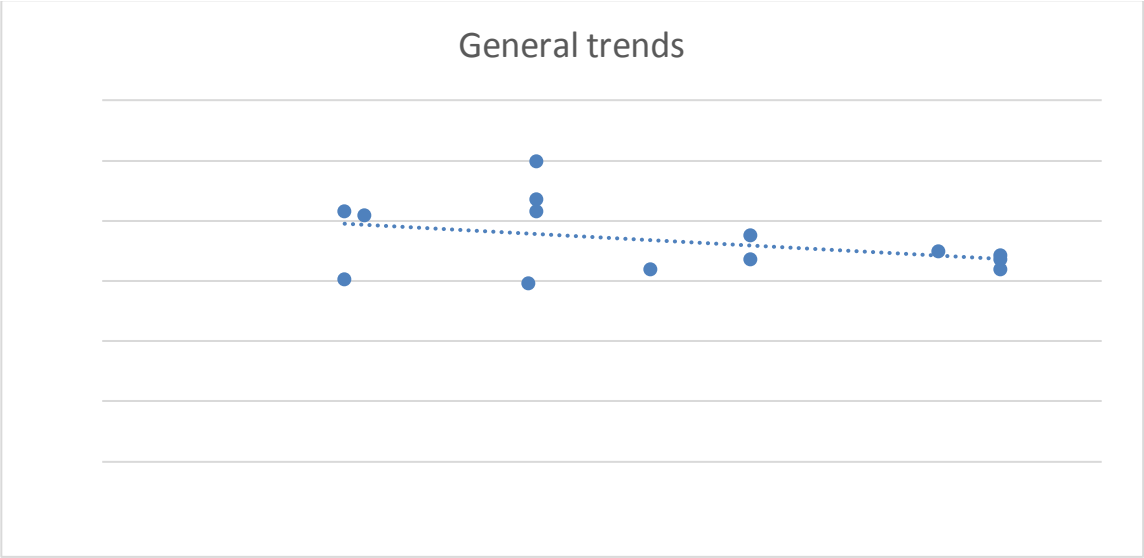

FIGURE 6.18 THE RELATION BETWEEN THE FLOWRATE AND THE UNLOADING PRODUCTION

The sand production is approximately linear correlated with the unloading time; this is not completeley linear, since the residual load in each experiment varies. Figure 6.18 shows that increasing jet flow rate has a negative impact on the unloading production. Increasing the jet flow rate decreases the unloading production.

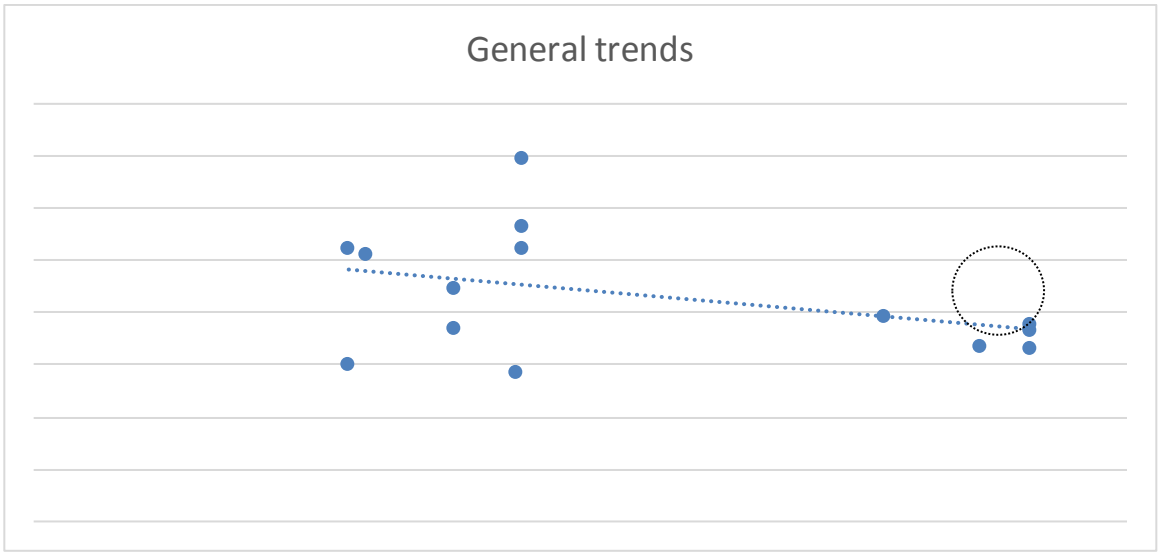

FIGURE 6.19 THE RELATION BETWEEN THE HYDRAULIC POWER AND THE UNLOADING PRODUCTION

According to figure 6.19: increasing the hydraulic power delivers a decreasing trend for the sand production; the marked measuring points contain the highest flow rates (see table 6-2), therefore decreasing the mixture density and leading the lower unloading productions.

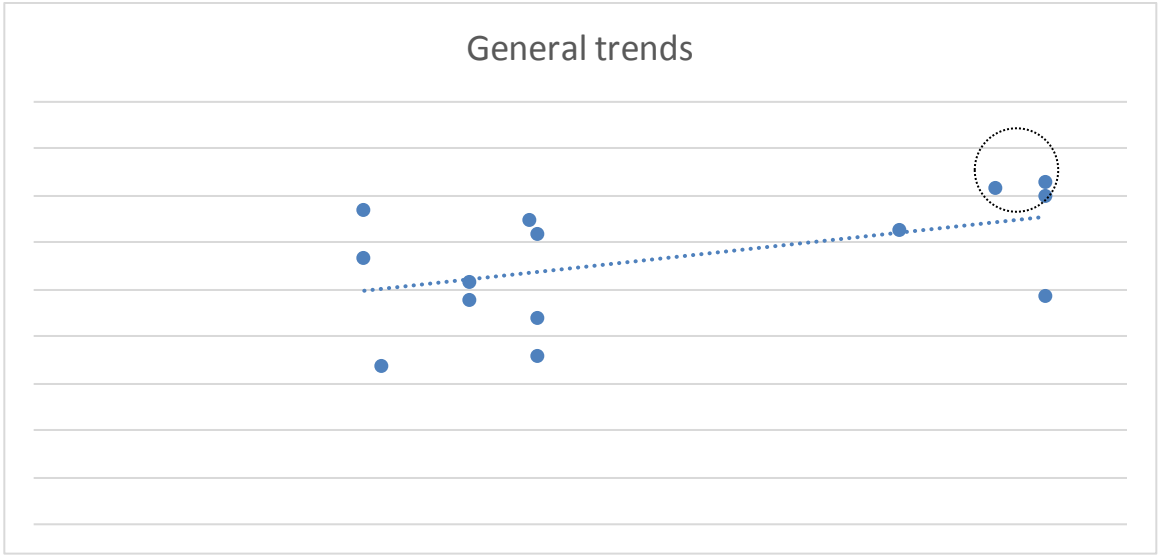

FIGURE 6.20 THE RELATION BETWEEN THE HYDRAULIC POWER AND THE UNLOADING TIME.

According to figure 6.20, increasing the hydraulic power increases the unloading time, the marked data points contains the highest hydraulic power (three upper right points) contain the highest flow rate. Higher flowrates decrease the mixture density and therefore increases the unloading time.

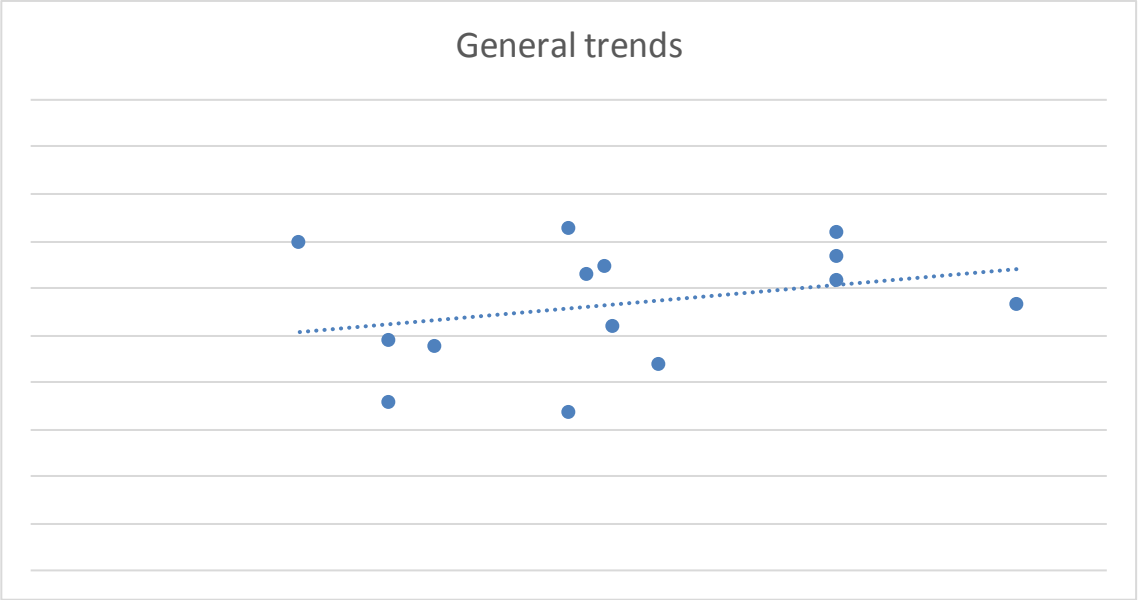

FIGURE 6.21 THE RELATION BETWEEN THE PRE-JETTING TIMES AND THE UNLOADING TIME

Figure 6.21, shows that increasing the pre-jetting times delivers higher unloading times and therefore, similar to figure 6.17, decreasing the unloading productions.

6.7.2 850mm condition

The 850mm condition represents the unloading process for the water level of approximate 1m water above the bed before the unloading process starts. Tests (1, 2, 9, 16, 19, 20, 21, 22) has been conducted for 850mm water level condition, the following results have been obtained.

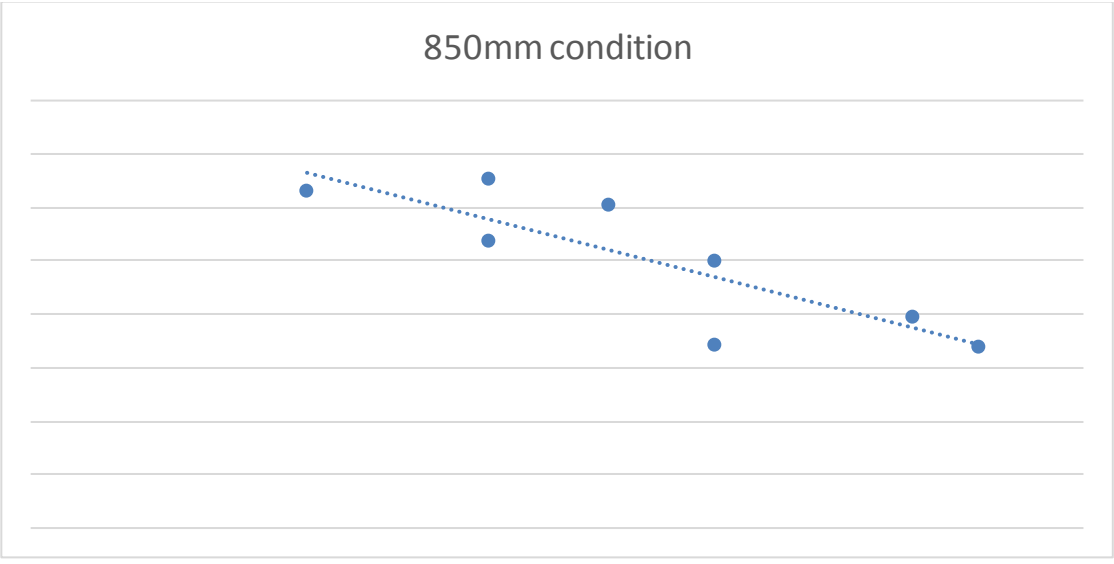

FIGURE 6.22 THE RELATION BETWEEN THE PRE-JETTING TIMES AND THE UNLOADING PRODUCTION

Figure 6.22, shows a clear relation between the jet flow rate and the unloading productions, increasing the jet flow rate delivers a linear decreasing trend for the unloading productions.

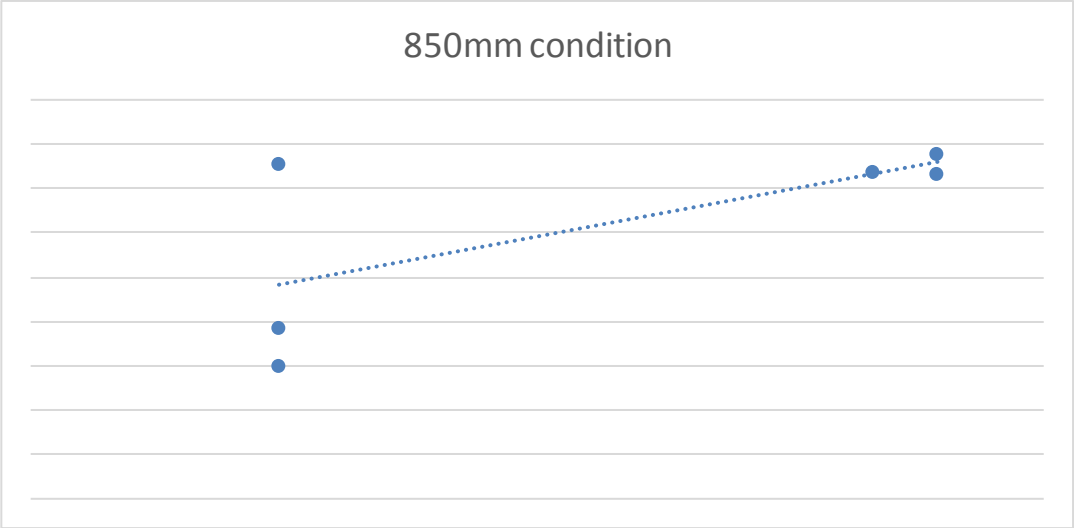

FIGURE 6.23 THE RELATION BETWEEN THE HYDRAULIC POWER AND THE UNLOADING PRODUCTION.

Figure 6.23, shows that increasing the hydraulic power increases the unloading productions, experiments with the highest hydraulic power contains the highest flow rates (see table 6-2), however in the 850mm condition significant lower pre-jetting times is used, reducing the possibility of lowering to, too low mixture densities.

6.7.3 Dry sand condition

The dry sand condition represents the unloading process for the unloading condition which does not have water on the top of the cargo. The soil contains high level of humidity, but the sand is dry enough to walk on the hopper cargo, however this is strongly discouraged. The high humidity level of the sand can form quicksand conditions at the top of the cargo. Tests (3, 4, 5, 10, 17, 18), are the unloading experiments for the dry unloading condition. The following results are obtained:

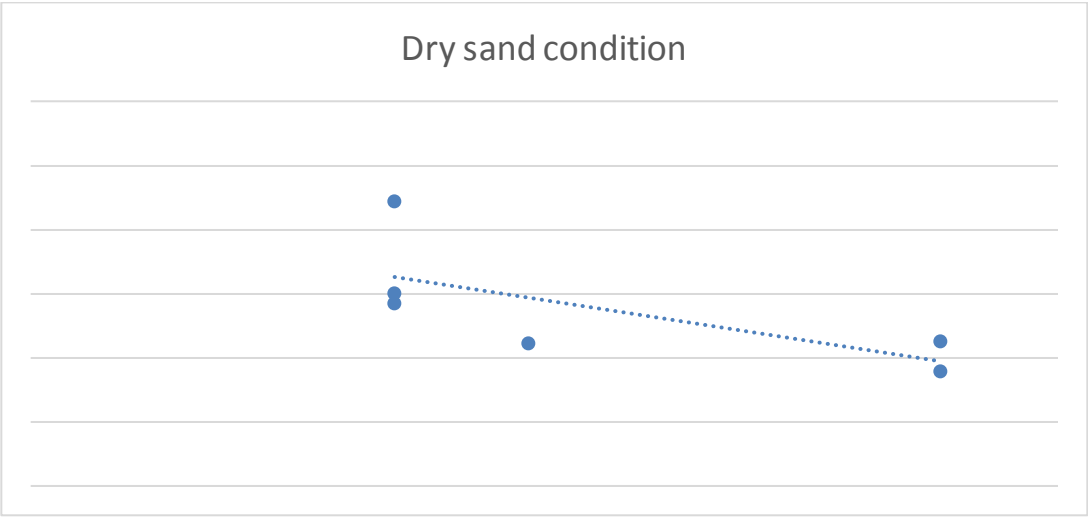

FIGURE 6.24 THE RELATION BETWEEN THE FLOW RATE AND THE UNLOADING TIME.

Figure 6.24, shows that increasing the flowrate for the dry sand condition decreases the unloading time, this is the opposite relation compared with the submerged soil conditions.

In the dry sand condition, the soil still contains a high level of moisture, but it takes more water to increase the pore level to reach the fluidized state. Before the fluidization process takes place, the water has to flow in the pores of the sand, then the pores as to expand to a certain porosity. Due to the expansion of the pores the superficial velocity increases, more water flows through the pores. This increase in superficial velocity and the bed expansion cause the particles to move and form a mixture.

For the dry sand conditions, missing the pore water, or at least a part of the pore water, creates the need for the filling of the pores with water. For increasing the desired fluidization volume of the bed, the bed requires more water, compared to the submerged conditions. This extra step in the fluidization process gives an extra delay for the fluidization process. Causing larger fluidization times.

In the dry sand, more steps are required for achieving the fluidized state; therefore, it requires more water and more time to fulfill the processes to reach fluidization (bed expansion).

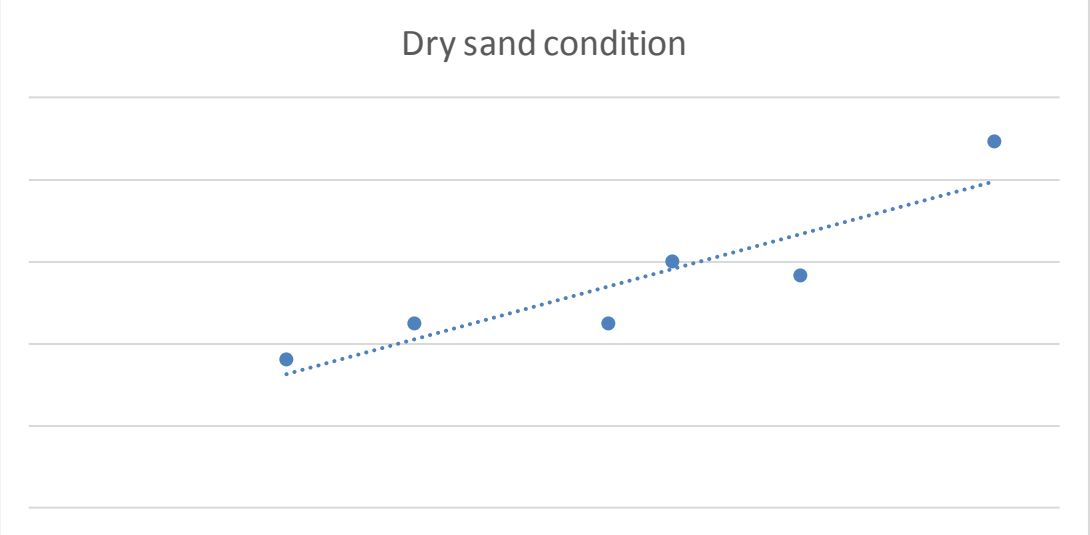

FIGURE 6.25 THE RELATION BETWEEN THE PRE-JETTING TIMES AND THE UNLOADING TIME.

Figure 6.25 and 6.26, shows that also for the dry sand condition increasing of the pre-jetting time leads to lower unloading productions and therefore higher unloading times.

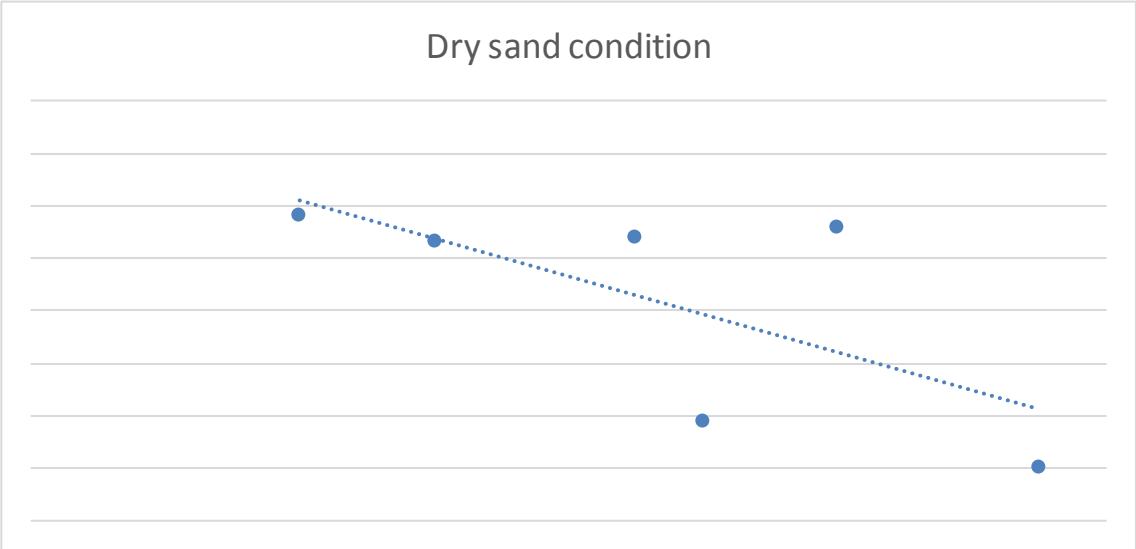

FIGURE 6.26 THE RELATION BETWEEN THE PRE-JETTING TIMES AND THE UNLOADING PRODUCTION.

Increasing the pre-jetting time decreases the production in the dry sand condition.

7 Evaluation

7.1 Jet flow rate

[redacted]

7.2 Jet pressure

[redacted]

7.3 Jet hydraulic power

[redacted]

7.4 Pre-jetting times

[redacted]

7.5 Sea inlet

[redacted]

7.6 Unloading flowrate

[redacted]

7.7 Initial conditions prior to fluidization.

[redacted]

7.8 Number of Nozzles

[redacted]

[redacted]

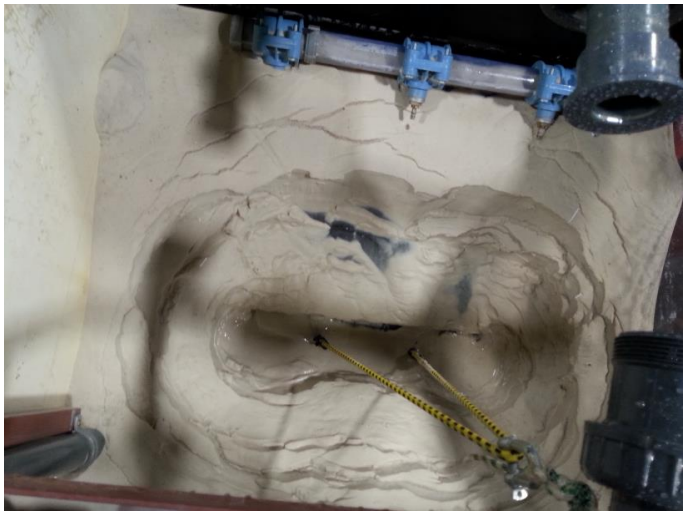

FIGURE 7.1 UNLOADING OF THE HOPPER VOLUME WITHOUT JETTING

[redacted]

7.9 Nozzle orientation

[redacted]

[redacted]

7.10 Nozzle positions

[redacted]

7.11 Jet diameter

[redacted]

7.12 Nozzle shape

[redacted]

7.13 Adapted nozzle configurations

[redacted]

7.14 Maximum Erosion/Trench depth

[redacted]

8 Conclusions and Recommendations

8.1 Conclusions

1. The flow rate is the most decisive parameter for influencing the fluidization and the unloading process. By increasing the jet flowrate per unit of time more water is inserted into the bed, delivering lower mixture densities, giving lower production rates and therefore increasing the unloading times.
2. High pre-jetting times insert more water in the bed and therefore decrease the mixture density, leading to lower unloading productions and higher unloading times.
3. Low flow rates and high pre-jetting times delivers approximate similar results as high flow rates and low pre-jetting times. Longer pre-jetting at lower flow rates delivers less residual load.
4. The pressure influences the fluidization velocity, higher pressures rates deliver faster fluidization over a certain volume.
5. The magnitude of hydraulic power is not the most decisive parameter for the unloading process, the combination of flow rate and pressure is decisive for the jet production, higher flowrates at constant power levels delivers higher jet production.
6. In scale 40seconds of pre-jetting time is to less for the existing jetting system. However, by using the existing jetting system and unloading with a constant water level condition and 40s of pre-jetting, delivers the most satisfying unloading time.

8.2 Recommendations

Based on the conclusions of the report the following is recommended:

[redacted]

- Position the nozzles as deep as possible in the hopper, preferably at the bottom of the hopper.
- Placing additional nozzle on the kippekooi the nozzle distance on the kippekooi is fine however, sand accumulates especially at the sidewalls of the kippekooi, therefore jets have to be positioned close to the walls at the top of the kippekooi.
- Use the constant water level condition for the unloading process. This unloading condition delivers the highest unloading productions, lowest residual load and the fastest unloading times.
- Minimize the opschoonslag, by strategically positioning the jets.
- Place the nozzles near the unloading channel and deep in the hopper; prevent water short cuts by taking a minimum distance of 2.5m of a perpendicular distance.

[redacted]

Testing method

IHC should build different hopper configurations (V, W), symmetrical and un-symmetrical unloading doors and test the influence and reach of the jets for these geometries and unloading configurations on the unloading process. This study showed that the best optimization is found by placing the jets on the right positions in the hopper, the jet parameters are more of secondary importance. To investigate the optimized jet positions. The approach and background of this report can be used to execute the tests for the other geometries. These simple tests deliver great insight in the influence of the jets on the unloading process. All the components in the scaled hopper can be designed adjustable and replaceable, which delivers simple and cheap experiments of the nozzles influencing the hopper unloading process.

Additional water canon on top of hopper.

In most experiments, a layer of sand was fixed between the walls of the hopper and the kippekooi, this part of the sand was not influenced by the jets and remained in the hopper for the complete unloading process. Therefore, it is recommended to install manually jet canons on the top of the hopper, intended for this kind of sanded parts and for the fluidization of the dead corners. This water canon reduces the amount of waterjets in the hopper, which mainly function to cover dead jet areas; the water canon delivers a more controllable unloading process.

References

Aberibigbe, O. and Rajaratnam, N. (1996). Erosion of loose beds by submerged circular impinging vertical turbulent jets. Journal of Hydraulic Research.

Albertson et al,(1950). Diffusion of submerged jets. Trans. ASECE,

Bindt, F. (1996). Constructieve uitwerking van een overvloeikoker als voorlosinrichting. Master's thesis, Delft University of Technology.

Breusers, H. N. C. (1977). "Hydraulic excavation of sand." Proc. Int. Course on Modern Dredging, Postgraduate Courses in Civil Engineering, The Hague.

Carman, P.C. (1937). Fluid flow through granular beds, Transactions, Institution of Chemical Engineers

De Groot et all (2009). Bresvloeing in zand, Geotechniek.

Ergun, S. (1952). Fluid flow through packed columns, Chemical Engineering Progresses, 48(2), pp. 89-110

Kobus, H., Leister, P., and B., W. (1979). Flow field and scouring effect of steady and pulsating jets impinging on a movable bed. Journal of Hydraulic Research, 175–192.

M.A.J. de Nijs (2014). On self-Emptying at discharge mixture densities, Van Oord Dredging and Marin Contractors bv.

Maas, F. (1992). Beunfluidisatie Geoptes 14. Master's thesis, Delft University of Technology.

Markvoort, J.W(2002). Horizontaal jetten in een zandpakket. Master's thesis, Delft University of Technology.

Matousek, V, (2004). Dredge Pumps and Slurry Transport, lecture notes OE4625, Faculty of Mechanical Maritime and Materials Engineering, TU-Delft.

Nasr El Din et all,(1986), A conductivity probe for measuring local concentration in a slurry system, University of Saskatchewan, Saskatoon,Canada

Nasr El Din et all,(1993), A conductivity probe for measuring local solids concentration in a slurry mixing tank, University of Alberta, Edmonton, Alberta, Canada

Nobel, A. (2013). On the excavation process of a moving vertical jet in cohesive soil. PhD thesis, Delft University of Technology.

Rajaratnam, N. (1976), Turbulent jets.

Rhee, C. van, G.L.M. van der Schrieck (2010). Physical scale modeling of dredging processes in sand and gravel, Proceedings of WODCON 19th, September 2010, Beijing, China.

Rhee, C. van,(2010). Sediment Entrainment at High Flow Velocity, Journal of Hydraulic Engineering.

Rhee, C. van,(2014). Slope failure by unstbale reaching, ice proceedings.

Rhee, C. van,(2016). Dredging processes, lecture notes OE4627, Faculty of Mechanical Maritime and Materials Engineering, TU-Delft.

Rhee,C. van, (1989). Bresprocessen tijdens het zuigen van zand. Bagt.434, Het zuigen en bressen van zand; Waterloopkundig Laboratorium,

Richardson, J., & Zaki, W. (1954). The Sedimentation of a suspension of uniform spheres under conditions of viscous flow.

Van Wijk, J.M.; Blok, B.W.G (2015), The influence of grain size on the performance of conductivity concentration meters,

Weisman,R.N., A.G.. Collins and J.M. Parks, 'Stabilization of tidal inlet channels by fluidization'. Proceedings of WODCON IX. Vancouver, British Columbia, Cenede/ October 29-31, 1980, pp.573-586.

Weisman,R.N., G.P. Lennon and E.W. Roberts, 'Experiment on Fluidization in Unbounded Domains'. Journalof Hydraulic Engineering. Volume 114, No. 5, May, 1988, pp.502-515.

Weisman,R.N., G.P. Lennon and E.W. Roberts, 'Experiment on Fluidization in Unbounded Domains'. Journalof Hydraulic Engineering. Volume 114, No. 5, May, 1988, pp.502-515.

I. Appendix: Scaling the jetting process in SAND.

Introduction

The aim of scaling is achieving similarity in the physical processes between the model and prototype. Scaling effects occurs when the conditions between both scales are not similar. Unclear understanding of the scale effects leads to wrong predictions and interpretations, which means the model is becoming less representative for the prototype. The information in this chapter is based on the collaboration of the works of (van Rhee; van der Schrieck, 2010) (Huijsmans; Journée; Massie, 2015).

Dimensionless indicators

The scaling factor expresses the ratio between a quantity in the prototype and the same quantity in the model. Often the length is used as parameter for the determination of the scaling factor.

$$N_x = \frac{X_{prototype}}{X_{model}} \qquad \textbf{I.1}$$

Scaling Rules:

For correct scaling the following scaling rules has to be respected:

1. The scaling factor for constants (e.g. $\rho_w,\ g,\ \rho_s$) is equal to one.
2. The scale of the sum (or difference) of two parameters is correctly scaled if the sum (or difference) of the parameters are in the same scale.
3. The scale of the product (or quotient) of a physical parameter is equal to the product (or quotient) of the scales of the parameters.

Similarity

Geometric similarity

Geometric similarity refers to equal scaling of length, width, height and the corresponding angles of the model.

Dynamic similarity

Dynamic similarity refers to the similarity of the movements of objects. Dynamic similarity for the jet process means identical scaling for jet velocity and jet flowrate.

Kinematic similarity

Geometric and Dynamic similarity leads to kinematic similarity. Respecting the kinematic similarity for the model, leads to similar scaling of the flow fields, wave patterns, flow streamlines and therefore particle trajectories.

Scaling effects

It is often not possible to model the physical processes simultaneously in the same scale without deviations, these deviations are called the ''scaling effects''. Often a trade-off has to be made of which Processes are decisive for the study and which process are of second order importance. It is important to have an understanding of the scaling effects, this delivers better estimations and predictions for the prototype scale.

Scale Indicators and effects

Froude Indicator

The Froude number is a common used indicator for kinematic similarity. The Froude indicator defines the ratio between the inertia force and the gravity force.

$$Fr = \frac{Inertia\ forces\ (mass\ forces)}{Gravity\ forces} = \frac{\rho_w \frac{du}{dt} L^2}{\rho_w\ g\ L^3} = \frac{u^2}{g.L} = \frac{u}{\sqrt{g\ L}} \qquad \textbf{I.2}$$

Where:

Fr= Froude number	$[-]$
u= flow velocity	$\left[\frac{m}{s}\right]$
L= Length	$[m]$
g= gravitational acceleration	$\left[\frac{m}{s^2}\right]$

Kinematic similarity means the same Froude number for model and scale conditions. The Froude number gives correct scaling of the gravity forces. Important for the settling process and the breaching process.

Reynolds indicator

The Reynolds number is also an indicator for the kinematic similarity. The Reynolds number defines the ratio between the inertia- and the viscous forces.

$$Re = \frac{Inertia\ forces\ (mass\ forces)}{Viscous\ forces} =)\frac{\rho_w \frac{du}{dt} L^2}{\mu\ u\ L} = \frac{\rho\ u\ L}{\mu} = \frac{u\ L}{v} \qquad \textbf{I.3}$$

$Re =$ Reynolds number $[-]$
$\mu =$ Dynamic viscousity $[pa\ s]$
$v =$ Kinematic viscosity $\left[\frac{m^2}{s}\right]$

The Reynolds number indicates whether the flow is in the laminar regime (Re $\leq$ 2000), or in the turbulent (Re > 2000) regime. The kinematic velocity of water is approximate 10^{-6}, the jet velocity is approximate $30\ \frac{m}{s}$, and the jet diameter is approximate 40 mm. substituting these parameters in the Reynolds numbers, leads to the turbulent flow regime. Equal Reynolds number values in the prototype and model scale delivers correct scaling for the viscous forces. Important for the scaling of turbulence and erosion process of the sand.

Tradeoff between Reynolds and Froude indicator

It is possible to scale the model with the Froude indicator or with the Reynolds indicator, the Froude indicator scales the gravity forces correctly, but the fluid viscosity and the effect of turbulence will encounter scale effects.
The Reynolds indicator gives correct scaling for the viscous forces, but the gravity forces encounters scale effects. It is not possible to apply the Reynolds scaling and the Froude scaling in the same model.

Froude indicator:

$$Fr = \frac{u}{\sqrt{g\ L}} \qquad \text{Scaling} \qquad N_{Fr} = \frac{N_u}{\sqrt{(L)}} = 1 \qquad => N_u = \sqrt{N_L} \qquad \textbf{I.4}$$

Reynolds indicator:

$$Re = \frac{u\ L}{v} \qquad \text{Scaling} \qquad N_{Re} = \frac{N_u\ N_L}{N_v} \qquad => N_u = \frac{1}{N_L} \qquad \textbf{I.5}$$

The Froude indicator decreases the velocity in the model with the square root of the scaling factor. The Reynolds indicator increases the velocity in the model with the scaling factor N_L.

The flow velocity of the nozzle in the prototype is approximately $u_{nozzle} = 30\frac{m}{s}$. Using a scaling factor of $N_L = 10$, gives a model velocity:

$$N_u = \frac{u_{prototype}}{u_{model}} \qquad \textbf{I.6}$$

.

$$u_{model} = \frac{u_{prototype}}{N_u} = \frac{u_{prototype}}{\frac{1}{N_L}} = \frac{30}{\frac{1}{10}} = 300\frac{m}{s} \qquad \textbf{I.7}$$

The velocity of $300\frac{m}{s}$ and therefore the pressure $p = \frac{1}{2} * \rho_w * u^2 = 450\ bar$ in the Reynolds scale are unpractically high.

The Reynolds scaling leads to correct scaling of the viscous forces and the effect of turbulence, the side effect are the unpractical high velocities. For correct scaling of erosion, the sand particles in the model must be in the order of the scaling factor times the average sand diameter in the actual scale ($7 \cdot 0.4 = 2.8mm$ in diameter). This resembles the size of marbles. In this report, the Reynolds indicator is not treated further, due to the unpractical high pressures and velocities the physical parameters are scaled according to the Froude indicator.

Using a scaling factor of $N_L = 10$, according to Froude scaling the velocity in the model becomes:

$$N_u = \sqrt{N_L} \rightarrow u_{model} = \frac{u_{prototype}}{N_u} = \frac{u_{prototype}}{\sqrt{10}} = \frac{30}{\sqrt{10}} = 9.5\frac{m}{s}$$

This is a far more practical velocity for small scale experiments.

Scaling the physical parameters

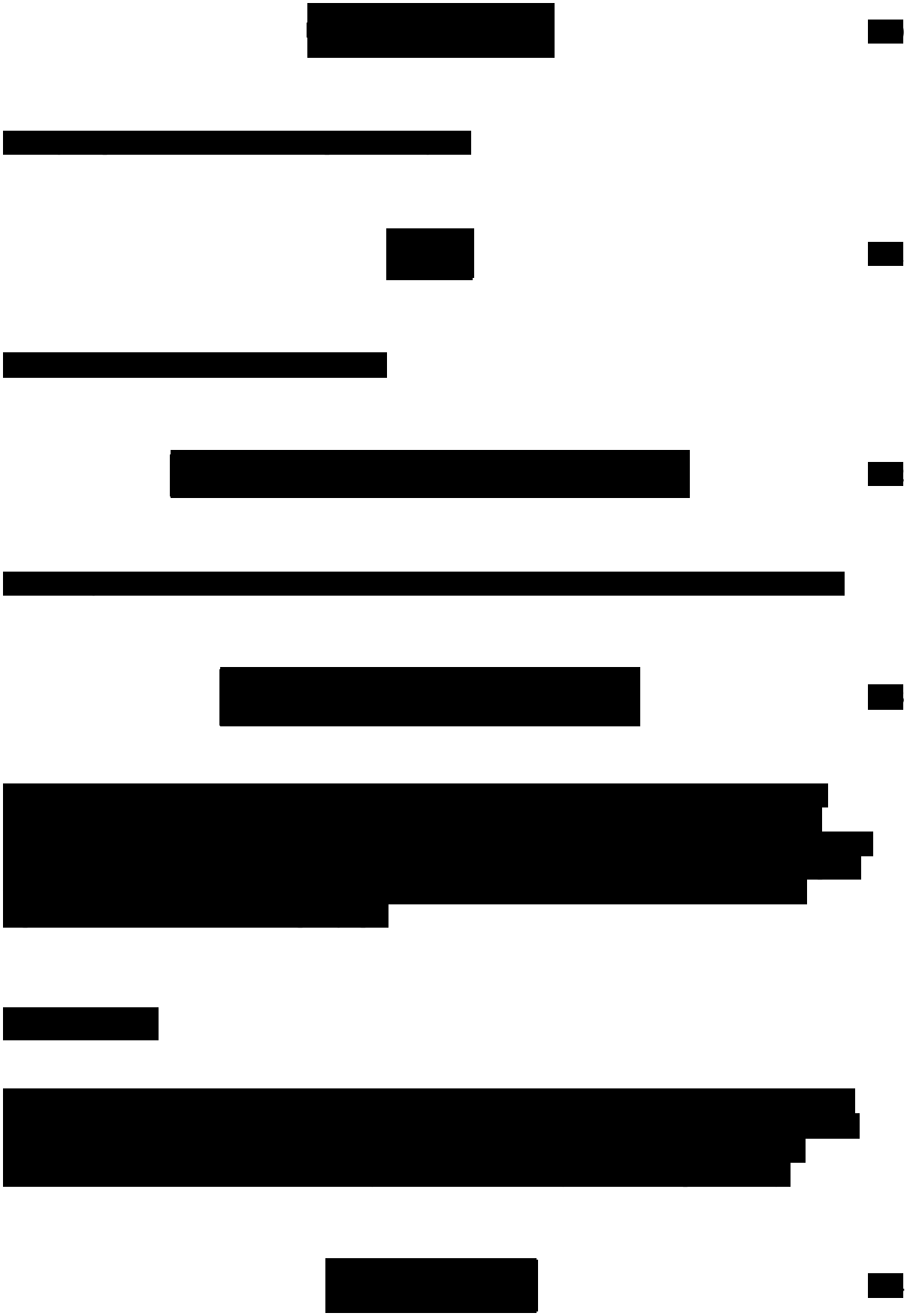

[redacted]

[redacted]

[redacted]

[redacted]

II. Appendix: Sand Mechanisms

Erosion

This chapter explains the erosion theory. The erosion of sand is explained by the traditional erosion functions.

Traditional Erosion equation

The definition of the erosion velocity is:

$$v_e = \frac{E - S}{\rho_s \, (1 - n_0 - c_b)} \qquad \textbf{II.1}$$

Where:

$v_e = erosion\ velocity\ \left[\frac{m}{s}\right]$
$E = pick - up\ flux\ \left[\frac{m}{s}\right]$
$S = settling\ flux\ \left[\frac{kg}{m^2\ s}\right]$
$n_0 = initial\ porosity\ of\ the\ bed\ [-]$
$c_b = near\ bed\ concentration\ [-]$

According to van Rhee (2010), the near bed concentration c_b for low concentrations can be neglected. For higher concentrations, c_b must be included in the denominator, otherwise incorrect results are calculated.

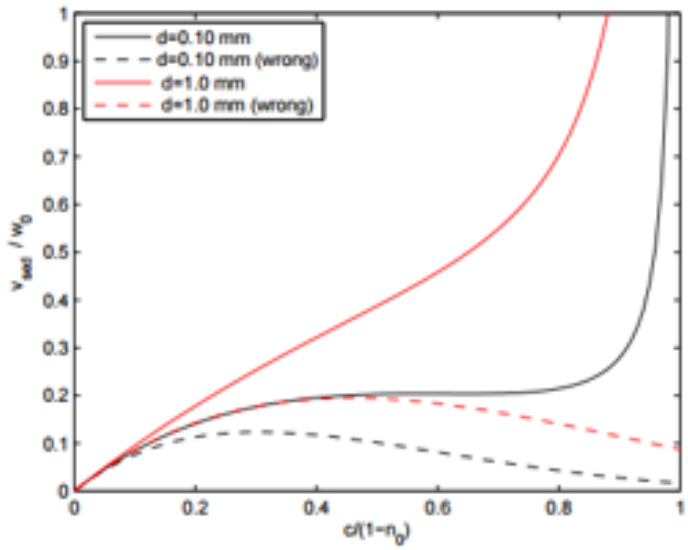

FIGURE II.1 SEDIMENTATION VELOCITY AS FUNCTION OF THE CONCENTRATION [VAN RHEE, 2016]
The dotted lines simulate the concentration development in case the bed concentration is omitted in the denominator; this is only allowed for low concentrations.

The Sedimentation flux S is:

$$S = \rho_s \, w_s \, c_b = \rho_s \, w_0 \, c \, (1 - c)^n \qquad \textbf{II.2}$$

Removing the pick-up flux from equation II.3gives the sedimentation velocity:

$$v_{sed} = \frac{S}{\rho_s \, (1 - n_0 - c)} = \frac{w_0 \, c \, (1 - c)^n}{(1 - n_0 - c)}$$

When the sedimentation flux is larger than the pick-up flux $S > E$, the equation for the erosion velocity then describes the sedimentation velocity.

Pick-up flux

Water flow close to the bed will initiate friction and therefore exert shear stress to the bed. The particle will start moving when the shear force exceeds the threshold value of the submerged weight of the particle and the resistance to motion excreted by the bed. The shear stress initiating the motion of the particle is widely known as the critical shear stress.

The bed shear stress reads:

$$\tau_b = \frac{f}{8}\,\rho_w\,u^2 \qquad \textbf{II.4}$$

.

Where:
f = frictional factor $[-]$
u = flow velocity $\left[\frac{m}{s}\right]$

The friction factor f is a function of the Reynolds number. The dimensionless Shield parameter describes the bed shear stress:

$$\theta = \frac{\tau}{(\rho_s - \rho_w)\,g\,D_{50}} = \frac{fu^2}{8\,\Delta\,g\,D_{50}} = \frac{u_*^2}{\Delta\,g\,D_{50}} \qquad \textbf{II.5}$$

With u_* the critical, shear velocity. The particles will move if the critical Shields value is larger than the actual shields value $\theta > \theta_{cr}$.

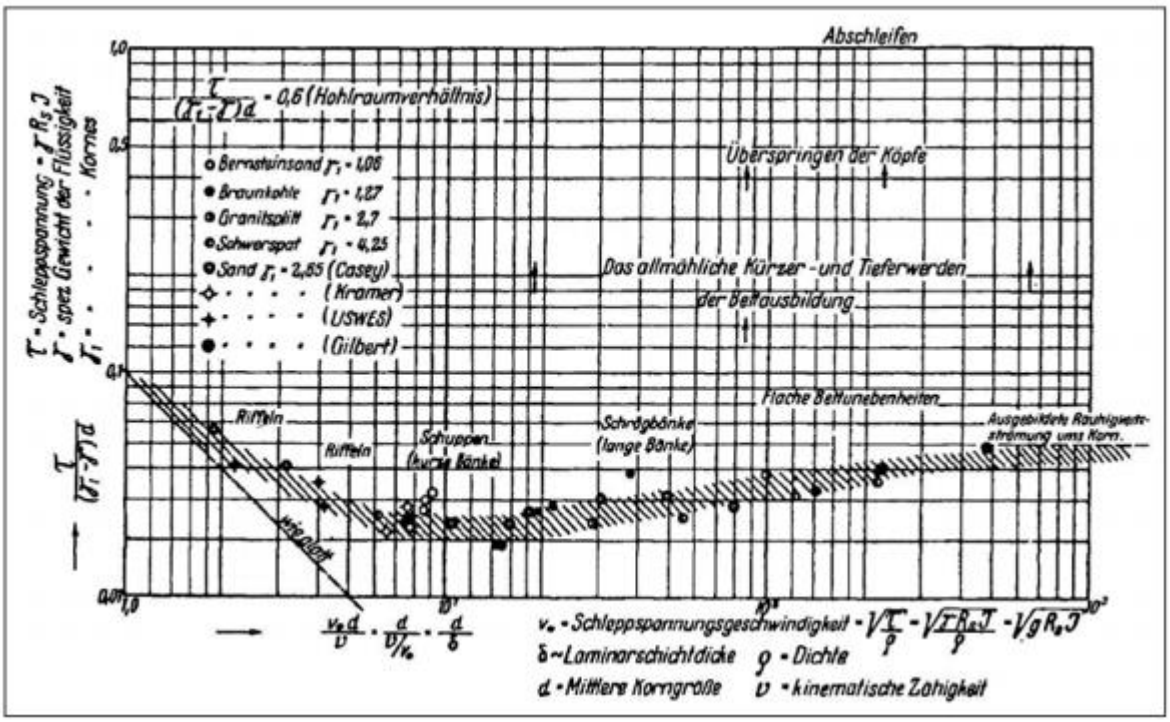

FIGURE II.2 ORIGINAL SHIELDS CURVE

Different authors (Brownlie, Van Rijn, Zanke, Miedema) developed approximation equations for the critical Shields parameter. Brownlie (1981) derived the expression:

$$\theta_{cr} = \frac{0.22}{Rp^{0.6}} + 0.06\exp\left(-17.77\ R_p^{-0.6}\right) \qquad \textbf{II.6}$$

Where

$$R_p = \frac{D_{50}\sqrt{\Delta\ g\ D_{50}}}{v} \qquad \textbf{II.7}$$

The expression for the pick-up flux is:

$$E = \ \Phi\ \rho_s\ \ \sqrt{\Delta\ g\ D_{50}} \qquad \textbf{II.8}$$

A well-known pick-up function Φ, is the van Rijn function (1984):

$$\Phi = 0.00033\ D_*^{0.3}\ \left(\frac{\theta - \theta_{cr}}{\theta_{cr}}\right)^{1.5} \qquad \textbf{II.9}$$

With the particle diameter defined as:

$$D_* = D_{50}\ \left(\frac{\Delta\ g}{v^2}\right)^{\frac{3}{2}} \qquad \textbf{II.10}$$

The pick-up function of van Rijn is valid for low flow velocities, in the order of $u < 1\frac{m}{s}$. For the jetting process in the hopper, the flow velocities are 20 to 30 times larger than the van Rijn approximation. This approximation is not credible for the jetting process.

Van Rhee modification

The processes for higher flow velocities is different for the erosion process, higher flow velocities erodes layers of particles, instead of particle-by-particle.

When a densely packed sand layer is sheared, the soil volume increases due to dilatancy. The pore volume increase gives a pore under pressure in the soil, water will flow towards the sheared zone in order to neutralize the under pressure. This water flow exerts an extra force on the sand, leading to less erosion of the sand than predicted by traditional erosion formula's (van Rhee, 2010). The modification of the traditional shields parameter by van Rhee (2010) includes the processes for high-speed erosion. The modification of van Rhee reads:

$$\theta_{cr}^{'} = \theta_{cr}\left(\frac{\sin(\varphi-\beta)}{\sin(\varphi)} + \frac{v_e}{k_l}\,\frac{n_l - n_0}{1-n_l}\,\frac{1}{\Delta\,(1-n_0)}\right) \qquad \textbf{II.11}$$

Where

$\theta_{cr}^{'}$ = modified Shields function
φ = angle of internal friction
β = slope angle
k_l = porosity of sheared layer
n_l = porosity

The first term of the modified shields function, is the influence of a sloping surface. The second term, describes the dilatancy phenomena. The third term, describes the effect of the seepage flow, due to the increase of the pore volume (van Rhee, 2010). For low slopping surfaces and low flow, velocities (or high permeability) transforms the modified function, back to the traditional shields function. For the high-speed erosion regime, the ratio between erosion velocity and permeability must exceed 3 (Van Rhee, 2016).

$$\frac{v_e}{k_l} > 3 \qquad \textbf{II.12}$$

The adapted erosion velocity becomes, van Rhee (2010):

$$v_e = \frac{1}{1-n_0-c_b}\,(\phi^1\sqrt{\Delta\, g\, d} - c_b\, w_s) \qquad \textbf{II.13}$$

With the adapted pick-up function:

$$\phi^1 = 0.00033 D_*^{0.3} \left(\frac{\theta - \theta_{cr}^1}{\theta_{cr}^1} \right) \qquad \textbf{II.14}$$

The adapted erosion function is also valid for low flow velocities.

Settling velocity of sediments

Force balance on settling particle.

The settling velocity of a single particle in a stagnant flow is a balance between the gravity force and the drag force working on the particle. The drag force of the fluid is a function of the dynamical viscosity and the density of the liquid. The drag is working in the upward direction of the particle. The force balance between on the particle gives:

$$F_{drag} = F_{gravity} - F_{bouyancy} \qquad \textbf{II.15}$$

With:

$F_{drag} = \frac{1}{2} \rho_w A_{particle} v_{ts}^2 C_D$

$F_{gravity} = \rho_s g V_s \xi$

$F_{bouyancy} = \rho_w g V_s \xi$

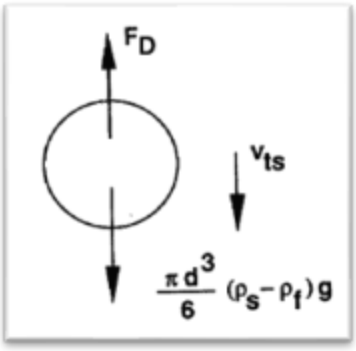

FIGURE II.3 FORCE BALANCE ON SETILIGN PARTICLE [MATOUSEK]

$A_{particle}$ is the particle surface facing the upward liquid flow, v_{ts} is the vertical settling velocity, C_D is the drag coefficient. The particle volume $V_s = \frac{\pi}{6} d^3 g$, the particle shape factor φ is the correction factor for non-spherical particles $\varphi = \frac{v_t}{v_{ts}} = 0.7$ for sand. Where v_t is the settling velocity for a

non-spherical particle and v_{ts} is the settling velocity for a spherical particle. Rewriting the equations of the force balance for v_{ts} gives the expression:

$$v_{ts} = \sqrt{\frac{2g\left(\rho_s - \rho_w\right) V_s}{\rho_w C_d A_{particle}}} \qquad \textbf{II.16}$$

The specific density Δ is:

$$\Delta = \frac{(\rho_s - \rho_w)}{\rho_w}$$

Substitution of the variables gives the well-known general expression for the settling velocity of a single particle:

$$w_0 = \sqrt{\frac{4g\Delta\, d\, \varphi}{3\, C_d}} \qquad \textbf{II.17}$$

Drag coefficient and flow regimes.

The dimensionless drag coefficient C_D is a function of the particle Reynolds number. Various authors (see Brown and Lawler, 2003) derived sphere drag correlations, for example, Turton and Levenspiel (1986) defined the following empirical expression:

$$C_D = \frac{24}{Re_p}\left(1 + 0.173 Re_p^{0657}\right) + \frac{0.413}{16300 Re_p^{-1.09} + 1} \qquad \textbf{II.18}$$

The expression for the particle Reynolds umber is:

$$Re_p = \frac{w_0\, d}{v} \qquad \textbf{II.19}$$

The drag coefficient is dependent of the flow regime of the particle. This flow regime is either laminar, transition or turbulent flow regime. Each regime has a different relation.

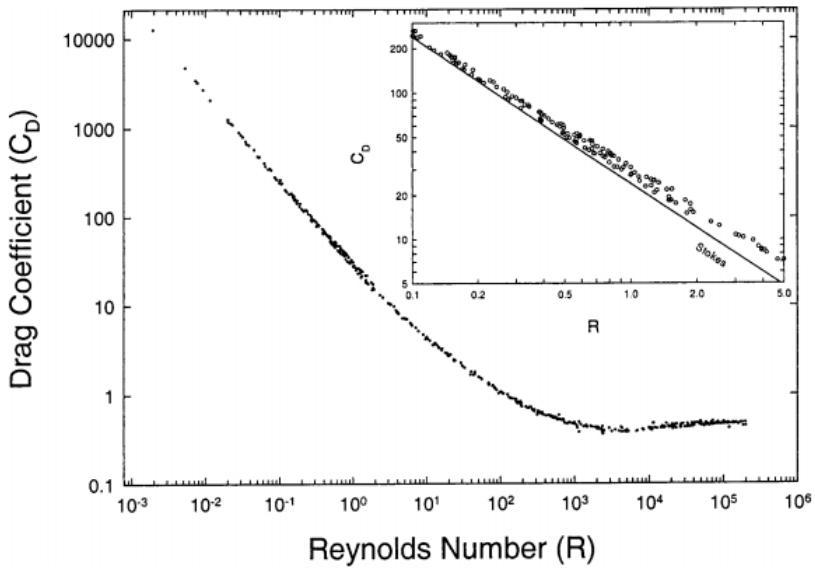

FIGURE II.4 DRAG COEFFICIENT AS FUNCTION OF THE REYNOLDS NUMBER, DELIVERING DIFFERENT FLOW REGIMES.

$$C_D = \frac{24}{Re_p} \qquad for\ Re_p \leq 1 \qquad \textbf{II.20}$$

$$C_D = \frac{24}{Re_p} + \frac{3}{\sqrt{Re_p}} + 0.34 \qquad for\ 1 < Re_p \leq 2000 \qquad \textbf{II.21}$$

$$C_D = 0.4 \qquad for\ Re_p > 2000 \qquad \textbf{II.22}$$

The flow pattern for the particle in the laminar regime is linear, this approximation is valid until $Re_p = 1$, see figure 4.4. This is the well-known Stokes equation for the settling velocity:

$$w_0 = \frac{\Delta g d^2}{18v} \qquad \textbf{II.23}$$

For the transitional regime, Budryck derived the following expression:

$$wo = \frac{8.925}{d} \sqrt{1 + 95\ (\rho_s - \rho_w) d^3)} - 1 \qquad \textbf{II.24}$$

The drag coefficient for the turbulent regime $Re_p > 2000$, as shown in figure II.4 is nearly constant. This results to the expression:

$$w_0 = 1.8\sqrt{\Delta g d} \qquad \textbf{II.25}$$

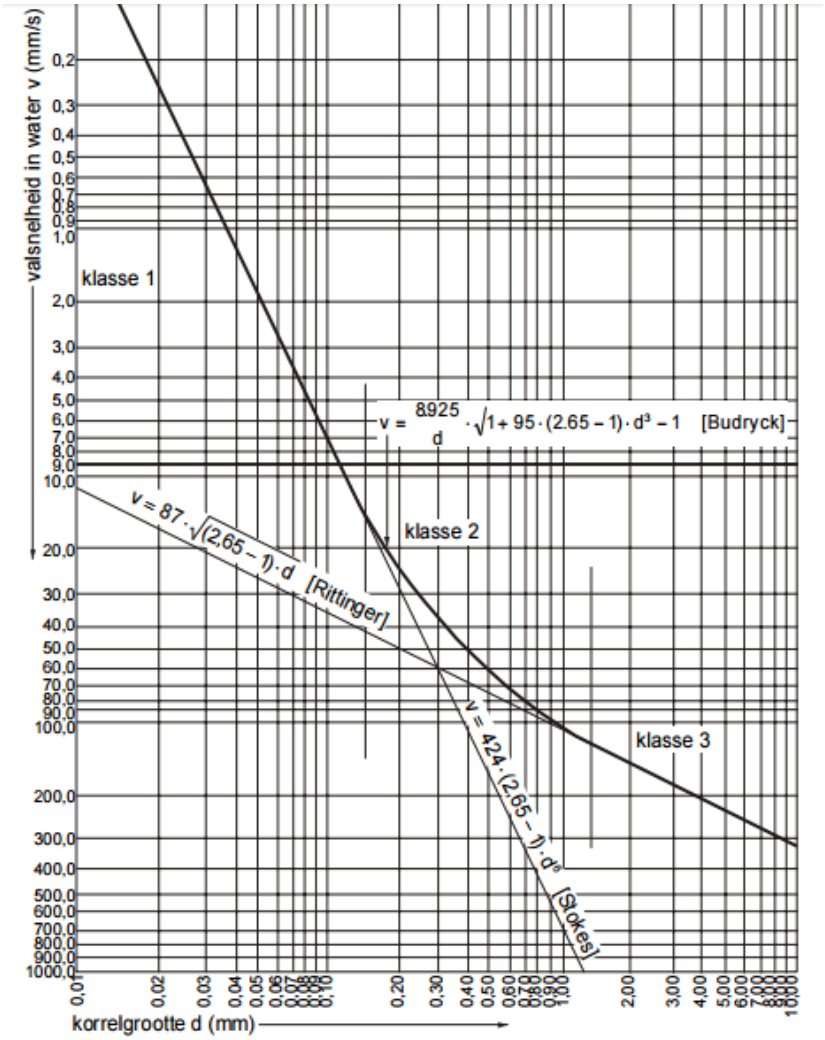

FIGURE II.4 SETILING VELOCITY FOR DIFFERENT FLOW REGIMES, USING STOKES, BUDRYCK AND RITTINGER EQUATIONS. [MATOUSEK 2004]

Ferguson and Church, 2004, came up with a new equation from which it is possible to estimate the settling velocity for a wide range of sediments:

$$w_0 = \frac{\Delta g d^2}{C_1 v + \sqrt{0.75 C_2 \Delta g d^3}} \qquad \textbf{II.26}$$

Where the constants $C_1 = 18$ and $C_2 = 0.4$ for spheres for and $C_2 = 1$ for sand.

Hindered Settling

The previous paragraph described the settling process for a single particle. A mixture, consists of more particles, these particles interfere with each other. The influence of the particles is based on the Van der Waals theory, the particles are attracting each other and therefore leading to a larger effective area for the drag forces. The larger area experiencing drag force results to more resistance to the downward velocity, the settling velocity decreases. Richardson and Zaki, 1954, estimated the hindered settling velocity for particles with the same particle size by:

$$w_s = w_0 \, (1 - c)^n \qquad \textbf{II.27}$$

Where w_s is the hindered settling velocity, w_0 is the settling velocity for a single particle, c is the volumetric concentration. Richardson and Zaki introduced the exponent n as a function of the particle Reynolds number and the diameter ratio of the particle diameter and the pipe diameter. Experiments ranging from very low concentration in the order of $c = 0.05$ up to the theoretical maximum concentration of $c = 0.65$ where executed for different particle Reynolds number in the range of $0.0000185 < Re_p < 7150$. Garside and Al-Dibouni (1977) gives a summarized relation for $0.04 < c < 0.55$ and flow regimes $0.001 < Re_p < 3.10^4$ of the original relation for the Richardson and Zaki expression. This expression is defines as:

$$n = \frac{5.1 + 0.27 \, Re_p^{0.9}}{1 + 0.1 Re_p^{0.9}} \qquad \textbf{II.28}$$

Breaching

Introduction

A well-known failure mechanism in the dredging industry is the breaching process. When a stationary suction dredger lowers the suction mouth in sand and the suction of sand starts, a suction pit will form in the sand. The suction pit triggers the breaching process. The disturbance of the slope and continuously removing sand prevents the sand to come into its natural equilibrium (the angle of repose). When the suction of the sand stops, the sand will come into its equilibrium angle over a certain period.

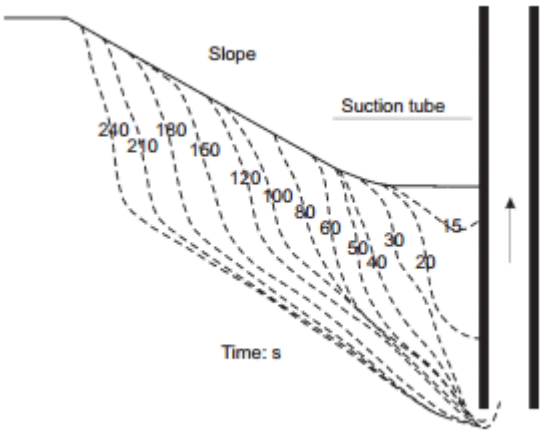

FIGURE II.5 BREACHING PROCESS IN A LABORATORY SCALE [BREUSERS 1974]

Active wall velocity

The active wall velocity is the retraining velocity of the upper surface of san bed, described as (van Rhee, 2010), (van Rhee, 2015):

$$v_w = (1-\varepsilon)\,\frac{\rho_s - \rho_w}{\rho_w}\,\frac{k_1}{\Delta\varepsilon}\cot\phi \qquad \textbf{II.29}$$

Where

v_w = active wall velocity $\left[\frac{\mathrm{m}}{\mathrm{s}}\right]$
$k_1 = loose\ state\ permeability\ [\mathrm{m}^2]$
$\phi = angle\ of\ internal\ friction\ [^\circ]$
$\Delta\varepsilon = relative\ porosity\ change = \frac{\varepsilon_1 - \varepsilon_0}{1-\varepsilon_1}$
$\varepsilon_1 = porosity\ at\ loose\ state\ [-]$

III. Appendix: Jet contraction- and dissipation

(Lecture notes van Rhee (2016); White M, Fluid Mechanics)

Assuming three flow regions: the flow before the nozzle opening (region 1), the flow at the contraction point (region 2) and flow at the discharge point (region 3). The Bernoulli equation for the flow region one and two gives:

$$p_1 + \frac{1}{2}\,\rho_w\,u_1^2 = p_2 + \frac{1}{2}\,\rho_w\,u_2^2$$

The equation for the flow region two and three becomes:

$$p_2 + \frac{1}{2}\,\rho_w\,u_2^2 = p_3 + \frac{1}{2}\,\rho_w\,u_3^2 + p2 + \frac{1}{2}\,\rho_w\,(u_2 - u_1)^2$$

The velocity drop between region 2 and 3 expressed as:

$$\mu = \frac{u_3}{u_2}$$

Combining and rewriting the equations gives:

$$p_1 + \frac{1}{2}\,\rho_w\,u_1^2 = p_3 + \frac{1}{2}\,\rho_w\left(u_3^2 + \left(\frac{u_3}{\mu} - u_3\right)^2\right)$$

The energy dissipation due to the contraction in-between region 1 and 3 reads

$$(p_1 - p_3)\,(1 - \zeta) = \frac{1}{2}\,\rho_w\,u_3^2$$

The energy dissipation in the nozzle due to contraction reads:

$$\zeta = \frac{\left(\frac{1}{\mu} - 1\right)^2}{1 + \left(\frac{1}{\mu} - 1\right)^2}$$

The nozzle discharge coefficient is a product of the contraction coefficient $c_c = \mu$ and the energy dissipation coefficient $c_v = \sqrt{1 - \zeta)}$:

$$c_d = c_c \, c_v$$

In order to minimize the nozzle energy dissipation, the energy dissipation coefficient c_v and the contraction coefficient c_c should be as small as possible

Including the discharge coefficient, the jet flow rate becomes:

$$Q_0 = c_d \, \frac{\pi \, D_0^2}{4} \, \sqrt{\frac{\left(2 \left(p_1 - p_3\right)\right)}{\rho_w}}$$

IV. Appendix: Ergun and Orning Formula

Ergun (1952) and Ergun and Orning (1949) has used small pipes for the modeling of the pore spaces in a bed. The pipe diameters where constant, with paralleled distance between the pipes. The volume of the pipes approximated the pore volume of the packed sand bed.

Ergun and Orning used for their model the general expression:

$$\frac{dp}{dx} = \alpha\, a\, v + \beta\, b\, v^2\, \rho_w$$

The pressure drop consists out of a viscosity parameter and a kinetic energy parameter.

v = Hydraulic velocity in the pipes $\left[\frac{m}{s}\right]$.
a, b =Coefficients
α, β =experimentally determined correlation coefficients

Coefficient a, is determined by the Poiseuille equation. This equation determines the pressure drop Δp for a cylindrical tube with diameter d and length L.

$$\frac{\Delta P}{L} = 32\, \mu_w\, \frac{v}{D^2}$$

Where:
v = Hydraulic velocity in the cylinder

The pressure drop for to the kinetic energy dissipation in turbulence describes:

$$\frac{\Delta P}{L} = \frac{1}{2}\, \rho_w\, v^2\, \frac{f}{L}$$

Where
f = frictional factor

Combining the dissipation of kinetic energy and dynamical shear stress gives the equation:

$$\frac{\Delta P}{L} = 32\, \mu_w\, \frac{v}{D^2} + \frac{1}{2}\, \rho_w\, v^2\, \frac{f}{L}$$

The total surface area of the tubes are:

$$A_w = \pi\, D\, L\, N$$

The total volume of the liquid in the tubes is:

$$V = \pi \frac{D^2}{4}\, L\, N$$

Ratio of total surface area divided by the Volume gives:

$$\frac{A_w}{V_w} = \frac{\pi\, d\, L\, N}{\pi \frac{d^2}{4} L\, N} = \frac{4}{D}$$

The total volume of the particles is determined by:

$$\sum (n_k\, v_k) = (1 - \varepsilon)\, A\, L$$

Where
n_k= number of particles
v_k= volume of a particle
A= the surface of the bed
L= height of the bed
ε = porosity of the bed

The ratio for the porosity area and the volume of the bed equal to the summation of the tubes gives after substitution the expression for the particle diameter d:

$$d = \frac{3\,(1 - \varepsilon)}{2\,\varepsilon}\, D$$

Rewriting gives the diameter of the tube:

$$D = \frac{2}{3} \frac{\varepsilon}{(1 - \varepsilon)}\, d$$

Substitution of the above equation and the equation for the superficial velocity $U = v\,\varepsilon$ in the expression for the pressure drop delivers:

$$\frac{dp}{dL} = \frac{72\,\alpha\,(1-\varepsilon)^2\,\mu_w\,U}{\varepsilon^3\,d^2} + \frac{3\beta\,(1-\varepsilon)\rho_w\,U^2}{4\,\varepsilon^3\,d}$$

Ergun experimentally determined the coefficients $\alpha\ and\ \beta$ for different particle size and different liquids. Ergun delivered the coefficients:

$$72\,\alpha = 150 \quad and \quad \frac{3}{4}\,\beta = 1.75$$

Adding the shape factor φ of non-spherical particles delivers the Ergun equation gives:

$$\frac{dp}{dL} = \frac{72\,\alpha\,(1-\varepsilon)^2\,\mu_w\,U}{\varepsilon^3\,(\varphi\,d)^2} + \frac{3\beta\,(1-\varepsilon)\rho_w\,U^2}{4\,\varepsilon^3\,\varphi\,d}$$

The shape factor φ is included for irregular shapes, $\varphi = \frac{(6/d_{particle})}{Area_{particle}/Volume_{particle}}$. According to J. H. Perry (1984) $\varphi = 0.83$ for rounded sand. When and Yu found for many systems $\varphi\,\varepsilon^3 \cong \frac{1}{14}$.

The Ergun equation has the following restrictions:

- In reality the pores are not small tubes with a constant diameter, the pores are constantly changing in size and structure.
- Static pressure is not taken into consideration
- The equation is a summation of a laminar term and a turbulent term, in reality one term at a time is decisive. In a laminar flow, the turbulent term is negligible and vice versa.

In order to acquire better estimations Oliemans (1997) approached the Ergun equation as follows:

The particle Reynolds number defined:

$$Re' = U\frac{d}{(1-\varepsilon)v}$$

The Ergun equation as function of the Reynolds number know defined as:

$Re' < 1.2$ $\quad \frac{dp}{dL} = 180\frac{(1-\varepsilon)^2\,\mu_w\,U}{\varepsilon^3\,(\varphi\,d)^2}$

$Re' > 1.2$ $\quad \frac{dp}{dL} = 150\frac{(1-\varepsilon)^2\,\mu_w\,U}{\varepsilon^3\,(\varphi\,d)^2} + 1.75\frac{(1-\varepsilon)\rho_w\,U^2}{\varepsilon^3\,\varphi\,d}$

V. Appendix: Af-100 Sand

KWARTSZAND VAN METTET AF100

Technical Data

Kwartszand van Mettet wordt na ontginning industrieel gewassen. **AF100** is beschikbaar zowel groevevochtig als gedroogd.
AF100 wordt los geleverd of verpakt in zakken of big bags (droog).
Dankzij de zeer fijne korrelgrootte, biedt **AF100** uitzonderlijke mogelijkheden, zowel in de keramische nijverheid als in gieterij- en vulstoftoepassingen.

KORRELVERDELING EN FYSISCHE EIGENSCHAPPEN
Methode: ISO-zeving

D50	130	µm
> 250 µm	1	%
> 180 µm	3	%
> 125 µm	50	%
> 90 µm	93	%
> 63 µm	99	%
< 63 µm	1	%
soortelijk gewicht	2,65	kg/dm^3
stortgewicht	1,3	kg/dm^3
hardheid	7	Mohs
pH	8	
gloeiverlies	0,20	%

TDS.03.05.82 2009-05-25 1/2

KWARTSZAND VAN METTET AF100

Technical Data

CHEMISCHE SAMENSTELLING (XRF) %

SiO_2	99,00
Fe_2O_3	0,050
Al_2O_3	0,50
TiO_2	0,10
K_2O	0,02
CaO	0,03

SIBELCO BENELUX

Bovenvermelde informatie is gebaseerd op gemiddelde waarden. De typische eigenschappen en chemische analyses zijn bedoeld als voorbeelden en kunnen niet beschouwd worden als vervanging voor eigen testen en onderzoek in alle omstandigheden waarbij eigenschappen en chemische samenstellingen kritische factoren zijn.
Verkoop en levering geschieden steeds volgens onze algemene verkoopsvoorwaarden.

CAS-Nr.: 14808-60-7 EINECS-Nr.: 238-878-4 Veiligheidskaart op verzoek

VI. Appendix: PSD-AF100 sand

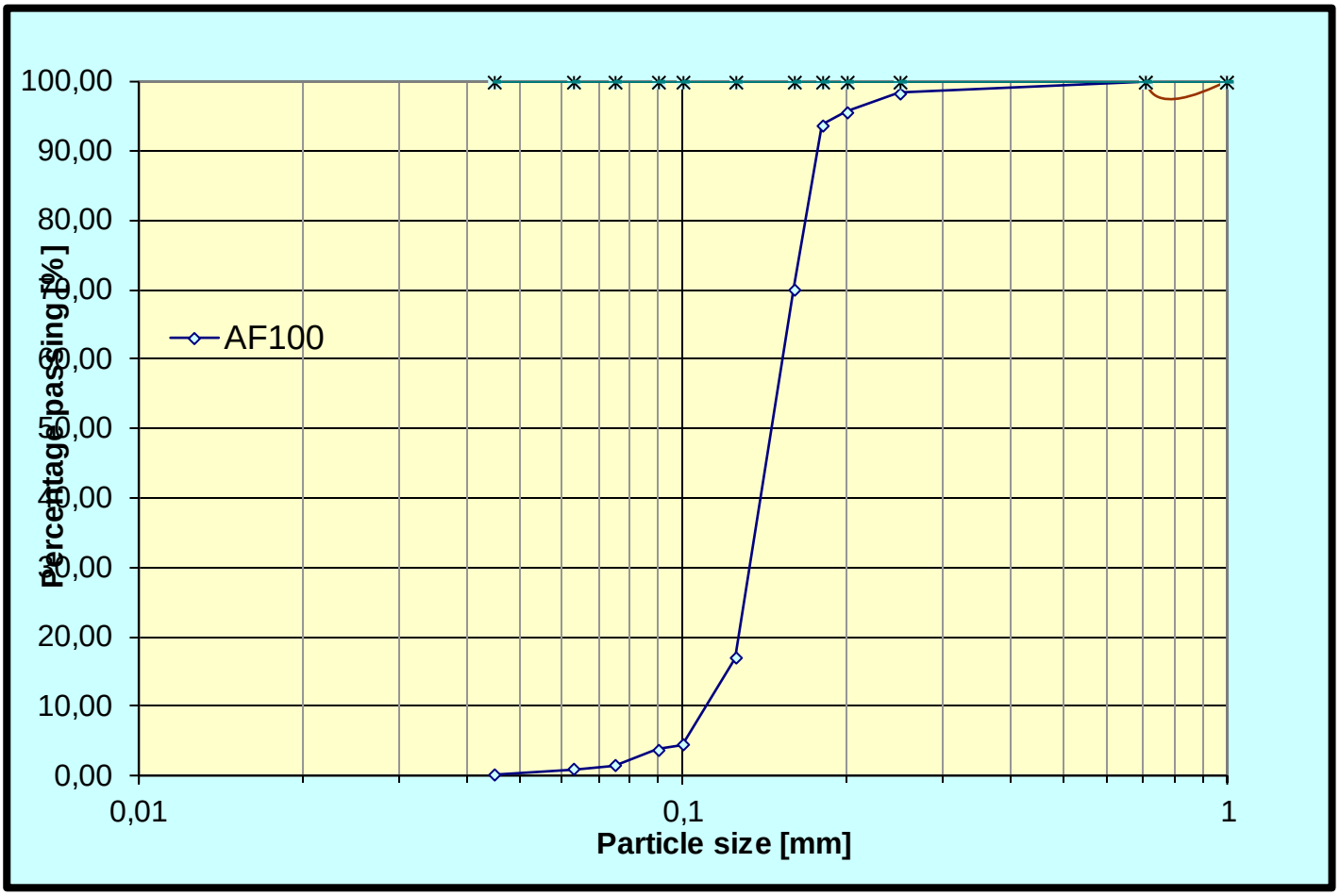

VII. Probe measuring locations